THE UNIVERSITY OF
WARWICK

AUTHOR: **Matthew George Brown** DEGREE: **Ph.D.**

TITLE: **Ion Scattering Studies of Metallic and Complex Bi-Metallic Systems**

DATE OF DEPOSIT: . . . . . .

I agree that this thesis shall be available in accordance with the regulations governing the University of Warwick theses.
I agree that the summary of this thesis may be submitted for publication.
I **agree** that the thesis may be photocopied (single copies for study purposes only).

Theses with no restriction on photocopying will also be made available to the British Library for microflming. The British Library may supply copies to individuals or libraries. subject to a statement from them that the copy is supplied for non-publishing purposes. All copies supplied by the British Library will carry the following statement:

> "Attention is drawn to the fact that the copyright of this thesis rests with its author. This copy of the thesis has been supplied on the condition that anyone who consults it is understood to recognise that its copyright rests with its author and that no quotation from the thesis and no information derived from it may be published without the author's written consent."

AUTHOR'S SIGNATURE: . . . . . .

USER'S DECLARATION

1. I undertake not to quote or make use of any information from this thesis without making acknowledgement to the author.
2. I further undertake to allow no-one else to use this thesis while it is in my care.

DATE SIGNATURE ADDRESS

. . . . . .

. . . . . .

. . . . . .

. . . . . .

. . . . . .

. . . . . .

. . . . . .

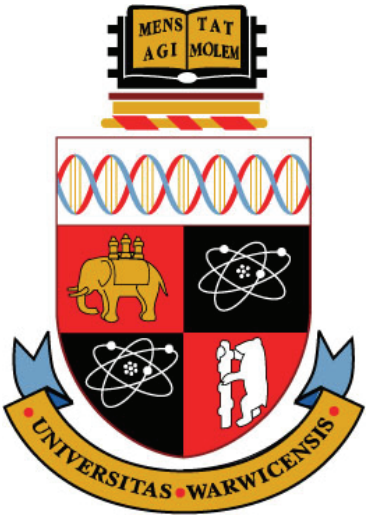

Ion Scattering Studies of Metallic and Complex Bi-Metallic Systems

Matthew George Brown M.Phys.

A thesis submitted in partial fulfilment of the requirements for the degree of Doctor of Philosophy

Department of Physics
University of Warwick

February 2010

THE UNIVERSITY OF WARWICK

Contents

Acknowledgments

Many people have contributed to supporting me in producing this thesis. I cannot possibly thank enough all the friends and family who have each helped in their own way; I am forever grateful to you all. Many thanks must go to my supervisor — and **still** busiest man in the Department of Physics — Prof. Chris McConville, for the opportunity given to me to work in such a fast-emerging field of physics, and for his patience throughout hard times.

To Dr. Marc Walker, for being all-round amazing. Firstly, in showing me the ropes, and teaching me how to 'inject vacuum'. Secondly, for continuing to provide much needed support and advice even during a period away from the department. And thirdly, for reading a number of these chapters for me... if there are any spelling mistakes, it's clearly your fautl Marc! (Yes, that was deliberate.)
And to Dr. Markus Draxler, for his assistance with repairs to the CAICISS apparatus and with MEIS data collection.

To Rob Johnston... what can i say; not only does this man provide enough sarcasm to run a [not-so] small country, but he single handedly provides ... ~~tea and coffee~~ ... support for all equipment in the group. If there's something mechanical he can't fix, then I'm yet to find it. Without the expertise of our technician, I doubt that any PhD in the group would be possible. And to Adrian Lovejoy... the electronics genius, and the rest of the guys in the Electronics Workshop, who constructed all the new gadgets and gizmos required to breathe new life into the ailing apparatus, despite being the second-busiest man in the department.

And where would I be without the banter, and endless ridicule received from the many members of the Surface, Interface & Thin Film Group. Your jokes and company during many long weeks at the UK MEIS Facility have kept me sane (barely), as well as your teaching me many important things. Who ever knew that *alabandical* and *obstrigillate* were real words; go figure.

Declarations

This thesis contains an account of my research, undertaken at the Department of Physics of the University of Warwick, between October 2005 and January 2010, under the supervision of Prof. C. F. McConville. The research reported here has not been submitted, either wholly or in part, at this or any other academic institution for admission to a higher degree.

The MEIS data reported in Part II were obtained by the author with the aid of Dr. Marc Walker and Dr. Markus Draxler. All of the analysis and interpretation presented pertaining to these data was performed by the author. All other data was obtained, analysed and interpreted solely by the author.

. . . . . .

M G Brown

January 2010

Parts of this work have been published or are in preparation:

M.G. Brown, M. Walker, L. Fishwick and C.F. McConville,
"Evaluation of the ion-atom interaction potential for He^+ ions scattered from a clean Pt(111) surface",
Submitted for publication to Surface Science

M. Walker, M.G. Brown, M. Draxler, L. Fishwick and C.F. McConville,
"Analysis of the interactions between He^+ ions and transition metal surfaces using CAICISS",
Submitted for publication to the Journal of Applied Physics

M.G.Brown, M. Walker, M. Draxler, L. Fishwick, T.C.Q. Noakes, P. Bailey and C.F. McConville,
"Evaluation of the submonolayer reconstructions of the Cu(100)/Sn system by ISS",
In preparation

Much of this work has also been presented at major international conferences (presenting author in bold):

M. Walker, **M.G. Brown**, M. Draxler and C.F. McConville,
"Re-evaluating the ion-atom interaction potential in LEIS",
The 16th Interdisciplinary Surface Science Conference (ISSC-16),
St Andrews, Scotland — Poster presentation

M.G. Brown, M. Walker, T.C.Q. Noakes, P. Bailey, M. Draxler and C.F. McConville,
"Determination of the sub-monolayer reconstructions of Cu(100)/Sn using MEIS",
The 16th Interdisciplinary Surface Science Conference (ISSC-16),
St Andrews, Scotland — Poster presentation.

M. Draxler, M. Walker, M.G. Brown and C.F. McConville,
"How accurately are the interaction potentials known in ion scattering spectroscopy",
The 24th European Conference on Surface Science (ECOSS-24),
Paris, France — Poster presentation.

M.G. Brown, M. Walker, C.F. McConville, T.C.Q. Noakes, P. Bailey and **M. Draxler**,
"Determination of the Cu(100)-$p(3\sqrt{2}\times\sqrt{2})$R45 °-Sn structure using MEIS",
The 24th European Conference on Surface Science (ECOSS-24),
Paris, France — Poster presentation.

Additionally, the author has contributed to the following publications during his PhD studies:

M. Walker, C.R. Parkinson, M. Draxler, M.G. Brown and C.F. McConville,
"Initial Growth of Platinum on Oxygen-Covered Ni(110) Surfaces",
Surf. Sci. **600** (2006) 3327

M. Walker, T.D. Veal, P.D.C. King, P.H. Jefferson, M.G. Brown, L.F.J. Piper, M. Draxler and C.F. McConville,
"Investigation of the structure of InN(0001) surfaces following AHC",
The 16th Interdisciplinary Surface Science Conference (ISSC-16),
St Andrews, Scotland — Poster presentation.

T.C.Q. Noakes, P. Bailey, C.F. McConville, M. Draxler, M. Walker, M.G. Brown, R. McGrath, J. Ledieu, J.A. Smerdon, L. Leung, T.A. Lograsso and A.R. Ross,
"Metal film epitaxy on quasicrystalline substrates studied using MEIS",
17th Interdisciplinary Surface Science Conference (ISSC-17),
University of Reading, United Kingdom — Poster presentation.

Abstract

A combination of modern surface science techniques has been used to investigate a number of systems, including the complex bi-metallic Cu(100)/Sn system, and several clean metal systems: Cu(100), Ni(110), Pd(111), Pt(111), and Au(111).

Five sub-monolayer surface reconstructions of the Cu(100)/Sn system have been studied by ion scattering spectroscopy. Phase 1 (complex $p(2\times2)$-based reconstruction) is best described by an alloy model with anti-phase domain boundaries. Phase 2 ($p(2\times6)$-based reconstruction) by an alloy structure with stress relieved through the introduction of regular vacancies within the second layer. Phase 3 ($c(2\times2)$-based reconstruction) by an alloy structure with every third row of Cu atoms in the outermost layer removed. Phase 4 ($c(4\times4)$-based reconstruction) by one of two possible Sn overlayer models. And a fifth intermediate phase between Phase 2 and Phase 3 was unable to be accurately reproduced.

As a result of limitations identified, a number of improvements were made to the Warwick co-axial impact collision ion scattering spectroscopy (CAICISS) system. The net result of the improvements has been: increased ion beam intensity and energy range, reduced runtime (down from 3 hours to 1 hour), and lower main chamber base pressure (down from 8×10^{-10} mbar to 1×10^{-10} mbar). New analysis routines have been developed; a first attempt has been made to apply a reliability factor to CAICISS fits, and codes have been written to automate CAICISS structural optimisation. Existing codes for analysis of medium-energy ion scattering (MEIS) data have also been improved.

A series of five low-index clean transition metal surfaces, each with well-known surface relaxations, have been studied with CAICISS in order to investigate the mass and primary beam energy dependence on the screening length correction factor. The new automated optimisation codes were utilised to find optimum values of correction factor over a range of incident beam energies. Results showed consistently lower values than those generally applied in other low energy incident ion techniques — approximately 0.26 lower in all cases, with no dependence on incident energy. [Cu: 0.58, Ni: 0.57, Pt: 0.74, Au: 0.75, Pd: 0.71] compared to values from other authors of [Cu: 0.85, Ni: 0.84, Pt: 1.00, Au: 1.00, Pd: 0.91]. Knowledge of the screening length correction factor values applicable for CAICISS will improve the accuracy of all future studies using this technique.

List of Abbreviations

Abbrev.	Description	Definition
AES	Auger electron spectroscopy	page 14
CAICISS	Coaxial impact collision ion scattering spectroscopy	page 16
DFT	Density functional theory	page 90
fcc	Face-centred cubic	page 29
HAS	Helium atom scattering	page 81
IBA	Ion bombardment and annealing	page 7
IFFCO	Implicit filtering for constrained optimisation	page 22
IPA	Iso-propyl alcohol	page 94
ISS	Ion scattering spectroscopy	page 8
LEED	Low energy electron diffraction	page 17
LEED	Low energy electron diffraction	page 17
LEED I-V	LEED intensity versus voltage	page 27
LEIS	Low energy ion scattering	page 8
MEIS	Medium energy ion scattering	page 14
ML	Monolayer	page 7
NIXSW	Normal incidence x-ray standing wave	page 34
PEEK	Polyether ether ketone	page 100
RBS	Rutherford back-scattering	page 8
SOAR	Structural optimisation automation routine	page 23
SPALEED	Spot-profile analysis LEED	page 53
STM	Scanning tunnelling microscopy	page 34
ToF	Time-of-flight	page 16
TFM	Molière approx. to the Thomas-Fermi model	page 10
TLEED	Transmission LEED	page 72
TSP	Titanium sublimation pump	page 93
UHV	Ultra-high vacuum	page 7
ZBL	Ziegler-Biersack-Littmark	page 103

CHAPTER 1

Introduction

Motivation

As the typical dimensions of electronic devices are reduced, the properties and behaviour of the surface and near-surface regions becomes increasingly important. Modern surface science consists of a large number of techniques that can probe the chemical, electrical and structural properties of these interfaces with a high degree of surface specificity. The combination of this wide range of powerful techniques and the demand from industry to find new materials for device construction mean that surface science is positioned to become one of the most important fields in modern science.

Bi-metallic systems can display complex behaviours (different to those of bulk alloys) and a large range of surface structures, including thin film growth and surface alloys. There are many possibilities, all of which yield different chemical and structural properties and may have uses in many areas of industry. Crucial to being able to study these complex phenomena is to have a good knowledge of the underlying fundamental physics which governs the interactions of ion scattering techniques with crystal surfaces.

Accurate characterisation of surface properties requires that a chemically and structurally constant surface be maintained. The adsorption of atmospheric contaminants could lead to changes in surface properties during experimentation. Therefore, vacuum conditions are widely used in surface science experiments to allow access to pure and constant surfaces. However, it must also be noted that industrial applications very often require surfaces to operate in air. The presence of atmospheric contaminants can significantly change the atomic structure, chemical composition and electronic properties of the surface. Thus, in many cases surface science experiments are now carried out in air.

In this thesis, modern surface science techniques have been used to study a complex bi-metallic system and a number of clean metal surfaces. The Cu(100)/Sn system displays a number of different surface structures. Study of clean metal surfaces will lead to a better understanding of the fundamental physics of the ion-surface interaction.

Thesis Outline

The content of this thesis is divided into four parts. Part I discusses background theory, covering a wide range of topics. The concept of a single crystal is introduced, what is meant by its surface, and how surfaces are uniquely identified. Then the ion-surface interaction and basics of ion scattering techniques are covered. Finally, supplementary techniques are briefly discussed, and the methods of computer simulation and data analysis are outlined.

Part II focuses on ion scattering investigations of the Cu(100)/Sn system. Five surface reconstructions are characterised and structural solutions are identified. Part III begins by outlining a number of improvements made to the Warwick CAICISS system as a result of limitations identified during the previous investigation; then it continues with a study of five clean metal surfaces in order to investigate the specifics of the ion-surface interaction for low energy ion scattering. Finally, Part IV provides a brief summary of the key experimental results, and outlines a number of possible future studies and improvements.

Part I

Theory and Equipment

List of Chapters

CHAPTER 2

A Brief Introduction to Surface Science

The study of solid surfaces — known as surface science — has been a fast-expanding field since the early 1960s. The aim is to explore the structural, compositional and electronic properties of surfaces, in order to advance understanding of their behaviour and find new industrial and technological applications.

In this thesis, metal surfaces in particular are examined. The importance of metal surfaces is already well understood by modern industry; studies have produced wide-ranging applications, including heterogeneous catalysis [1] and magnetic recording [2]. This chapter presents a brief introduction to some of the key concepts and notations used in describing the nature of solid surfaces. The concepts introduced will be referred to throughout this thesis.

2.1 Crystalline structures and surfaces

All of the solids discussed in this thesis are single-crystal solids, consisting of atoms arranged in a continuous three-dimensional periodic lattice. For most single-crystal solids one can specify a *unit cell* from the periodicity of atoms within the lattice. The unit cell is the smallest volume that can define the positions of all atoms in the solid; the long-range order of the crystal is built up by repetition of the unit cell in each of the crystal axes.

The surface of a single-crystal solid need not run parallel to the face of the unit cell. Therefore, surfaces are defined by their orientation relative to the unit cell. A surface creates a plane through the unit cell, and the particular orientation of that plane gives the identity of the surface. It is usual to refer to the orientation of a plane by its *Miller indices*.

Miller indices arise by considering how the plane intersects the axes of the unit cell. A set of three numbers is assigned which quantify the intercepts and thus uniquely identify the plane/surface. The notation takes the form (hkl), where h, k and l are the reciprocal fractional intercepts of the unit cell. Figure 2.1 shows an illustration of several planes for a simple cubic unit cell. The metal surfaces investigated in this thesis are all low index surfaces (i.e. low Miller indices — (100), (110) or (111)). Note that, symmetrically equivalent indices are often used interchangeably (i.e. (100), (010) and (001) are all equivalent unless stated otherwise).

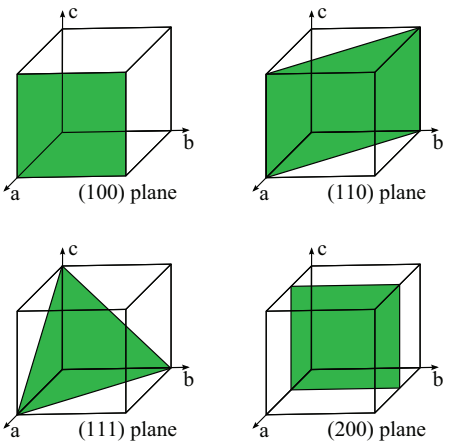

Figure 2.1 Illustration of the (100), (110), (111) and (200) crystal planes for a simple cubic lattice (adapted from Walker [3]).

2.1.1 Relaxation and reconstruction

A solid surface is a discontinuity in the three-dimensional periodicity of a crystal lattice. The local environment of a surface atom is very different from that of a bulk atom; surface atoms have fewer neighbouring atoms, and thus have more free energy because they are less constrained. To minimise the free energy of the surface, changes to the atomic structure can occur by relaxation or reconstruction of the atomic layers in the near-surface region.

If the changes in the structure leave the two-dimensional surface periodicity unchanged from that of the bulk, then the surface is said to be relaxed. In the majority of cases, the only change to the near-surface layers is a change in the inter-layer spacings. Most clean metallic surfaces show this *relaxation*. Typically, expansions or contractions in inter-layer spacings of a few % are observed [4].

Surface structural changes can also be in the form of a rearrangement of atoms in the surface plane — a *reconstruction*. Surface reconstructions increase the size of the surface unit cell. Simple reconstructions of clean surfaces often result from minimisation of dangling bonds (i.e. bonds are formed between adjacent atoms to reduce the number left free due to the surface lattice discontinuity). For example, the clean Si(001) surface forms a reconstruction consisting of symmetric dimers and a surface periodicity twice that of bulk Si [5].

Reconstruction can also result from the presence of adsorbates on the surface, and through differences in bond strength between the different elements of the adsorbate and underlying substrate. A number of factors can affect the reconstruction of a surface, including: the composition of the substrate and adsorbate, the coverage of the adsorbate, and the ambient conditions (i.e. temperature, gas pressure, etc.) [6].

2.1.2 Reconstruction notation

The change in surface layer structure due to a reconstruction can be specified by a matrix notation [6]. If a and b are the base vectors of the bulk lattice, and a_s and b_s are the base vectors of the reconstructed superlattice, then the relation between the two sets of vectors, are given by the matrix equation:

$$\begin{pmatrix} a_s \\ b_s \end{pmatrix} = \begin{pmatrix} M_{11} & M_{12} \\ M_{21} & M_{22} \end{pmatrix} \begin{pmatrix} a \\ b \end{pmatrix} \tag{2.1}$$

Matrix notation, whilst capable of describing the most complex of reconstructions, can be hard to visualise even for simple cases. A more convenient and compact notation was proposed by Wood [7] in 1964, and has become the preferred method of describing surface structures. The notation defines the ratio of the surface and substrate lattice periodicity and an angle through which the surface superlattice must be rotated in order to align the base vectors. This leads to a generic system of notation for surfaces of the form:

$$X\,\{hkl\}\,(m \times n)\,\mathrm{R}\phi^\circ - A \tag{2.2}$$

In this notation, the bulk substrate material is specified in place of X, and $\{hkl\}$ is the surface plane orientation. The rest of the terms describe the reconstruction; $\mathrm{R}\phi^\circ$ is the angle of the superlattice to the bulk lattice, and m and n are the ratios of the lattice periodicity in each base direction. If the reconstruction is brought about by adsorption of another species onto the surface, then it is specified in place of A. In many cases, Wood notation (and variations thereof) provides a more intuitive method of describing the nature of a surface. An extension to the notation allows it to describe non-primitive unit cells in a simpler way [6]:

$$\left(\sqrt{2} \times \sqrt{2}\right)\mathrm{R}45^\circ \quad \text{describes the same surface reconstruction as} \quad c\,(2 \times 2)$$

The reconstruction described by these expressions can be seen in Figure 2.2. The use of this centred unit cell extension to the Wood notation is usually coupled with the addition of a preceding 'p' to any reconstruction which is not centred, to denote it as primitive. This is mainly for clarity, and is omitted in some cases. Where no letter precedes the Wood notation, 'p' is implied.

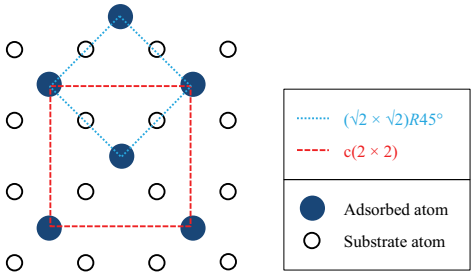

Figure 2.2 Example of the use of Wood notation for a simple cubic lattice (adapted from [3]). The two notations shown describe the same reconstruction, but using different base vectors.

2.1.3 Adsorbate coverages

Surface studies often involve deposition of an adsorbate, so it is helpful to define a measure of how much adsorbate is on a surface. This is usually referred to as a *coverage*, and is measured in *monolayers*. A monolayer (ML) is defined such that, one monolayer of adsorbate has the same number density of atoms as a single parallel layer of the substrate material. Take the simple example system shown in Figure 2.2; the adsorbate atoms in the $c(2\times2)$ reconstruction have a number density half that of the underlying substrate. This coverage is therefore 0.5 ML.

2.2 The need for vacuum conditions

The majority of surface studies are conducted either on 'clean' surfaces, or after deposition of some known amount of adsorbate onto a surface. If the properties of the surface are to be well-characterised, it is essential that surface composition is not modified throughout the investigation. Sub-monolayer quantities of contamination can lead to significant changes in surface electronic, chemical and structural properties.

In order to reduce the rate of arrival of contaminants surface science investigations are commonly conducted under vacuum. Consistent surfaces are often required to be maintained for several hours, which calls for a pressure in the low 10^{-10} mbar ultra-high-vacuum (UHV) regime [6]. Ion scattering experiments would not be possible without UHV conditions, due to the rate of contamination and inability to produce a suitable ion beam with which to probe the surface due to interactions with the surrounding gas.

2.3 Ion bombardment and annealing

Contaminants must be removed *in situ* before studies commence. Preparation of the surfaces studied in this thesis was performed using an ion bombardment and annealing (IBA) process. Ion bombardment is an effective and widely used technique, particularly for metal surfaces; many atomic layers can be stripped away quickly. Typically, Ar^+ ions with energies of between 0.5 keV and 5 keV are accelerated towards the surface. By sputtering at grazing incidence, the Ar^+ ions penetrate less deeply into the crystal, causing less surface damage [8]. Owing to the Ar sputtering damage, the surface must subsequently be annealed to restore order. Annealing involves heating the substrate to temperatures sufficiently high to induce reordering or recrystallisation within the sample, but without inducing melting. Annealing often has the added effect of leading to segregation of impurities to the surface. Therefore, it is frequently necessary to conduct several IBA cycles to obtain a clean, well-ordered surface.

CHAPTER 3

Experimental Techniques

This thesis uses ion scattering techniques, to investigate complex systems and draw conclusions about the nature of the surfaces examined. The data obtained from ion scattering studies gives information about both the composition and atomic structure of the target surface. Combined with some supplementary analytical techniques, ion scattering becomes a powerful tool in characterising solid surfaces and understanding their interaction with charged particles [9].

This chapter outlines the key principles of ion scattering, before moving onto discuss the specifics of different implementations. Supplementary techniques are introduced along with examples that put their usage in context.

3.1 Ion scattering spectroscopy

Ion scattering spectroscopy (ISS) has been used for many years. It was Rubin [10] who first demonstrated that it was possible to examine charged particles elastically scattered from a surface in order to identify the composition of the target material. Early experiments used high-energy ions to determine composition as a function of depth [11]; a technique now known as Rutherford back-scattering (RBS).

Interest was soon raised in using lower energy, higher mass ions [12,13]. At lower energies, the penetration depth of the incident ions and the mean-free-path for inelastic collisions are relatively small; neutralisation rates are also relatively high. This leads to high surface specificity, as fewer multiply-scattered ions are detected [14]. This technique is generally known as low-energy ion scattering (LEIS).

Scattered ions are detected, and their direction and kinetic energy measured. Kinetic energy gives information about the target composition, and compiling a spectrum of scattering intensity as a function of the scattering direction gives structural information about the target surface. The rest of this section is concerned with explaining the information contained in the properties of scattered ions.

One of the main strengths of ion scattering is that it can be modelled as a simple kinematic binary collision — an elastic collision involving two bodies, much like a billiard ball collision.

The incident ion energy and mass are known; data collection measures the scattering angle and energy. From this, it is possible to apply the laws of conservation of energy and momentum to calculate the mass of the surface target atom that was impacted. The resulting relation is known as the kinematic factor (Equation 3.1). It relates the ratio of energies (E_1/E_0), the scattering angle (θ), and the ratio of masses ($A = M_2/M_1$).

$$\frac{E_1}{E_0} = \left[\frac{\cos\theta \pm \sqrt{A^2 - \sin^2\theta}}{(1+A)}\right]^2 = k \tag{3.1}$$

Figure 3.1 shows an illustration of the binary collision process. An ion with mass (M_1) and kinetic energy (E_0) impacts a surface atom with mass (M_2). The ion is scattered through an angle (θ), transferring kinetic energy to the target atom during the collision. The scattered ion possess a kinetic energy (E_1), whilst the target atom recoils with a kinetic energy (E_2).

At each particular scattering angle, distinct peaks in kinetic energy are seen for each species of atom on the target surface. The ability of a technique to distinguish between target atoms of different masses is known as the *mass resolution*. An important consequence for ion scattering is that mass resolution can be improved by increasing the energy transfer to the target atoms.

This is accomplished by using heavier ions in the incident beam (i.e. better mass resolution is achieved with a smaller value of the ratio of masses, A). The complication associated with this is that using high energy and high mass incident beams in order to increase energy transfer (e.g. Ne^+ instead of He^+) can lead to more surface damage during data collection. The solution is a reduction in the beam energy to help mitigate the damaging effects of the ions, whilst still providing good mass separation. However, it is always advisable to use an ion beam of the lowest possible mass, to reduce surface damage. A large number of variants of ion scattering have arisen that utilise different incident ions and beam energies in order to obtain the best resolution data possible from various target surfaces [10–12, 15–19].

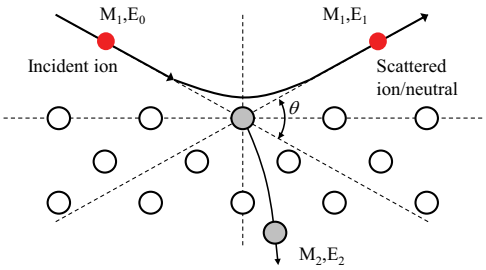

Figure 3.1 Schematic of the binary collision of an ion with a surface atom. The interaction is described in the text (adapted from van der Veen [15]).

3.1.1 Interaction potentials

The binary collision model is a good starting point to understand the data collected from ISS experiments, but Coulomb ion-surface interactions provide a more accurate description. This more thorough treatment of the collision is required in order to understand some of the additional processes taking place during low-energy scattering events.

Interaction potentials are based on the repulsion between an ion with nuclear charge $Z_1 e$ and target surface atom with charge $Z_2 e$. At high beam energies interaction time is short due to the fast-moving incident ions and the presence of electrons becomes negligible; this is the binary collision approximation. At low beam energies ions are moving more slowly so the interaction time is longer and it becomes necessary to take account of the electrons, which have a screening effect on the ion charge. Most common interaction potentials contain a Coulomb $(1/r)$ term, multiplied by a screening function, $\Phi(r/a)$, where r is the distance between atomic centres, and a is the screening length. For example:

$$V(r) = \frac{Z_1 Z_2 e^2}{r} \times \Phi(r/a) \tag{3.2}$$

3.1.2 Electron screening

Electron screening modifies the Coulombic repulsion by shielding the target atom from some of the charge of the ion (and *vice versa*). The *screening length* (a) is a value characteristic of the particular ion and target atom combination, and is usually calculated by one of two expressions (discussed below); it is most noticeable at low energies, where ion-surface interaction times are relatively long.

The most commonly used screening function for low and medium energy ion scattering techniques is the Molière approximation to the Thomas-Fermi model [20, 21] (TFM), which uses either the Firsov [22] or Lindhard [23] screening length expressions. Comparisons between different screening functions have been made previously [24], but are not discussed here; all studies in this thesis have made use of the TFM model exclusively — a restriction imposed by the simulation codes employed for data analysis. The TFM screening function is given by Equation 3.3, and screening length is calculated from Equation 3.4 or Equation 3.5.

$$\Phi(r/a) = 0.35y + 0.55y^4 + 0.10y^{20} \tag{3.3}$$

$$y = \exp\left(-0.3r/a\right)$$

$$a_{\text{Firsov}} = 0.4685\left[Z_1^{1/2} + Z_2^{1/2}\right]^{-2/3} \tag{3.4}$$

$$a_{\text{Lindhard}} = 0.4685\left[Z_1^{2/3} + Z_2^{2/3}\right]^{-1/2} \tag{3.5}$$

In the low energy regime, the characteristic screening length in the TFM approximation is often also reduced by an empirical factor, given by the expression [24]:

$$C_{\mathrm{f}} = 0.045\left[Z_1^{1/2} + Z_2^{1/2}\right] + 0.54 \tag{3.6}$$

The correction factor becomes extremely important when analysing low-energy ion scattering data. Once the interaction potential has been accurately modelled — by use of the TFM approximation coupled with a correction factor — it can be used to gain quantitative information about surface structural properties, through the evaluation of *shadow cones*.

3.1.3 Shadow cones

An important consequence of the repulsive nature of the ion-surface interaction is the production of a region behind the target atoms into which incident ions cannot penetrate — a shadow cone. Figure 3.2 illustrates how a shadow cone is produced. After many ion-surface interactions at a particular incident angle, the periodic nature of the surface leads to a well-defined distribution, which displays a region devoid of scattered ions. Shadow cones play a major role in enhancing the surface specificity of ion scattering techniques, by stopping ions reaching target atoms that lie in deeper layers. An approximation for the shadow cone radius can be defined [15, 25], which depends on the distance behind the scattering atom (l), the incident ion energy (E), and the screening length correction factor (C_{f}). For a screened Coulombic potential, the shadow cone has a radius (r_{c}) given by:

$$r_{\mathrm{c}} = 2C_{\mathrm{f}}\left[\frac{Z_1 Z_2 e^2 l}{E}\right]^{1/2} \tag{3.7}$$

At beam energies of only a few keV wide shadow cones (comparable to interatomic spacings, i.e. $\sim$ 3 Å to 4 Å) lead to high surface specificity [26]. In contrast, for medium and high energies, ions penetrate many layers into the crystal. In this case, use of double-alignment geometry can still give surface specific scattering data. (MEIS experiments use this technique, as discussed below.) Figure 3.3 shows a schematic comparison of shadow cone width between an arbitrary 'low' energy, and a relatively higher energy ion beam.

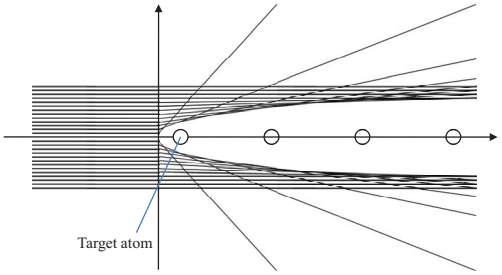

Figure 3.2 Schematic showing production of a shadow cone behind the target atoms (adapted from Woodruff [6]) — a region into which scattered ions cannot penetrate.

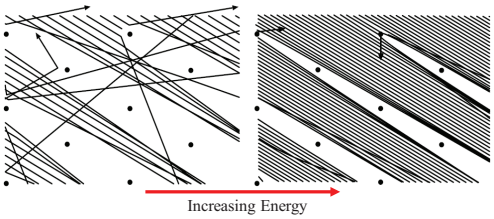

Figure 3.3 Schematic comparison of shadow cone width between an arbitrary 'low' energy, and a 'higher' energy ion beam. As incident ion energy increases, shadow cones narrow.

Trajectory focusing

At the edge of a shadow cone, incident ions are forward-scattered through small angles due to their interaction with the Coulomb potential to create a region of high ion flux (see Figure 3.2); this is known as *trajectory focusing*. The detected ion scattering signal can be enhanced by careful alignment of the crystal so that the high flux region is incident on another target atom [19]. The polar angle at which ions are focused from one surface layer atom to the next adjacent one is known as the *surface critical angle* (a value widely used to give surface layer structural information in CAICISS studies).

Surface critical angle

The critical angle for shadowing is defined as the angle where the atoms are just disappearing in the shadow of their neighbour. Just above the critical angle we expect an enhanced signal, due to trajectory focusing. Simple geometry relates the critical angle (α_c) to the shadow cone radius (r_c) at a distance (l) from its apex and the distance (d) between the two atoms (see Figure 3.4) [27]. These geometric relations can be used to obtain the shadow cone radius for known inter-atomic distances or to obtain the distance for a known shadow cone radius. Measurements of the shadow cones on known surfaces can also be used to obtain information on the interaction potential screening length acting between the ions and the surface atoms (a calculation exploited in the analysis of CAICISS data contained in Chapter 13).

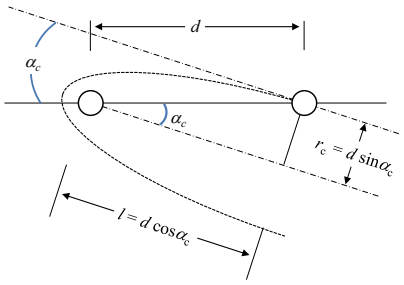

Figure 3.4 Schematic showing the simple geometric relation of the inter-atomic distance (d) and critical angle (α_c) to the shadow cone radius (r_c) at the distance (l). At the critical angle, the right hand atom enters the shadow cone of the left hand atom. (reproduced from Fauster [27]).

Accurate calculation using these expressions relies on accurate knowledge of the shadow cone radius. Investigations by Fauster [27] highlighted deviations between the universal shadow cone expression (Equation 3.7) and experimental datasets. Fauster derived an empirical expression for the TFM model which directly relates the critical angle and inter-atomic spacing [27]; it arises from fitting numerically to many experimental datasets, and thus no approximations need be made as to the shape of the shadow cones:

$$\begin{aligned}\ln(\alpha_c) = 4.6239 &+ [\ln(d) - \ln(aC_f)]\,[-0.0403\ln(A) - 0.6730] \\ &+ \ln(A)\,[-0.0158\ln(A) + 0.4647] \end{aligned} \tag{3.8}$$

$$\text{where} \quad A = \frac{Z_1 Z_2 e^2}{E_0 a C_f}$$

The expression can be rearranged to give an estimate of the value of C_f, if one assumes that the surface layer inter-atomic spacing (d) is known. For a fixed target and incident ion combination at a given energy, A is constant and this equation reduces to a simple power law — a fact which is extremely useful for interpretation of experimental work [14].

3.1.4 Surface vibrations

The thermal vibrations of surface atoms are generally larger than those of bulk atoms; surface atoms are less constrained because of the presence of the discontinuity in the lattice. It is also usual to expect some difference between the vibrational amplitudes parallel to the surface (in-plane) and normal to the surface (out-of-plane), because of the different constraints on the atoms in the outermost layer. Typical outer layer surface vibrational amplitudes are the order of 150 % to 200 % of bulk value [28, 29].

There are two common ways of representing thermal vibrations in a crystal in surface science. Both systems of describing surface vibrations will be employed throughout this thesis. First is an amplitude that defines the root mean square value of displacement from the atom rest positions. Second is *Debye temperature*, which defines a limit to the number of vibrational modes in the solid. A complete description of the Debye model is beyond the scope of this chapter, but importantly, a relation exists [6] to convert between the two descriptions of vibrations, given by Equation 3.9, where: $\langle u^2 \rangle$ is the mean square vibrational amplitude, (θ_D) is the Debye temperature of the surface, (m) is the mass of the surface atom, and (T) is the temperature of the solid.

$$\langle u^2 \rangle = \frac{3\hbar^2 T}{m k_B \theta_D^2} \tag{3.9}$$

3.1.5 Charge exchange, neutralisation and inelastic losses

As an ion travels in the vicinity of a target atom, there is a probability that a charge exchange process can occur. There are several mechanisms for charge exchange, including: (*i*) resonant ionisation, (*ii*) resonant neutralisation, (*iii*) Auger neutralisation, (*iv*) Auger de-excitation, (*v*) quasi-resonant neutralisation, and (*vi*) radiative neutralisation. These processes are competitive and have varying probabilities. For example, resonant neutralisation and resonant ionisation are dominant for alkali metal ions; Auger neutralisation dominates for noble gas ions [6].

In *resonant neutralisation*, an electron from the surface conduction band of the solid tunnels to an excited empty level of the ion. The same process can occur in reverse, in which case it leads to *resonant ionisation*. This process relies on a broadening of the energy levels of the ion, which occurs as the ion approaches the surface. When in close proximity, the valence levels of the ion and surface overlap forming a 'surface molecule'. Incident ions likely to undergo these effects must have their ionisation potentials close to the work function of the metal — a condition typically satisfied by alkali metal ions [6]. It is usually assumed that the neutralisation rate has an exponential dependence on the separation of the ion and the surface [14]. It is therefore clear that at lower ion energies — which produce slower moving ions — neutralisation will be higher, because more time is spent near the surface where neutralisation probabilities are higher.

If an electron from the surface conduction band tunnels into a deep-lying hole in the potential well of an ion, then that electron gives up its excess energy to another conduction band electron, which is then emitted from the surface (*Auger neutralisation*). This electron is known as an *Auger electron*, and has a characteristic energy which is used in analytical techniques such as Auger electron spectroscopy (AES) [14].

3.2 Medium energy ion scattering

Medium energy ion scattering (MEIS) was originally developed as a high resolution variant of RBS. Because MEIS uses medium rather than high energy ions — 100 keV as opposed to 1 MeV — the energy (and depth) resolution are improved.* The energy and angle of the scattered ions are analysed simultaneously, allowing atomic mass, depth, and surface structure to be probed. The specifics of the MEIS system used in these studies — located at the UK MEIS Facility, Daresbury — have been discussed in detail elsewhere [30].

* MEIS has a depth resolution of ~ 5 Å, compared to the ~ 100 Å of RBS [15].

3.2.1 Kinematics

The medium-energy regime typically comprises of incident ions in the range 50 keV to 200 keV. Generally, a low mass ion such as H or He is used to limit surface damage. The studies presented in this thesis all utilise a 100 keV H^+ beam. The use of ions in the medium-energy regime leads to short ion-surface interaction times, and thus less neutralisation of incident ions. Shadow cones are also narrower, which means ions are able to penetrate quite deeply into the bulk of the target crystal. Therefore, careful alignment of the incident ion beam is required to produce surface specificity in MEIS studies.

Target mass information is gained by examining the energy of elastically scattered ions; structural information is obtained from the angle of scattering. More details of how this information is extracted from the raw data are presented in Chapter 4. Depth profiling is also possible — the likelihood of inelastic losses through multiple-scattering events increases as ions penetrate deeper into the target crystal. Depth analysis is not part of the studies presented in this thesis. For more information on depth profiling, refer to the detailed MEIS review articles by Van der Veen [15] and Stensgaard [31].

3.2.2 Beam alignment

By aligning the incident ion beam along a low-index crystallographic direction, shadow cones can be utilised to hide deeper layers of the crystal, thereby gaining surface specificity. Ions scattered from sub-surface layers can collide with surface layer atoms along their outgoing path to the detector, creating further shadow cones. Shadow cones created during these outgoing collisions are generally referred to as *blocking cones* to differentiate between the incoming and outgoing events. The combination of shadowing and blocking cones which creates surface specificity is known as *double alignment* geometry. Figure 3.5 shows a schematic illustration of how a MEIS angular spectrum is produced. Ions scattered from sub-surface layers produce minima in the scattering yield — *blocking features*. The angular locations of blocking features are often labelled by matching to their nearest bulk crystallographic direction. The angular position of the features can be used to determine the structure of the near-surface layers.

Accurate determination of surface structure, however, has some additional complications. The presence of defects, impurities and thermal vibrations in the crystal significantly influences the structure of the blocking features [15]. In practice, computer simulations are required in order to match the scattering data to a suitable structural model. The procedure for data analysis and simulation of trial structures is detailed in Chapter 4.

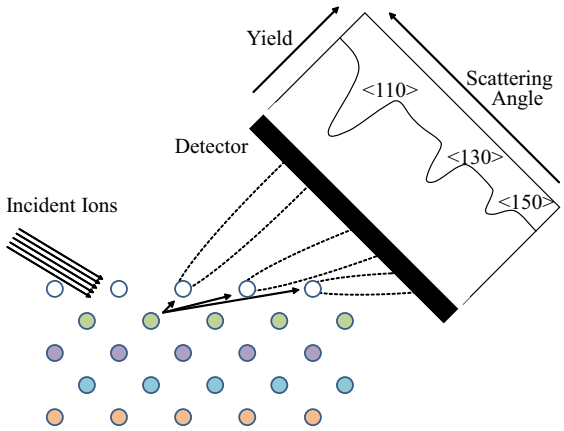

Figure 3.5 Illustration of MEIS blocking minima production in the scattering yield. Ions scattered from sub-surface layers will be prevented from reaching the detector along trajectories containing a surface atom (adapted from Parkinson [30]).

3.3 Co-axial impact collision ion scattering

Co-axial impact collision ion scattering spectroscopy (CAICISS) was originally developed by Aono and coworkers at the RIKEN Laboratory, Tokyo [32,33]. CAICISS is a specific case of low energy ion scattering, which achieves true 180° backscattering through the use of an annular channel-plate detector. Whereas collection of MEIS data requires a detector in the scattering chamber capable of moving around the sample to collect scattered ions from a range of angles, CAICISS scans are completed by rotating only the target surface. The majority of sample manipulation stages have some rotation capability, so the co-axial nature of the apparatus makes CAICISS a truly 'bolt-on' technique.

The specifics of the Warwick CAICISS system as it was inherited at the start of these studies have been discussed elsewhere [3, 34]. Details of a number of modifications and improvements made to the system during the studies presented in this thesis can be found in Chapter 12.

3.3.1 Kinematics

The wide shadow cones produced by the low energy ion beams used in CAICISS studies, give the technique an inherent surface specificity. But, the long ion-surface interaction times mean that many ions undergo charge exchange processes. The increased neutralisation, coupled with the small solid angle of detection, means that the CAICISS signal is in general much weaker than that of MEIS. The Warwick CAICISS system employs an annular channel-plate detector [33,35,36]; it is able to detect both ions and neutrals, helping to increase the usable scattering yield [3]. The cost of using such a detector is that the energy of scattered ions can no longer be measured directly. CAICISS instead relies on a time-of-flight (ToF) system for

target mass separation, which necessitates the production of a pulsed ion beam. The beam typically comprises He^+ ions at energies of up to 5 keV; it is electrostatically chopped in order to produce a zero point of reference for measuring ToF, which can be converted into a kinetic energy characteristic of the target atom species. By collecting multiple ToF spectra at varying crystal polar angles, shadow cone trajectory focusing leads to a series of spectral features which give structural information about the target surface.

Whilst more complex in its implementation, the advantage of the coaxial design of CAICISS is the simplification of the data interpretation and analysis process [17, 37]. For example, in the case that $\theta = 180°$, determination of target mass is simplified, because Equation 3.1 (the kinematic factor) reduces to:

$$\frac{E_1}{E_0} = \left[\frac{(A-1)}{(A+1)}\right]^2 = k \tag{3.10}$$

Only near-perfect backscattering events lead to detection of the scattered ion. This reduces the number of significant multiple-scattering events seen. However, grazing multiple scattering events are key to the technique. CAICISS directly utilises the trajectory focusing effect of shadow cones to increase the backscattering yield. Indeed, most of the structural information which can be extracted from CAICISS spectra arises from focusing of shadow cones between different layers. More details of the analysis of CAICISS spectra are to be found in Chapter 4.

3.4 Low energy electron diffraction

Low energy electron diffraction (LEED) is a widely-used tool for the investigation of surface structure [38–41]. The technique is based on the wave-particle duality properties of electrons which, despite being particles, also exhibit wave-like diffraction. For energies in the range 10 eV to 500 eV, the electron wavelength is comparable to typical lattice spacings in crystalline structures, leading to diffraction [6]. The specifics and theoretical background of LEED are described in numerous other sources [3, 6, 14, 30, 42], so will not be discussed in detail here.

LEED patterns show the surface periodicity in reciprocal space. Features in-between the integer order spots are due to real-space periodicities which are larger than the (1×1) surface lattice. The sharpness and background intensity of the pattern can be used to gauge the quality of the surface — a high background or diffuse spots indicates some degree of disorder, possibly from surface contaminants. For most clean metal surfaces, the presence of spots other than those of integer-order indicates contamination by a well-ordered adsorbate. In many cases, oxide formation can be detected in this fashion [3, 43].

The surface specificity of LEED arises from the limited penetration depth of low energy electrons (< 100 eV). In most materials this is limited to around 20 Å at low energies [3]. The short mean free path makes it highly unlikely that electrons will escape from deep within the crystal without undergoing multiple inelastic scattering events, making the technique ideal for surface structure determination [6].

3.5 Auger electron spectroscopy

Auger electron spectroscopy (AES) has been used in this thesis to establish whether prepared surfaces are free from contamination. The capabilities of AES far outstrip the details relevant to its use in this thesis. For a full discussion of AES, the reader is referred to the book by Briggs and Seah [44].

AES utilises a beam of energetic electrons — typically between 1 keV and 10 keV. An incident electron ejects a core level electron from a surface atom. Subsequently, an electron from a higher energy level drops into the core hole, ejecting an electron from a higher level to conserve energy — an *Auger electron*. The process is shown schematically in Figure 3.6. The Auger electron has a kinetic energy characteristic of the atomic species of the surface atom, and the energy levels involved in the emission process. As such, a single atomic species may have several characteristic Auger electron energies. An AES spectrum contains peaks in intensity at energies consistent with certain energy level transitions, allowing target species to be identified. For elements with low atomic number ($Z < 20$) — such as typical surface contaminants C, O, S — Auger electron emission is the dominant process, thus AES is an ideal technique for monitoring surface cleanliness [45].

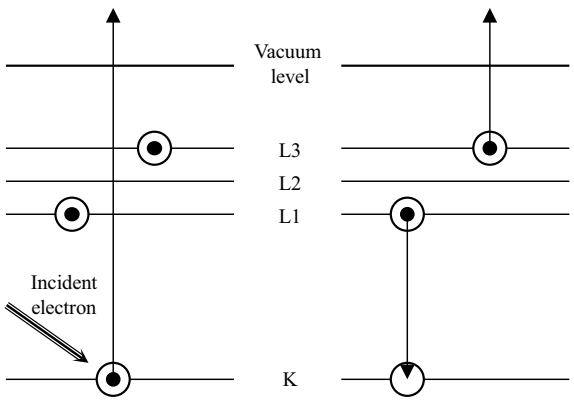

Figure 3.6 Schematic showing the process that produces an Auger electron. Left: a core level electron is ejected by an incident electron. Right: an electron from a higher level fills the core hole, and an Auger electron is ejected to conserve energy.

CHAPTER 4

Ion Scattering Data Analysis

In all but the simplest of cases, extracting useful information from ion scattering techniques is not as straightforward as simply applying the scattering formulae discussed in Chapter 3. Many factors influence scattering spectra for both MEIS and CAICISS, including: surface vibrations, surface reconstruction, multiple-scattering events, and ion-surface interaction potentials. A quantitative description of the atomic structure and elemental composition of the near-surface region can only be obtained by comparing experimental data with computer simulations of trial structures. This chapter introduces the simulation codes used for analysis of MEIS and CAICISS data, and outlines the process of data interpretation for each technique.

4.1 Simulation codes

There are numerous different approaches to simulation of ion scattering spectra, and various code solutions have been written. Generally, they fall into one of two categories: Monte Carlo simulation, or molecular dynamics simulation. This section discusses the premise behind each, and then introduces the optimised VEGAS and FAN codes used to create computer simulations for this thesis.

Monte Carlo ion scattering simulations — such as the MARLOWE codes (Robinson [46]) — allow the complete trajectory of an ion to be followed from its origin at the 'source', through the scattering event, to its detection at the 'detector'. Whilst providing a very thorough treatment of the ion-surface interaction, these codes are generally not well suited to the analysis of data with a restricted scattering angle range, due to the large number of irrelevant ion trajectories which are simulated. Large amounts of computation are required in order to generate enough qualifying scattering events for simulation in the angular range of the experimental data [3].

In the molecular dynamics approach, the motion of a given number of particles is calculated over a period of time, with the motion governed by an inter-atomic pair-wise potential. As with Monte Carlo simulations, the molecular dynamics approach simulates a large number of irrelevant trajectories. Due to the additional calculation of the motion of all the target particles in the surface region during the scattering event, molecular dynamic simulations are

significantly more time consuming than their Monte Carlo counterparts; they are not widely applied to ion scattering techniques. The KALYPSO codes (Karolewski [47]) employ just such a molecular dynamics approach. Whilst the package was designed primarily for simulation of sputtering events, attempts have been made to apply it for CAICISS simulation with some success [48, 49].

4.1.1 The VEGAS codes

The VEGAS codes (Tromp [50, 51]) are essentially a Monte Carlo simulation, but with some refinements to help reduce the number of irrelevant trajectories simulated. It has been shown by Tromp et al. [50] that the approximations made in the VEGAS codes are valid when applied to MEIS. Rather than simulating the full path of ions, the new approach of the VEGAS codes was to calculate hitting and detection probabilities for each of the target atoms.

Starting locations above the surface are randomly chosen, and paths traced along the required incident direction until an elastic collision with a target atom is experienced. By simulating a large number of random tracks, the approximate hitting probability for each target atom is compiled. By assuming that any inelastic collisions will only alter the ion beam energy by a small fraction, VEGAS treats the energy of the outgoing scattered beam as having undergone a single elastic collision event. In this scenario, one can use the principle of time-reversibility, which implies that the detection probability is equivalent to the hitting probability for an ion originating at the detector. Thus, all that need be calculated is the hitting probability for each target atom, firstly for the incident geometry, and subsequently for each required (time-reversed) outgoing direction. Finally, the hitting and detection probabilities are multiplied together to obtain the scattering yield from each atom [30].

In this approach, all of the simulated scattering events contribute to the final spectrum, saving vast amounts of computational time in comparison to other Monte Carlo methods and molecular dynamics methods. The approach of VEGAS has one specific drawback which prevents it being applied for CAICISS analysis; it can only be applied when the chances of inelastic multiple scattering events are low. For this to be the case, shadow cone radius must be small and therefore this simulation method is limited to the higher incident ion energies used in MEIS.

4.1.2 The FAN codes

The FAN codes (Niehus [16]) were specifically designed for application to techniques concerned mainly with detection of backscattered ions — such as CAICISS. Only trajectories which will reach the detector are calculated, giving FAN a significant performance advantage over the other codes discussed here. The FAN codes have been successfully applied to numerous systems [3, 48, 49].

In this case, Monte Carlo methods are not employed. Target atoms are treated as emitters of ions. The incident trajectories are calculated by tracing out a 'fan' of emission angles at the primary ion energy. The outgoing trajectories are then calculated using the scattered particle energy. The procedure is similar to that of the VEGAS codes, but specifically designed to handle some additional effects of low energy incident ions — most notably the ion-surface interaction potential can be customised, allowing correction factors to be included in the simulation [3]. The program does not, however, include inelastic energy losses along the incident trajectory, which may slightly affect the radius of the shadow cones. And the package is currently limited to 1500 target atoms, and only three species of target atom, making the simulation of more complex structures (e.g. quasicrystals) rather problematic.

4.2 Objective optimisation: R-factors

Visual comparison of experimental spectra with computer simulations can be helpful initially — especially when presented with a number of possible structural models which differ significantly. However, visual inspection is far too subjective for accurate surface characterisation, and thus an objective method is required. To this end, Noakes et al. [52] investigated the use of a reliability factor in MEIS analysis.

A reliability factor — or *R-factor* — is generally based on a sum of squared deviations between experimentally measured and theoretically computed intensities, after appropriate weighting and normalisation. For MEIS, a reduced chi-squared R-factor was found preferrable [52]. To correct for differences in the absolute intensity between experimental (I_e) and simulated (I_s) spectra, a scaling factor (λ) is applied to the simulation. The scaling factor is calculated by summing the total counts in each spectrum and taking a ratio. The R-factor is given by:

$$R = \left(\frac{1}{N}\right) \sum_{i}^{N} \left[\frac{(I_\mathrm{e} - \lambda I_\mathrm{s})^2}{I_\mathrm{e}}\right] \tag{4.1}$$

Structural determination often requires analysis of multiple scattering geometries. In this case, R-factors from each dataset are combined to form an overall R-factor; individual R-factors are weighted by the number of points in the respective datasets. A benefit of using a chi-squared R-factor is that the error on a particular structural parameter can be determined by creating plots of the R-factor variation with parameter value — *R-space plots* — and measuring the gradient. The second derivative is taken at the minimum point of the R-factor curve [53]; the parameter error estimate is then given by:

$$\sigma = \sqrt{2}\left[\left.\frac{d^2 R_\chi}{dZ^2}\right|_{R=R_{\min}}\right]^{-1/2} \tag{4.2}$$

This reliability factor has proven to be successful when applied to MEIS data [14,29,30,52]. For CAICISS analysis, no successful attempt has yet been made to apply an R-factor. This thesis trials the use of the MEIS R-factor, because it is simple to apply and to calculate parameter errors. As the reader will see in future chapters, application of this R-factor was not as straightforward as was hoped.

4.3 Automated structural fitting

Simulation and structural fitting of complex systems can be extremely time consuming. Models will often have upwards of six structural parameters. Obviously, manually simulating all possible parameter values in order to find the best fit is out of the question. Ideally, one would input a range for each structural parameter, and computer simulations would be conducted on all possible permutations; the lowest R-factor would be returned, along with the gradient of each parameter around that minimum, and that would provide the structural solution. In reality the amount of computation required — even for simple systems — would be unfeasibly large.

The implicit filtering for constrained optimisation (IFFCO) codes (Kelley) [54] provide a solution. IFFCO is a projected quasi-Newtonian algorithm for problems with bound constraints and many local minima. The application of the IFFCO algorithm to the MEIS and CAICISS fitting process should reduce the number of permutations required in order to find a suitable structural solution. The basic architecture is simple. The IFFCO algorithm runs as the driving program, with a user callback provided to allow customisation and application to different problems. The returned value of the user callback is what the algorithm will attempt to minimise. Full details of the operation of the algorithm can be found in the documentation by Kelley [54]. In the case of ion scattering techniques, the user callback will:

1. Run a simulation with the current structural parameter values.
2. Compare the result to experimental data and calculate an R-factor.
3. Repeat for all datasets.
4. Return the overall r-factor.

IFFCO will then attempt to minimise the R-factor by varying structural parameter values within the defined intervals. An automated fitting routine already exists for MEIS. No such equivalent yet exists for CAICISS — because no R-factor has been applied to CAICISS until now. An IFFCO-based fitting routine for CAICISS was developed as part of this thesis.

The specific versions of the MEIS and CAICISS IFFCO codes used for analysis in this thesis will henceforth be referred to jointly as SOAR — the structural optimisation automation routine. Additional features added to SOAR as part of this thesis that were not part of the original IFFCO codes include:

1. The ability to map out the R-factor variation for each structural parameter independently to help identify valid intervals for each structural parameter.
2. Automatic calculation of error estimates for all structural parameters once a candidate solution has been located by the IFFCO algorithm.
3. A mode which allows all parameter values to be specified and will produce output that can be imported directly into a suitable plotting package — most helpful when producing spectra of the final optimised structural solution.

4.4 Data preparation

MEIS data are acquired as a two-dimensional tile of energy versus scattering angle. The detector employed at the UK MEIS facility collects data in $\sim 20°$ angular windows. CAICISS data are acquired as a series of ToF spectra at individual polar angles, then compiled into a two-dimensional tile of ToF versus polar angle. Very similar information is contained in the tiles, as scattering energy (MEIS) is essentially equivalent to ToF (CAICISS) due to conservation of energy and momentum. Figure 4.1 shows an example tile for each technique acquired from the clean Cu(100) surface. A false colour scale is used to indicate the number of counts represented by each pixel; on the left — the MEIS data tile — scattered energy versus scattering angle. On the right — the CAICISS data tile — ToF versus polar angle.* White represents zero detected scattered ions/neutrals; blue, a low number of counts; red, a

* MEIS incident beam: 100 keV H^+, $\langle 110 \rangle$ incidence.
CAICISS incident beam: 3 keV He^+, $\langle 100 \rangle$ azimuth.

high number. The number of events detected is dependent on the efficiency of the detector, and the intensity of the incident ion beam.

Tiles are processed in a similar way; in both cases a polygon is placed around a region of interest, and the contents projected onto either the angular or energy axis. The blocking features in angular spectra describe the structural characteristics of the near-surface region of the crystal. Energy spectra are of interest when conducting depth profiling and compositional investigations. The VEGAS and FAN codes simulate angular spectra, allowing for simple comparison between experiment and simulation. They also allow compositional profiling via comparison of detected and simulated intensities for each target surface species.

4.4.1 Cross-section correction

An additional cross-section correction is needed for MEIS spectra, because of the varying scattering angle. The variation in scattered energy due to the scattering cross-section can clearly be seen in the example MEIS tile displayed in Figure 4.1. No cross-section correction is needed for CAICISS, because all ions/neutrals detected are for near-perfect 180° back scattering events. The correction is simple: a function that can be divided through the data in order to remove the angular dependence of the spectra [18]:

$$f(\theta) = \sin^4(\theta/2) \tag{4.3}$$

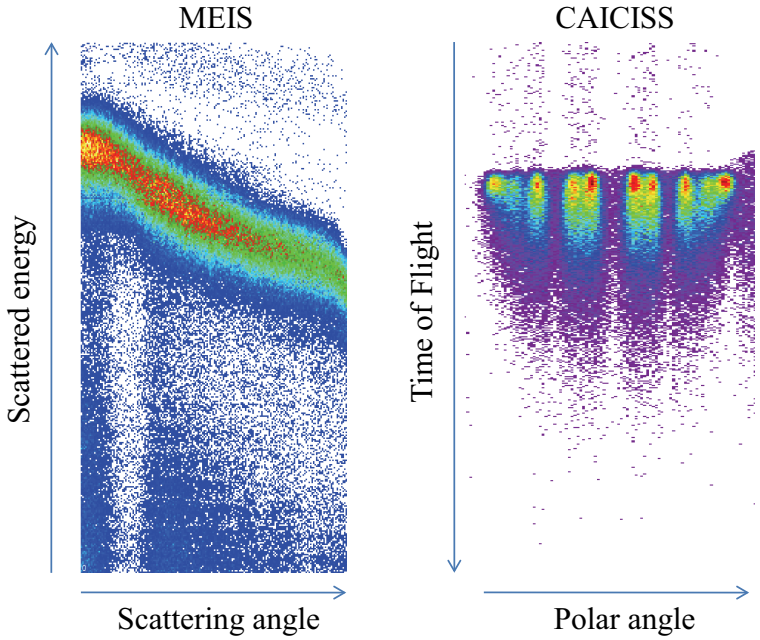

Figure 4.1 Examples of two-dimensional data tiles acquired from clean Cu(100) using MEIS and CAICISS. Left: MEIS data tile of *Scattering energy v. Scattering angle*. Right: CAICISS data tile of *ToF v. Polar angle*. A false colour scale represents the number of detected scattered particles, with red showing a high number of counts.

4.5 The fitting process

The fitting process is started by identifying possible models. 'Bulk-like' versions are constructed with as many surface layer atoms as possible in bulk lattice sites, whilst still retaining the unique periodicity of the model. An R-factor is produced for each of these *bulk fits* to act as a baseline for fitting. It is often the case that some models can be excluded based solely on R-factor analysis of bulk fits [30].

Next, relevant structural and vibrational parameters for each model are identified. Most models contain some parameters for altering the inter-layer spacings. Some more complex models also contain: surface rumpling parameters, lateral shifts, and vibrational amplitude enhancements. An addition for the CAICISS SOAR codes is the ability to vary the screening length correction factor in an automated way, allowing it to be included as an additional 'structural' parameter. Once parameters have been identified, SOAR is used to create R-space plots to identify physically sensible bounds for each of the structural parameters. With intervals for each parameter in place, SOAR runs the IFFCO algorithm [54] to generate an optimised structural solution. SOAR outputs the final optimised spectra, along with parameter values and associated error estimates.

Development of the SOAR codes, although time-consuming in its own right, has allowed for greatly accelerated data analysis, and improvements are still being made. Some possible future developments for SOAR are detailed in Chapter 14.

Part II
The Cu(100)/Sn System

List of Chapters

CHAPTER 5

Introduction to the Cu(100)/Sn System

The interaction of metallic species with the Cu(100) surface has been widely investigated due to potential applications in metal-on-metal epitaxial growth and industrial catalytic processes [40, 55–66].

Such bi-metallic systems exhibit a large range of modified behaviour, both structurally and electronically. Oftentimes complex alloy structures are formed in the near-surface region. Examples of such systems are: Cu/Sn, Pb/Sn, Cu/In, Cu/Pb, Pt/Sn [67–75]. The Cu(100)/Sn system is a good example of a complex bi-metallic system. A large lattice mismatch of ~ 10 % between tin and copper contributes to a complex yet well defined series of ordered phases formed under room temperature exposure to Sn [76].

The Cu(100)/Sn system structures were first systematically studied by Argile and Rhead [77] using LEED and AES. They concluded the existence of four ordered structures, at sub-monolayer Sn coverage. The surface structures were re-interpreted by McLoughlin et al. [78, 79] using analysis of LEED I-V (intensity versus voltage) experiments. They proposed structural models for the three lowest coverage phases, corresponding to Sn coverages of 0.21 ML, 0.33 ML, and 0.50 ML, henceforth referred to as Phase 1, Phase 2 and Phase 3 respectively. Phase 1 was observed to possess a $p(2\times2)$ reconstruction with a large number of split spots; Phase 2, a $p(2\times6)$, and Phase 3 a modified $c(2\times2)$ more precisely determined as $p(3\sqrt{2}\times\sqrt{2})\mathrm{R}45\,^{\circ}$. Phase 4 has a coverage of 0.625 ML, with a $c(4\times4)$ LEED pattern [77]. Here, ML is defined as the density of Cu atoms on the clean Cu(100)-(1×1) surface.

Further studies by Martínez-Blanco et al. [80] using LEED and X-ray diffraction have suggested the existence of a further phase — an 'intermediate' between Phase 2 and Phase 3 — with a Sn coverage of 0.45 ML and complex $c(4\times8)$ reconstruction. More recent studies [81–83] have focused on using a variety of techniques to attempt to find structural models for each phase. Martínez-Blanco et al. [80] have published a phase diagram which nicely summarises the current position of research on the system, which is reproduced in part in Figure 5.1. The phase boundaries shown are approximate due to phase co-existence, but loosely agree with both the early studies of McLoughlin et al. [78] and more recent work of Lallo et al. [81].

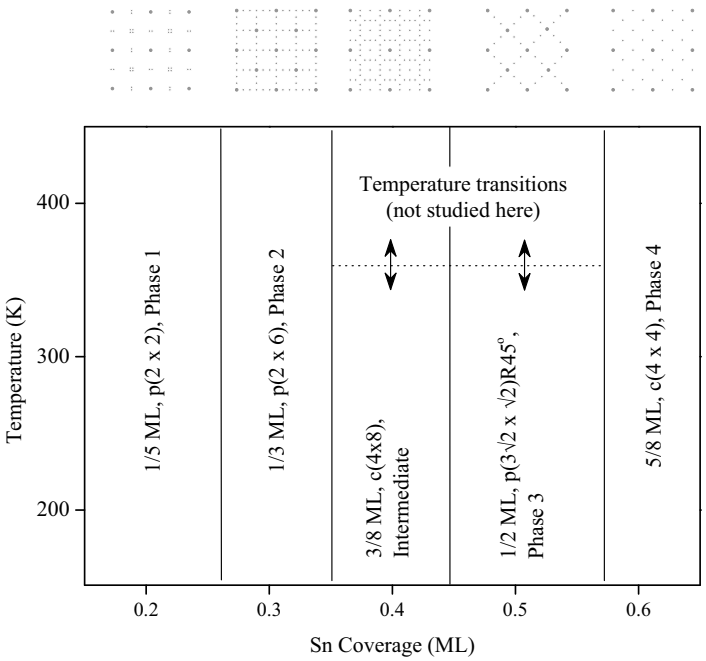

Figure 5.1 Phase diagram of the Cu(100)/Sn surface reconstructions, showing approximate Sn coverage and sample temperature dependence.

The objective of the work outlined in these chapters was to determine the structure and composition of each one of the phases observed in previous studies using ion scattering techniques. As already discussed in Chapter 3, ion scattering is ideally, and almost uniquely, suited to the study of crystallographic structure; the data collected give real-space information about atomic nucleus positions [38,84]. MEIS, CAICISS, LEED and AES data were collected. LEED was used to confirm the existence of each of the five observed phases, with AES used to ensure no contamination of the surface. A combination of MEIS and CAICISS was then used to provide a full structural fit for each phase.

5.1 Experimental details

Experiments were carried out in two locations. MEIS data were collected from the UK MEIS Facility, Daresbury Laboratories. CAICISS data were collected from the Warwick CAICISS system. Both systems have LEED and AES capability and down turned ports for addition of deposition cells containing liquid sources. MEIS and CAICISS are both ion beam techniques, but the difference in energy regime means that they provide two complementary views of the system. The information available by application of each technique is discussed in Chapter 3 and Chapter 4.

The Cu(100) crystal was purchased precut to an accuracy of 0.1°, and mechanically polished prior to being loaded into each of the scattering chambers. Once loaded, the crystal

was further cleaned by repeated cycles of low-energy IBA (1.5 keV Ar^+ for 20 minutes, followed by annealing to 750 °C for 60 minutes), as suggested by Musket et al. [85]. The surface cleanliness was verified using a combination of LEED and AES. The usual contaminants (C, O and S) were observed [85] with AES when the sample was first loaded into the chambers. IBA cycles as described were sufficient to remove all contamination. LEED was checked for a sharp (1×1) pattern with low background intensity.

Sn (with a purity of 5N) deposition was carried out using a water-cooled Knudsen-cell evaporator (W.A. Technology), held at a steady temperature of 950 °C. This provided a constant deposition rate of 0.012 $MLmin^{-1}$, calculated using the established coverages of observed LEED patterns. In particular, Phase 3 was used as a fixed point for calibration, because it is reported in previous studies [78] to have a coverage of approximately 0.50 ML. Deposition was conducted in stages by opening the Sn source for 1 minute at a time, with LEED checked after each deposition. The chamber base pressure remained below 5×10^{-10} mbar throughout deposition of all phases.

5.1.1 Scattering geometries

MEIS data for each phase were collected from the ⟨110⟩ and ⟨211⟩ incident directions. These directions provide surface specificity through shadowing of deeper layers. Figure 5.2 and Table 5.1 show the scattering geometries obtained for each of the incident directions collected. In all cases three datasets were taken for each incident direction, allowing a large range of scattering angles to be examined. Figure 5.2 also clearly demonstrates the surface specificity of MEIS for these directions of a face-centred cubic (fcc) crystal. Incident ions in the ⟨110⟩ and ⟨211⟩ directions can be seen to illuminate only 1 and 2 layers respectively.

Table 5.1 Expected MEIS bulk blocking features in each incident direction for a fcc(100) crystal. θ is the scattering angle in degrees. *hkl* is the crystallographic direction of the feature (see Figure 5.2 for an illustration).

⟨110⟩ incidence			⟨211⟩ incidence		
#	θ(degrees)	*hkl*	#	θ(degrees)	*hkl*
1	56.31	⟨150⟩	1	74.21	⟨122⟩
2	63.43	⟨130⟩	2	79.96	⟨233⟩
3	71.57	⟨120⟩	3	90.00	⟨111⟩
4	75.96	⟨350⟩	4	98.05	⟨433⟩
5	90.00	⟨110⟩	5	109.48	⟨211⟩
6	108.43	⟨210⟩	6	125.27	⟨411⟩
7	116.56	⟨310⟩	7	144.74	⟨100⟩
8	135.00	⟨100⟩			

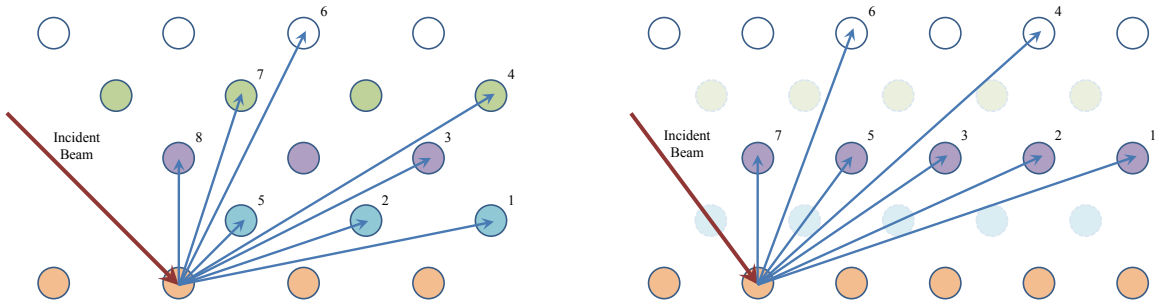

(a) Ion beam incident in ⟨110⟩ direction (b) Ion beam incident in ⟨211⟩ direction

Figure 5.2 MEIS scattering geometries for the ⟨110⟩ and ⟨211⟩ incident directions on the Cu(100) surface. Blocking features are numbered in order of increasing scattering angle (see Table 5.1 for exact values).

Ordinarily, MEIS datasets would provide absolute scattering yield information which can be used to distinguish between overlayer and alloy models when compared to a control sample. Unfortunately, due to problems with the current integrator during this investigation, there was a large variation in the number of counts obtained for each dataset. Analysis can proceed without this additional information, but the MEIS data are likely to be less conclusive.

CAICISS data for each phase were collected from polar angle scans in the ⟨100⟩ and ⟨110⟩ azimuths. Figure 5.3 shows the scattering geometries obtained for each of the azimuths collected. The back-scattering features seen arise from the focusing of ions in shadow cone edges. Scanning in two azimuths allows the structure of the crystal to be probed down to the sixth atomic layer.

5.2 Results: Study of the Cu(100) clean surface

The clean Cu(100) surface was also examined during this investigation. MEIS data collected are presented here. CAICISS data were also collected, but results are not presented in this chapter.* Data were analysed in accordance with the procedures defined in Chapter 4.

MEIS data collected from the clean surface serve as a good example of the different blocking features obtained from the near-surface region and the bulk crystal. Figure 5.4 shows a comparison of processed MEIS spectra for near-surface and bulk clean surface data in the ⟨211⟩ incident beam. The surface data clearly shows less contribution from fine blocking features. The bulk spectrum has lower counts because ion neutralisation probability rises dramatically the deeper they penetrate into the crystal.

* The CAICISS data was of lower quality and less comprehensive than equivalent data for a later chapter investigating ion-surface interaction potentials (see Chapter 13).

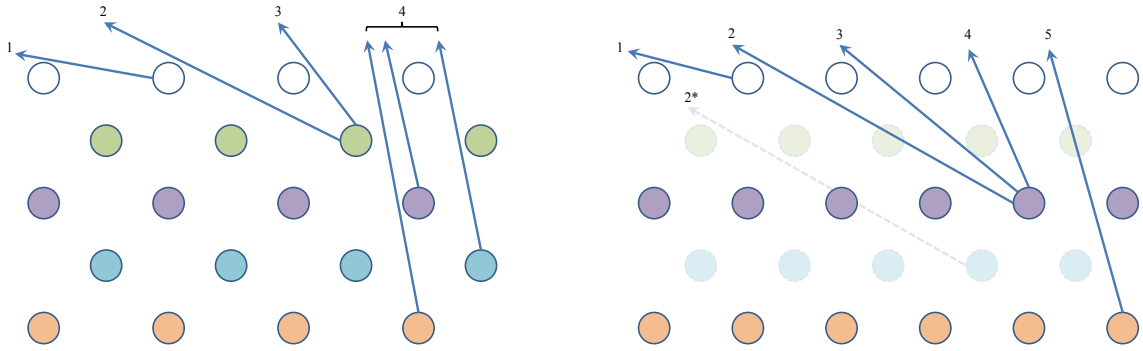

(a) Rotated about polar axis in ⟨100⟩ azimuth (b) Rotated about polar axis in ⟨110⟩ azimuth

Figure 5.3 CAICISS scattering geometries for polar scans in the ⟨100⟩ and ⟨110⟩ azimuths on the Cu(100) surface. Back-scattering features are numbered in order of increasing polar angle.

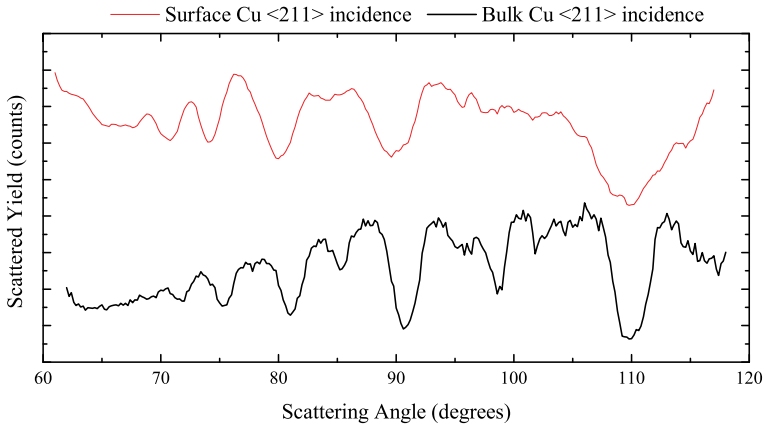

Figure 5.4 Comparison of blocking features from the near-surface region and bulk crystal. Processed MEIS Cu scattering data from the ⟨211⟩ incident beam. The near-surface region displays modified features due to changes in atomic structure. Surface specificity has been gained in this study through the use of shadow cones which hide deeper layers of the crystal.

MEIS data were compared with VEGAS simulations of a bulk Cu(100) crystal surface — all atoms are in bulk lattice positions and with bulk vibrational amplitudes: An R-factor of 2.79 was obtained. R-space plots (shown in Figure 5.5 and Figure 5.6) illustrate the variation of R-factor for each parameter, allowing intervals for SOAR to be narrowed. Four of the five plots show a single minimum. Surface vibrations in the plane of the surface show two minima, but one is over 400 % of the bulk value, which seems unlikely given that typical outer layer enhancements of surface vibrational amplitudes are in the order of 80 % to 100 % of bulk value [28,29].

SOAR optimisation leads to a better fit between data and simulation, and hence a reduced value of 2.34 for R-factor. Figure 5.7 and Table 5.2 show the optimised spectra and final parameter values after IFFCO fitting. In-plane vibrations show no enhancement, which is the expected result give that the local environment is unmodified from that of the bulk

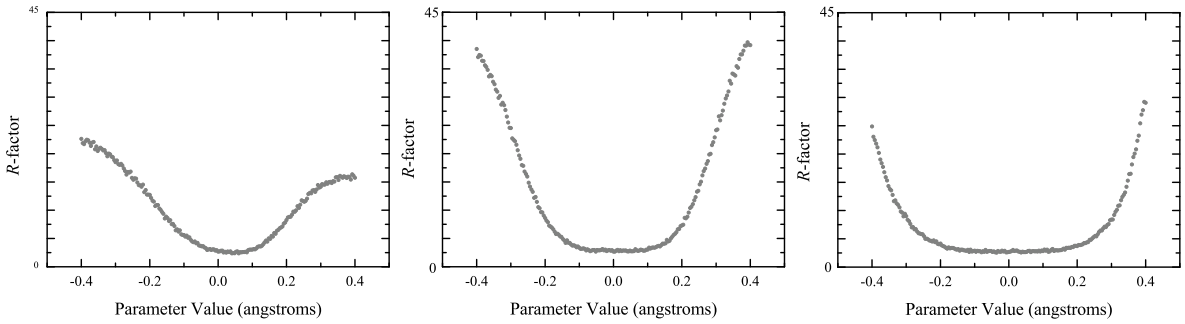

(a) First inter-layer spacing (b) Second inter-layer spacing (c) Third inter-layer spacing

Figure 5.5 MEIS R-space plots for clean Cu(100) surface structural parameters. Each of these parameters represents a change in the surface inter-layer spacings from that of the bulk crystal.

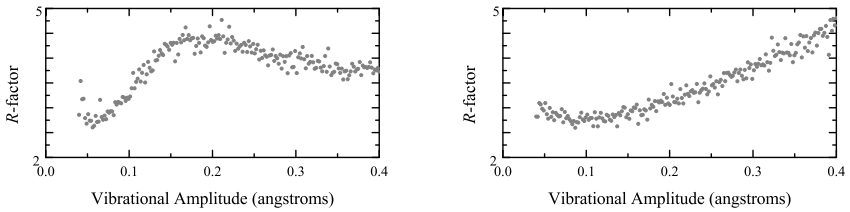

(a) Vibrations in-plane (b) Vibrations out-of-plane

Figure 5.6 MEIS R-space plots for clean Cu(100) surface vibrational parameters. These parameters define the surface layer atom vibrational amplitudes, split into two contributions parallel and perpendicular to the surface plane.

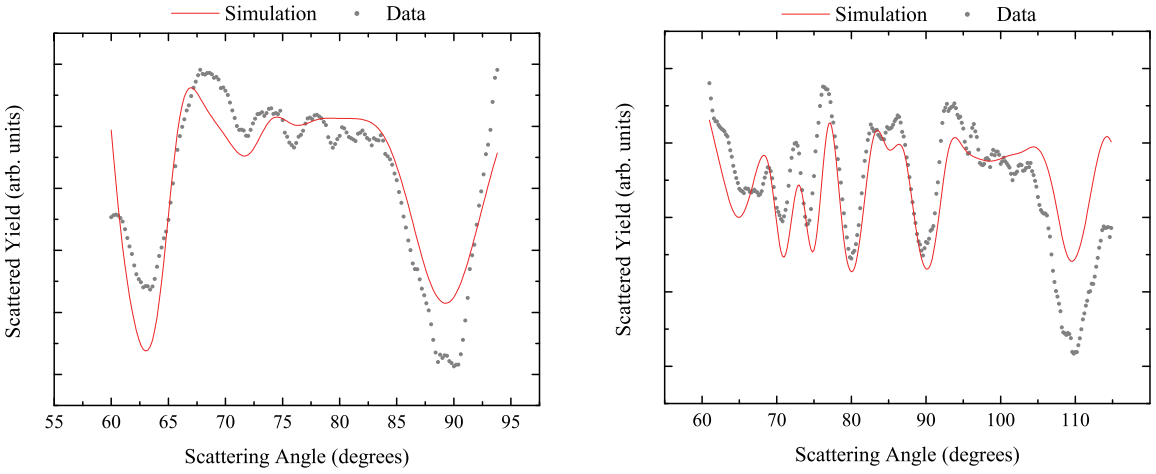

(a) ⟨110⟩ incidence (b) ⟨211⟩ incidence

Figure 5.7 Optimised MEIS fits from SOAR for the clean Cu(100) surface. Data were collected from two incident beam geometries. Simulations were conducted using the VEGAS codes [5].

Table 5.2 Optimised MEIS parameter values from SOAR for the clean Cu(100) surface. Inter-layer spacing changes are relative to the bulk value of 1.81 Å. Surface vibrational amplitudes are absolute values to be compared with the bulk Cu vibrational amplitude: 0.07 Å [76].

Parameter values (Å)		
1	Cu first interlayer spacing change (Δ_{12})	-0.049 ± 0.072
2	Cu second interlayer spacing change (Δ_{23})	$+0.030 \pm 0.113$
3	Cu third interlayer spacing change (Δ_{34})	$+0.025 \pm 0.151$
4	Cu in-plane vibration amplitude($V_{\|\|}$)	0.070 ± 0.047
4	Cu out-of-plane vibration amplitude($V_{\perp}$)	0.084 ± 0.081

crystal. This should not be the case for out-of-plane vibrations, because of the modified potential resulting from missing atoms at the interface — an enhancement to 119 % of bulk values is observed. Inter-layer spacing changes show some large error estimates. The large errors result from the flat R-space plots already seen in Figure 5.5.

A compilation of previous studies by Rodriguez [4] shows that the changes in the first and second inter-layer spacings observed in this study are largely consistent with the experimental results of many other authors. Most observe a change in the first inter-layer spacing of around -1 %, and a change in the second inter-layer spacing of up to $+2$ % — compared to values of -2.7 % and $+1.6$ % in this study. It is difficult to be confident of the result of MEIS data analysis considering the large error margins, but the alternating pattern of contraction and expansion in the outermost two layers does seem to be reproduced.

CHAPTER 6

Cu(100)/Sn: Phase 1

In the original LEED work by Argile and Rhead, no atomic structure was proposed for Phase 1. It was referred to simply as a 'complex' pattern, although the authors did suggest that the observed spot splitting indicated the presence of anti-phase domains [77]. McLoughlin et al. expanded on that work; they observed Phase 1 at an estimated coverage of 0.21 ML and proposed some models based on a $p(2\times2)$ superstructure — which would reach maximum perfection at a coverage of 0.25 ML. They concluded that it was reasonable to suggest that Phase 1 may be explained in terms of a $p(2\times2)$ periodicity with 'light' domain walls [78]. Similar domain walls have been observed in other studies [86–88]; in the Cu(100)/Pb system by Bocquet and Gauthier [86]; in the Rh(100)/La system by Kildemo et al. [87]; in the Cu(100)/Bi system by Meyerheim et al. [88].

The results of later scanning tunnelling microscopy (STM) and normal incidence x-ray standard wave (NIXSW) studies by Cafolla et al. support the idea of domain walls, with anti-phase alignment of Sn atoms in neighbouring domains [89]. Three types of domain wall are proposed, along with domains both larger and smaller in size. The authors also concluded that Sn atoms adopt a single well-defined adsorption site on the surface, most likely a four-fold symmetric site, which may be a four-fold hollow site, substitutional alloy site, or atop site. The various types of domain walls are classified primarily by their dimensions. Domain walls containing one, three and five rows of copper atoms are observed with a distortion of the copper rows due to elastic strain caused by the mismatch in radii between the Sn and Cu atoms. The authors found that they were unable to distinguish between the alloy and overlayer models using data from LEED and NIXSW, but from the magnitude of the corrugation in the $p(2\times2)$ domains viewed by STM it was concluded that Sn atoms most likely form a substitutional alloy [89].

This chapter examines MEIS and CAICISS data collected on Phase 1. Data are compared to computer simulations based on structural models proposed by previous studies, and structural parameters are optimised using the SOAR codes.* All of the models proposed have

* The analysis of MEIS and CAICISS data is described in detail in Chapter 4.

a lower coverage than that observed by McLoughlin et al. previously, although this is due mainly to the small dimensions of the domains relative to the dimensions of the domain walls. If larger domains were included, such as those seen by Cafolla et al. [89], then the coverage would obviously increase.

6.1 Structural models

The four structural models which will be tested, shown in Figure 6.1, are based on the previous studies described above. The first, (a), is a substitutional surface alloy model. The others are all overlayer models, but with Sn atoms in varying adsorption sites — (b) atop, (c) bridge and (d) four-fold hollow. MEIS should allow the different sites in the overlayer model to be resolved, but it may not be able to distinguish between alloy and overlayer models. The additional application of CAICISS, which has higher surface specificity, should allow the structure to be determined completely.

All of the models have a large number of atoms per unit cell in order to achieve the required missing row periodicity. The anti-phase domains of the original McLoughlin models compound this problem by quadrupling the size of the unit cell. In addition to the surface periodicity, the crystals are modelled down to the sixth atomic layer in order to accurately reproduce the blocking features of the near-surface Cu region.

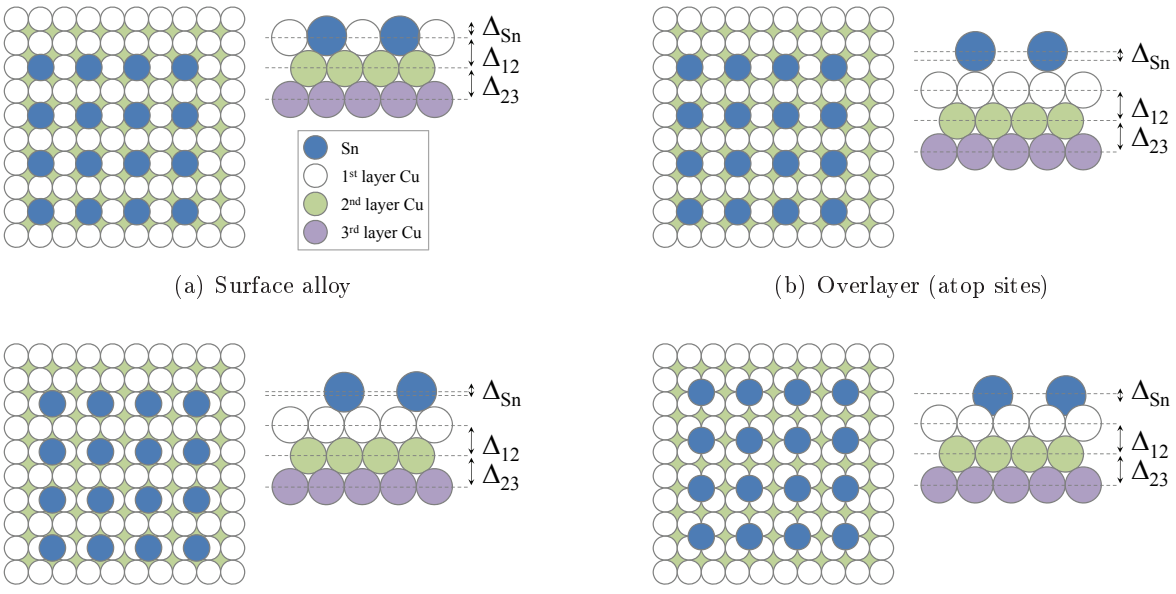

(a) Surface alloy

(b) Overlayer (atop sites)

(c) Overlayer (bridge sites)

(d) Overlayer (hollow sites)

Figure 6.1 Schematics of the four trial structures for Phase 1. Atomic positions and structural parameters used for fitting are shown. Based on models proposed from LEED I-V studies by McLoughlin et al. [78].

The large number of atoms poses problems, especially for the FAN simulation code used for CAICISS analysis. The software is old and has restrictive limits on the total number of atoms that can be modelled, so it has been necessary to simplify the periodicity of the models in order to reduce the unit cell size. The removal of the anti-phase domain boundaries should not adversely affect ion scattering data — the nature of the adsorption sites will not be altered by the simplified models. Specifically, the location of all features should remain the same in angle, but there will be some small changes to their relative intensities because of the additional presence or absence of atoms. This was seen as a reasonable compromise to the computation problem given that — according to the STM results of Cafolla [89] — the choice to model domains with dimensions of 4×4 appears to be somewhat arbitrary anyhow.

6.2 Results

Figure 6.2 shows the LEED pattern obtained for Phase 1 at 91 eV after 18 minutes of Sn deposition; it is in excellent agreement with that seen by Argile and Rhead. Using the calibrated deposition rate of 0.012 MLmin^{-1}, Sn coverage was estimated to be 0.22 ML. This is in agreement with the coverage obtained by McLoughlin et al. [78] (0.21 ML) for a similar LEED pattern. AES scans (see Figure 6.3) — which showed C and O contamination when the sample was first loaded — showed no C or O after cleaning.

Having confirmed the reconstruction as that of Phase 1 using a combination of LEED and AES, MEIS and CAICISS data were collected in the geometries detailed in Section 5.1.1. Analysis procedures for MEIS and CAICISS data are discussed in detail in Chapter 4.

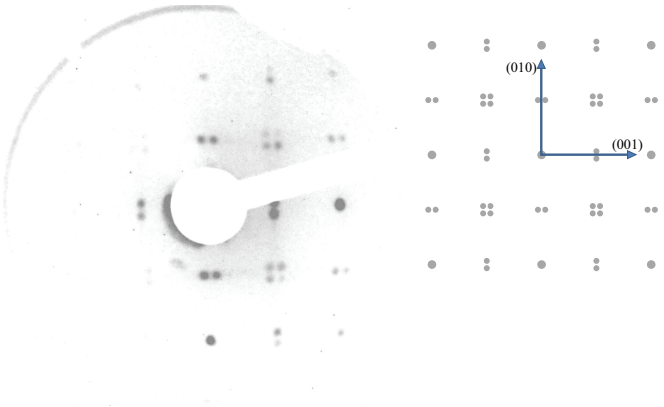

Figure 6.2 Illustration of the LEED pattern obtained for Phase 1 at 91 eV. The calibrated deposition rate of 0.012 MLmin^{-1} gives an approximate coverage of 0.22 ML after 18 minutes of Sn exposure. A photograph and a sketch are shown; the sketch is reproduced from the work of Argile and Rhead [77].

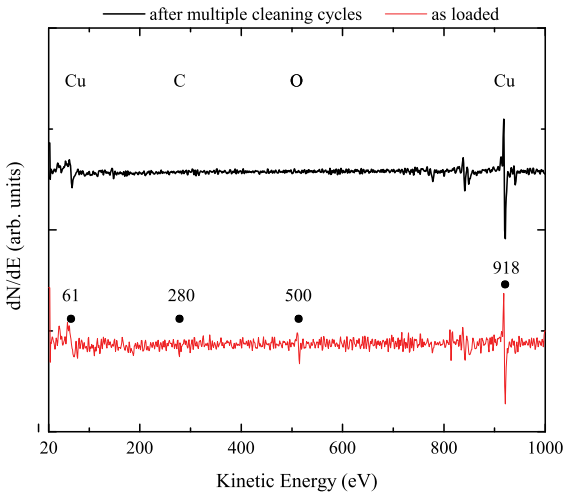

Figure 6.3 AES spectra before and after IBA cleaning cycles were performed. Bottom (in red) is the 'as loaded' spectrum. Top is the spectrum obtained after cleaning.

Figure 6.4(a) shows the Sn and Cu blocking curves extracted from the MEIS data. Each of the major blocking features is labelled to correspond with the schematics of bulk scattering geometry in Figure 5.2, and the theoretical position of the bulk feature is marked (vertical lines). Examination of the Sn scattering data obtained from MEIS shows no blocking features. An example Sn scattering spectrum is shown in Figure 6.4(a); neither the ⟨110⟩ or ⟨211⟩ incidence datasets showed any Sn blocking features. It is therefore possible to conclude that all Sn atoms must be in a single layer, with no penetration into the bulk of the Cu crystal. This does not allow any of the proposed models to be discounted, but does simplify the data analysis process, because only the Cu scattering data need be considered.

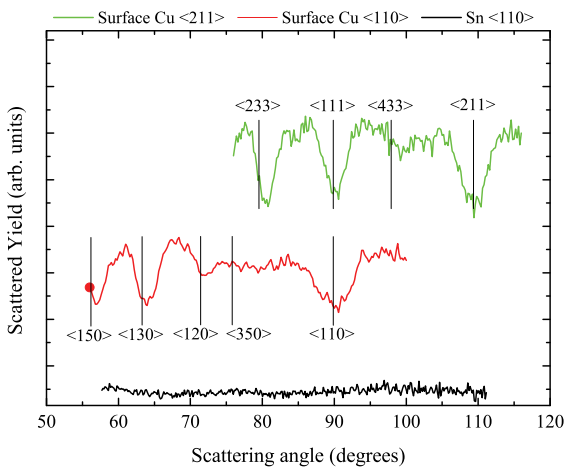

(a) MEIS data. Note that the Sn data shows no blocking features.

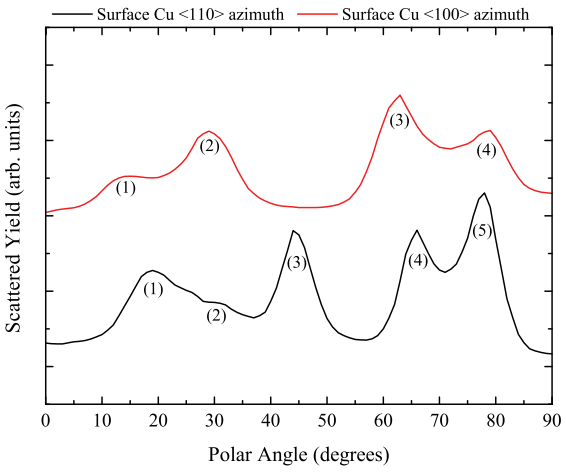

(b) CAICISS Cu backscattering data.

Figure 6.4 Processed Phase 1 scattering data. Data have been vertically translated for clarity.

Processed CAICISS data is shown in Figure 6.4(b). Features are numbered to correspond with the schematics of scattering geometry in Figure 5.3. The peaks labelled (1) in each dataset are the 'surface peaks'. They arise from focusing effects in only the outermost atomic layer, and thus their position gives information about the inter-atomic spacing in each azimuth. The remaining peaks give information on interlayer spacings and lateral displacements via changes in the peak location and relative intensities. Many of the peaks have multiple contributions, either from multiple atoms — generally occurs at higher polar angles — or from different scattering planes (e.g. the geometries labelled (2) and (2*) in Figure 5.3).

Simulations of each proposed structural model (detailed in Section 6.1) were compared to Phase 1 data. All models were constructed with Sn and Cu atoms in sites specified by the bulk lattice of Cu — all structural parameter values refer to shifts from bulk Cu lattice positions. Preliminary R-space plots were constructed for each structural parameter to allow the intervals for SOAR to be set more precisely. For a full explanation of the usage and functionality of SOAR, see Chapter 4.

The structural parameters required for fitting of Phase 1 were identified as: the first interlayer spacing change for Cu atoms (Δ_{12}), the second interlayer spacing change for Cu atoms (Δ_{23}), and the change in displacement of Sn atoms relative to the outermost Cu layer (Δ_{Sn}). In the case of the surface alloy model, the Sn shift is out of the plane of first layer Cu atoms. For the overlayer models, zero displacement is considered to be at one bulk Cu lattice distance above the first layer Cu atoms. Enhancements to surface vibrational amplitudes were not included in the first SOAR run — to reduce solve time.

6.2.1 CAICISS correction factors

The interaction potential correction factor is extremely important in CAICISS analysis. The low kinetic energy of the incident ions means that the time the ions spend near the crystal surface is much larger than with higher energy ion beam techniques such as MEIS. With the increased time of interaction comes an increase in the effect of electron screening, which must be compensated for in the Coulomb interaction by the inclusion of a multiplicative correction factor. The simple calculation of Equation 6.1 gives a rough estimate of the ratio of beam velocities for each technique. This is approximately equivalent to the ratio of time spent by ions in the near-surface region for each technique. The shorter interaction time of MEIS means that the effects of electron screening are significantly reduced and therefore no correction is required to the potentials.

$$
\begin{aligned}
E_{\text{kinetic}} &= \frac{1}{2}mv^2 \\
\therefore \quad \frac{v_{\text{M}}}{v_{\text{C}}} &= \sqrt{\frac{E_{\text{M}}}{E_{\text{C}}}\frac{m_{\text{C}}}{m_{\text{M}}}} \\
&\approx 11.5 \quad \text{for typical values}
\end{aligned}
\tag{6.1}
$$

where subscript M and C denote MEIS and CAICISS respectively,
and E, v and m are ion energy, velocity, and mass.

Typical beam values are: (MEIS) 100 keV H^+ beam, (CAICISS) 3 keV He^+ beam.

Previous studies using the Warwick CAICISS system [3,90] have shown deviation from the generally accepted values from O'Connor [24]. Chapter 13 details experiments undertaken on the Warwick CAICISS system in order to resolve this discrepancy via studies of clean metal surface structures. It is important that a suitable correction factor value is chosen for analysis in this investigation.

The correction factor was initially treated as another parameter in the fitting. Figure 6.5 shows the R-factor variation plotted against the correction factor for each of the trial structures. For all models, correction factor values fell consistently between 0.50 and 0.70. In this range the R-space gradient is shallow, so little is to be gained from including the parameter in further fitting. For all further CAICISS simulations of Cu backscattering, a correction factor of 0.58 was used — a median value consistent with all plots in Figure 6.5 and with previous studies [3, 90], and later verified during the collection of clean surface Cu data presented in Chapter 13.

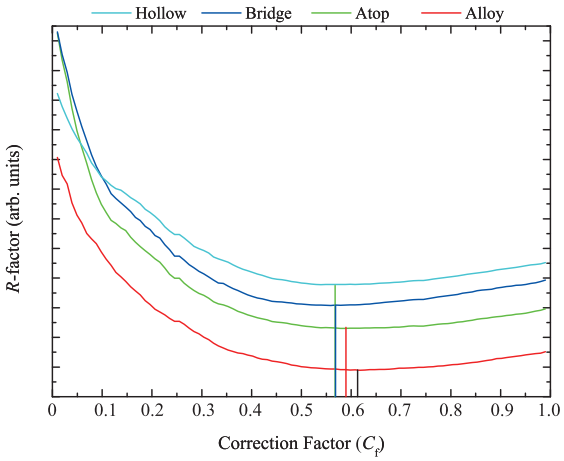

Figure 6.5 CAICISS Phase 1 R-factor variation with interaction potentials correction factor for each model

6.2.2 Initial R-factor comparisons

Figure 6.6 and Figure 6.7 show plots of the initial MEIS and CAICISS fits for each model — all structural parameters at bulk values and correction factor fixed at 0.58 for CAICISS simulations. R-factors for each model are shown in Table 6.1. The R-factors are a summation over the two datasets for each technique. The results seem to be ambiguous; the atop site and bridge site overlayer models fit MEIS data more closely; CAICISS clearly favours the alloy model and the hollow site overlayer model.

Visual examination of the fits in Figure 6.7 clearly shows that the peaks obtained for the bridge and atop overlayer models in CAICISS are inconsistent with the data — the simulations show additional peaks which are not seen in the data.† For example, the bridge site model shows additional peaks at 55° and 70° polar angle in the ⟨110⟩ azimuth. The atop site model also shows the additional peak at 55° as well as a much reduced surface peak intensity. Examination of the MEIS fits (Figure 6.6) reveals that the differences in R-factor arise mainly from variations in the relative intensities of features.

It is obvious that there are problems with comparing models by R-factor alone. The models are very similar, so R-factor variations between models are largely within error bounds

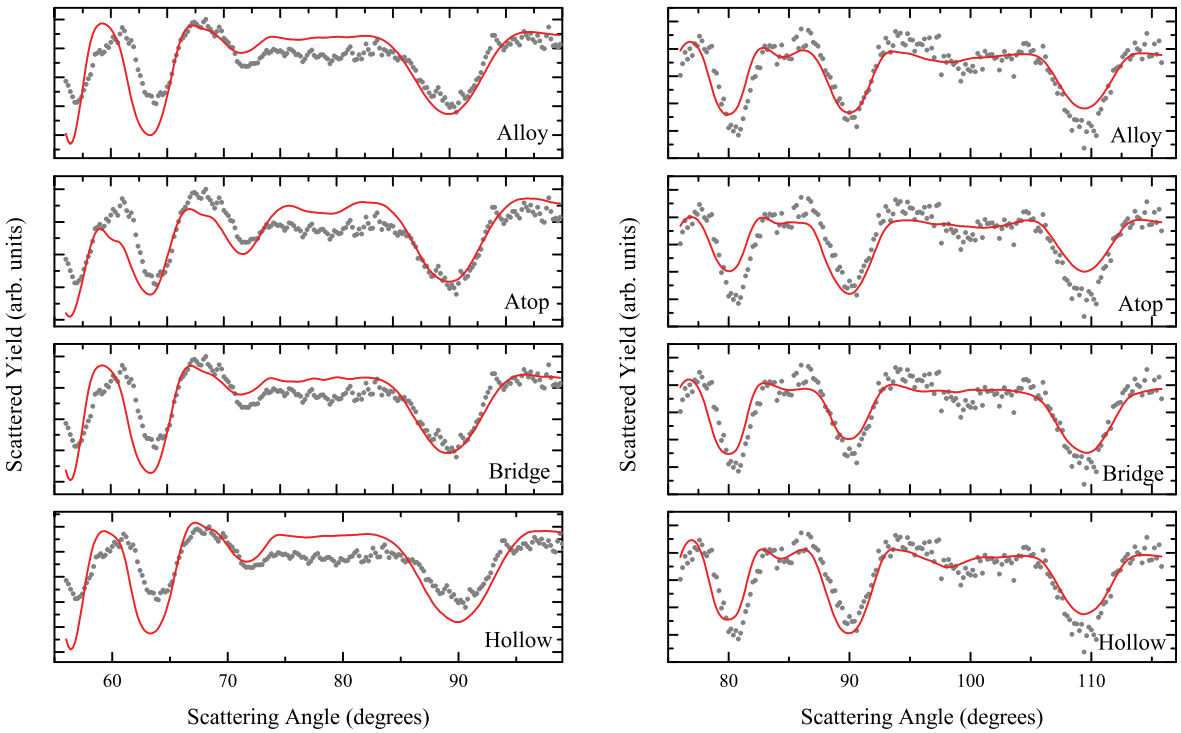

(a) ⟨110⟩ incidence (b) ⟨211⟩ incidence

Figure 6.6 MEIS fits for Phase 1 models with all atoms in bulk Cu lattice positions.

† For a detailed discussion of what features one expects to see in a CAICISS spectrum, refer to Chapter 4.

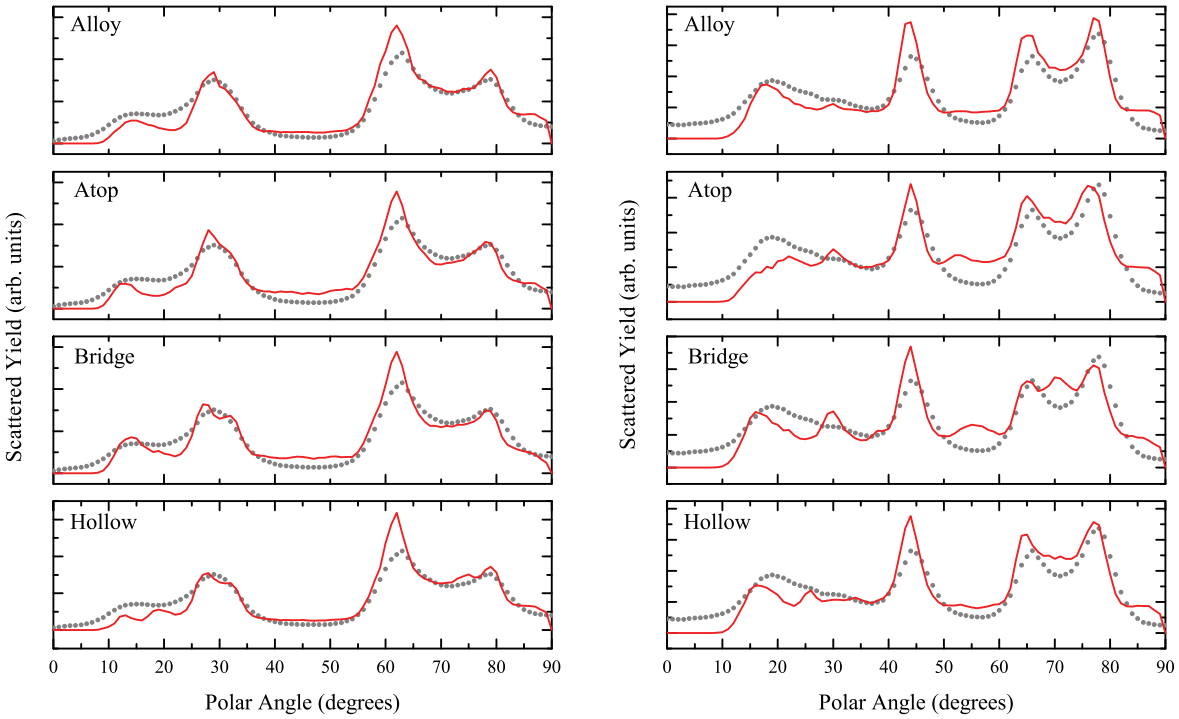

(a) ⟨100⟩ azimuth (b) ⟨110⟩ azimuth

Figure 6.7 CAICISS fits for Phase 1 models with all atoms in bulk Cu lattice positions, with a correction factor (C_f) of 0.58.

Table 6.1 Initial Cu scattering R-factors for each Phase 1 trial structure.

	R-factors	
Model	MEIS	CAICISS
Surface Alloy	11.5	4.9
Overlayer (atop sites)	5.3	7.9
Overlayer (bridge sites)	9.3	6.6
Overlayer (hollow sites)	18.1	5.5

arising from noise in the data. R-factors will still be vital when attempting to optimise each model in isolation, but for this study it is also necessary to conduct examination of fits by eye, taking into account both peak positions and relative intensities of features.‡ Any models which exhibit a large variation from the experimental data can be discarded from further analysis. In this case, the CAICISS simulations were used to discard the atop and bridge site overlayer models. Further fitting was conducted on the surface alloy and hollow site overlayer models using SOAR to resolve which model is the most likely candidate. MEIS simulations were not able to eliminate any of the models conclusively.

‡ The method of R-factor calculation for each technique is discussed in more detail in Chapter 4.

6.2.3 Surface alloy

R-space plots were compiled for each of the parameters of the surface alloy model. Table 6.2 details the parameters and the bounds chosen for SOAR. There appears to be good agreement between techniques at this stage. Minima are found at positive parameter values, which implies an expansion relative to bulk spacings should be seen in the optimised fits for all structural parameters.

SOAR optimisation gave final R-factor values of 9.7 for MEIS and 4.4 for CAICISS — approximately a 16 % improvement for MEIS and 10 % improvement for CAICISS over the bulk fit R-factors. The optimised MEIS fits are shown in Figure 6.8. Under visual examination the locations of the blocking features are good. In particular, the feature at a scattering angle of 84° in the ⟨211⟩ incidence spectrum is enhanced. The intensities and widths of features are still not well-matched. Overall, the fit does not show a vast improvement from the initial bulk simulations of the surface alloy model.

Surface vibrations

Exclusion of MEIS surface vibrational parameters may account for the inability of SOAR to find a better fit to the data. Additional vibrational fitting was conducted to test the improvement to the final R-factor. Figure 6.9 shows R-space plots for surface vibrational parameters. The four parameters included are in-plane (∥) and out-of-plane (⊥) vibrations for both the adsorbed Sn (V_{Sn}) and outermost Cu (V_{Cu}) layers. Three parameters show little or no R-factor variation in the range tested. The notable exception is the in-plane vibrations of surface Cu atoms (V_{Cu} ∥), which shows a marked increase in R-factor at values higher than bulk vibrational amplitude, and seems to show that reducing this vibration amplitude below the bulk level could lead to a better fit.

Re-running SOAR — with MEIS vibrational parameters included — produces the plots shown in Figure 6.10. Comparison with Figure 6.8 shows some improvement to the fit, particularly for ⟨110⟩ incidence. The R-factor is reduced from 9.7 to 4.0. Most of the improvement in

Table 6.2 Phase 1 surface alloy model structural parameter intervals.

		Fitting interval (Å)	
Parameter		MEIS	CAICISS
1	Sn out-of-plane shift (Δ_{Sn})	0.15 ± 0.20	0.20 ± 0.20
2	Cu first interlayer spacing (Δ_{12})	0.05 ± 0.30	0.10 ± 0.30
3	Cu second interlayer spacing (Δ_{23})	0.05 ± 0.30	0.10 ± 0.30

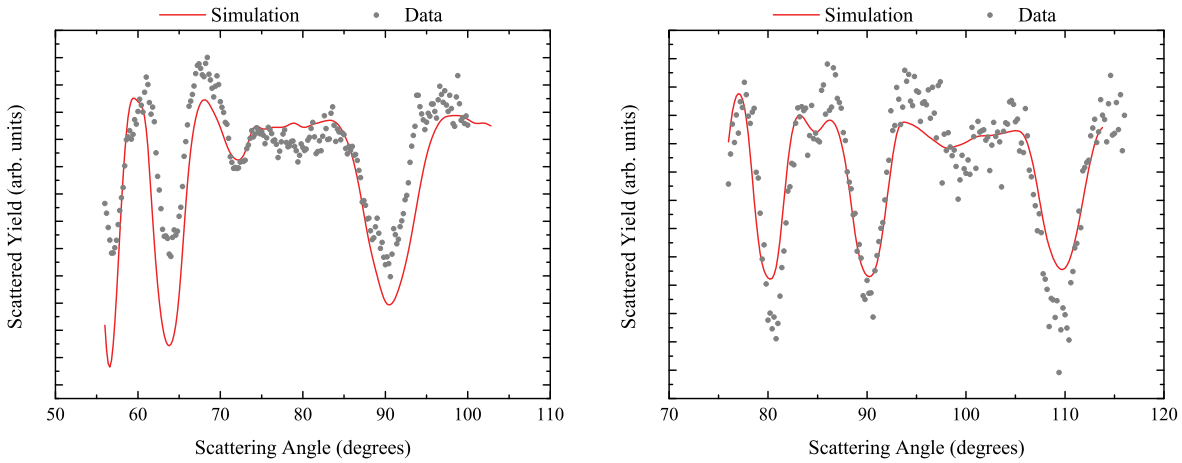

(a) ⟨110⟩ incidence (b) ⟨211⟩ incidence

Figure 6.8 Optimised MEIS Cu scattering fits from SOAR for Phase 1 surface alloy model.

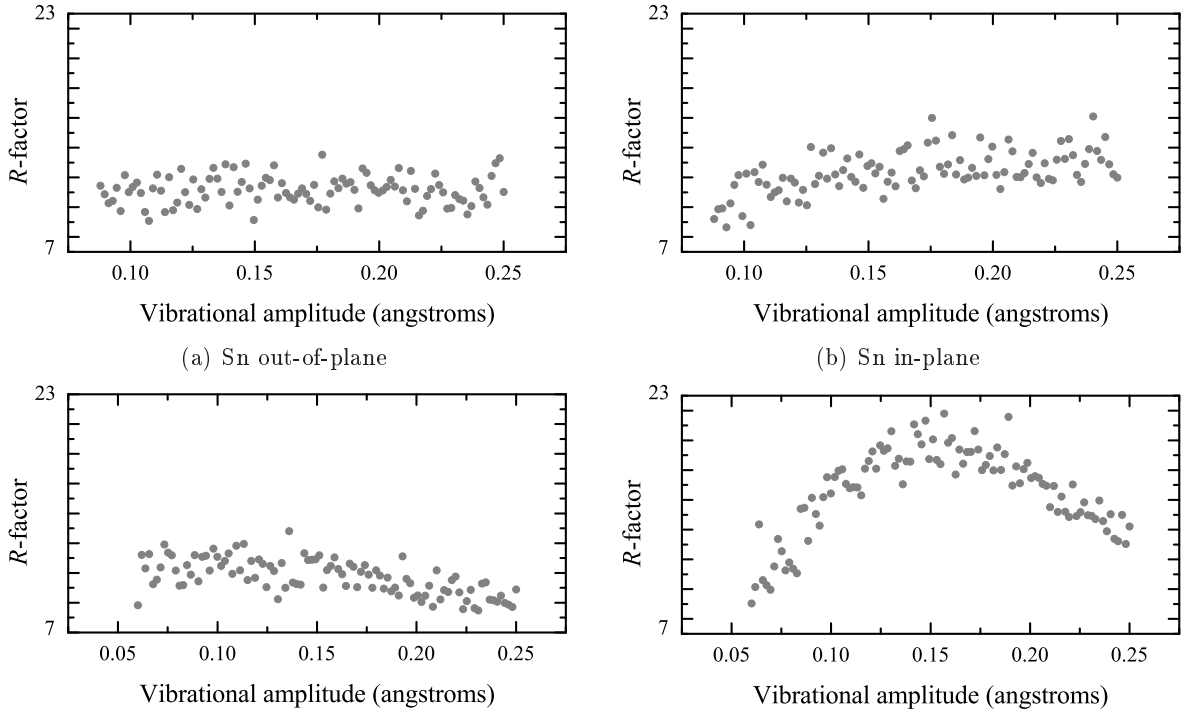

(a) Sn out-of-plane (b) Sn in-plane

(c) Cu out-of-plane (d) Cu in-plane

Figure 6.9 MEIS R-space plots for Phase 1 surface alloy model vibrational parameters.

the fit is seen in the blocking dips below 70°. This is expected, since features created from ions emerging at shallower altitudinal angle from the surface — lower scattering angle — should be more sensitive to surface layer vibrations. The ⟨211⟩ incidence simulation showed no obvious improvement. Table 6.3 shows the vibrational parameter values output by the IFFCO codes, and the bulk values for reference [76]. The surface vibrations are all much larger than the bulk values. In the case of the surface Cu atoms, vibrations are of the order of five times the

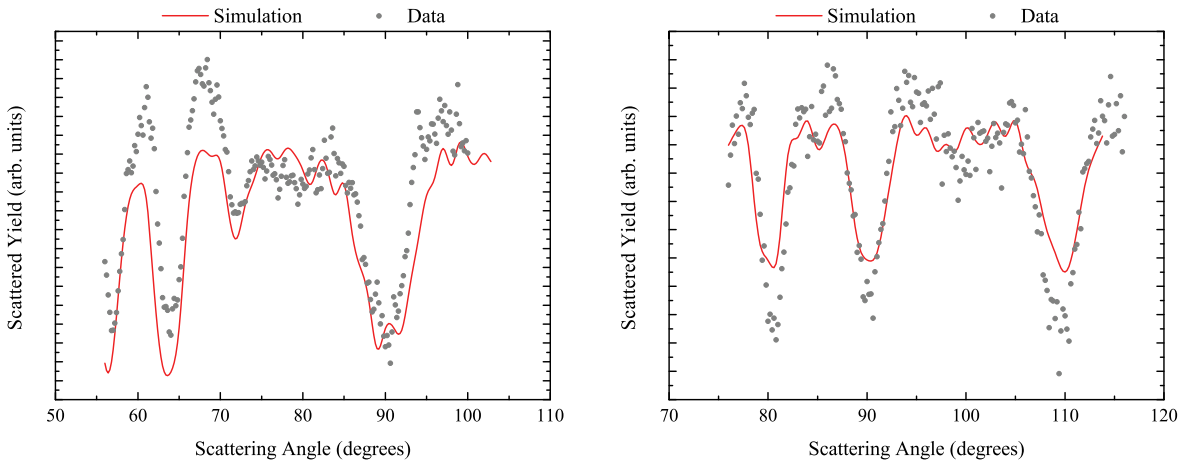

(a) ⟨110⟩ incidence (b) ⟨211⟩ incidence

Figure 6.10 Optimised MEIS Cu scattering fits from SOAR for Phase 1 surface alloy model including vibration parameters.

Table 6.3 Optimised MEIS surface vibrational amplitudes for the Phase 1 surface alloy model. (Bulk values from Slater [76])

Parameter			Vibration Amplitude (Å)
1	Sn out-of-plane vibration	($V_{\mathrm{Sn}}\perp$)	0.27 ± 0.04
2	Sn in-plane vibration	($V_{\mathrm{Sn}}\parallel$)	0.11 ± 0.08
3	Cu out-of-plane vibration	($V_{\mathrm{Cu}}\perp$)	0.34 ± 0.03
4	Cu in-plane vibration	($V_{\mathrm{Cu}}\parallel$)	0.35 ± 0.04
	Sn bulk vibration reference		0.098
	Cu bulk vibration reference		0.070

bulk value. Enhancements of this size to the dynamic vibrations of near surface layers seem unlikely. The more reasonable conclusion is that stress in the surface layer has led to a large degree of rumpling.

This result is consistent with several previous studies [91–93], which have shown that data could only be modelled successfully by using greatly enhanced vibrational amplitudes of the outermost layer atoms. Woodruff and Robinson [91] conclude that the enhancements can be at least a factor of two larger than that expected for surface vibrations of an elemental solid. Other independent MEIS investigations [93] have arrived at a similar conclusion. Woodruff's analysis centres on the limitations of the method used by the VEGAS code to simulate atomic vibrations. VEGAS incorporates a mean-square displacement parameter for this purpose, which can equally well relate to local random static displacements. The interaction time of the incident ions with the surface is much shorter than the vibrational periods of the atoms [91], so the MEIS data represent a sequence of instantaneous 'snapshots' of the atomic displacements, where no distinction can be made between static and dynamic displacements.

Strongly enhanced dynamic surface displacements as a consequence of the fact that the material is an alloy are difficult to understand, but static displacements may not be. In the case of the Cu(100)/Sn system, the presence of Sn atoms within the outermost Cu layer will necessarily induce surface stress due to the large lattice mismatch of the two elements. It is reasonable to assume that rumpling in the outermost Cu layer may result, which will manifest in simulations as enhanced out-of-plane surface vibrations. Those same stresses may also inhibit in-plane vibrational amplitudes of Cu atoms.

CAICISS results

Figure 6.11 shows the optimised fits for CAICISS. As discussed above, the R-factor is 4.4, approximately a 10 % improvement after fitting. Under examination by eye the fits are good. All backscattering features are located at or near the correct polar angles to match the data. The surface peaks at 15° and 19° are the most crucial features for examination of the surface layer. The simulation of the ⟨110⟩ azimuth surface peak shows a particularly good fit to the data.

Surface vibrational parameters were included in the CAICISS fitting but, due to limitations of the FAN simulation codes, are unable to be independently varied in the same way that MEIS simulations allow. However, the surface Debye temperature can be varied, which does provide a means of modelling vibrations. Debye temperature is inversely proportional to vibrational amplitude, so by setting a lower value, the vibrational amplitude can be increased (see Chapter 3 for further theory detail). The SOAR codes are unable to vary the Debye temperature automatically, so trying to optimise the value can be a tedious process.

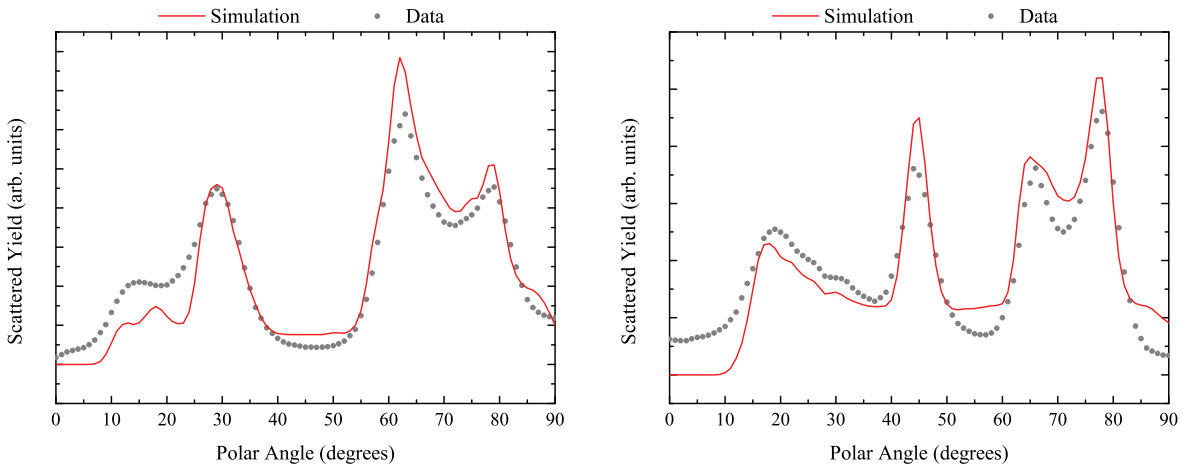

(a) ⟨100⟩ azimuth (b) ⟨110⟩ azimuth

Figure 6.11 Optimised CAICISS Cu backscattering fits for Phase 1 surface alloy model.

Bulk simulations were examined with a number of different Debye temperatures, and a suitable value was chosen which reduced the R-factors to an approximate minimum. A surface Cu Debye temperature of 340 K provided a better fit than the bulk-equivalent[§] value of 520 K. Equation 3.9 shows that this corresponds to approximately 150 % of the vibrational amplitude of bulk Cu. A surface Sn Debye temperature of 170 K was found to improve the fits, giving a vibrational amplitude approximately 160 % that of bulk Sn. The Debye temperatures were later re-examined — after SOAR fitting — to see if the values could be modified to improve the final fit further. No notable improvement could be achieved with modified values.

The final parameter values for fitting of the surface alloy model are shown in Table 6.4, along with corresponding error estimates. CAICISS errors appear to be vastly over-estimated. This is due to the rate of R-factor variation with parameter value being shallow. This posed a particular problem for CAICISS analysis during this investigation. The problem was addressed by additions to SOAR shortly afterward, leading to more realistic error estimates. Further discussion of the problem can be found below, and details of the changes made to SOAR to improve error estimates are given in Chapter 12 and Chapter 13.

All parameter values are positive — the first and second interlayer spacings are expanded, and the Sn atoms sit above the Cu atoms in the surface layer. The exact amount of expansion indicated differs between techniques. As a percentage of the bulk interlayer spacing of 1.808 Å, MEIS shows first and second interlayer spacing changes of (1.7 ± 1.6) % and (0.4 ± 1.9) % respectively. Sn atoms are indicated to lie (4.0 ± 10.1) % above the outermost layer of Cu atoms. CAICISS shows interlayer spacing expansions of (1.7 ± 1.1) % and (4.0 ± 0.5) %, and Sn atoms (0.5 ± 44.8) % above the outermost Cu layer. Comparison to previous studies [3]

Table 6.4 Optimised parameter values for Phase 1 surface alloy model. Inter-layer spacings are given as shifts from the bulk value of 1.81 Å. MEIS surface vibration parameters represent the mean square vibrational amplitude of atoms from rest positions.

			Parameter Value (Å)	
Parameter			MEIS	CAICISS
1	Sn out-of-plane shift	(Δ_{Sn})	0.10 ± 0.18	0.01 ± 0.81
2	Cu first interlayer spacing	(Δ_{12})	0.03 ± 0.03	0.03 ± 0.02
3	Cu second interlayer spacing	(Δ_{23})	0.01 ± 0.04	0.10 ± 0.01
4	Sn out-of-plane vibration	(V_{Sn} $\perp$)	0.27 ± 0.04	
5	Sn in-plane vibration	(V_{Sn} $\parallel$)	0.11 ± 0.08	
6	Cu out-of-plane vibration	(V_{Cu} $\perp$)	0.34 ± 0.03	
7	Cu in-plane vibration	(V_{Cu} $\parallel$)	0.35 ± 0.04	

§ The bulk-equivalent Debye temperature corresponds to the Cu bulk vibrational amplitude (0.070 Å)

show the interlayer spacing changes to be modified in both direction and magnitude from those of clean clean Cu(100), which are reported as ~ -4 % and ~ 1.5 % for the first and second inter-layer spacings respectively.

CAICISS error estimation

The error estimates associated with R-factor values for CAICISS seem to be completely disconnected with visual observation. As Figure 6.12 demonstrates — using the Sn out-of-plane shift as an example — variations in the parameter value (0.183 Å) of far less than the calculated error estimate (0.330 Å) produce clear changes in the spectral features. The shaded areas highlight two areas of the spectrum containing scattering features. The problem seems to arise due to the areas between features e.g. in the ⟨100⟩ azimuth the region 38° to 54°. Simulation values do not vary in these regions, the result of which is an overhead to the R-factor which the fitting routines are unable to reduce.

One possible method of reducing the overhead incurred by these invariant regions may be to split each of the datasets into multiple simulation runs. Each of the new simulations will concentrate only on areas of the data which contain features to be fitted. The alternative is to develop an entirely new R-factor measurement for CAICISS. Such large-scale changes to the simulation process will take time to implement and test, and thus are unfortunately beyond the scope of the current investigation due to time constraints.

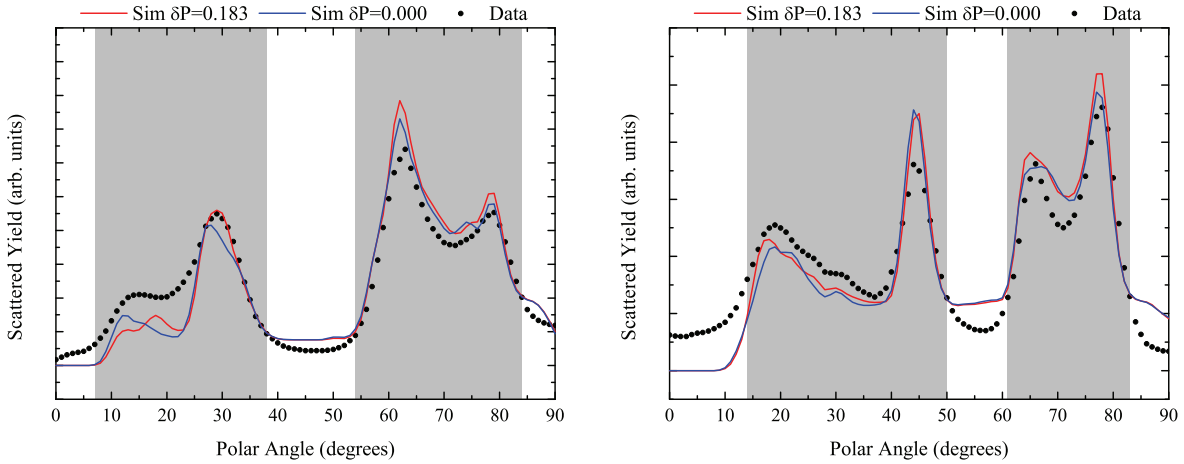

(a) ⟨100⟩ azimuth (b) ⟨110⟩ azimuth

Figure 6.12 CAICISS Cu scattering fits showing the effect of parameter variation on spectrum features. This example focuses on the Sn out-of-plane shift parameter (units of Angstrom).

6.2.4 Hollow-site overlayer

R-space plots (not shown) were compiled for the hollow site overlayer model parameters. Neither technique seems to be particularly sensitive to the out-of-plane shift of Sn atoms — the *R*-space plots showed shallow gradient. This is not entirely surprising, given the very low coverage of Sn in this phase. Table 6.5 shows the intervals for SOAR.

Table 6.5 Phase 1 hollow-site overlayer model structural parameter intervals.

		Fitting interval (Å)	
	Parameter	MEIS	CAICISS
1	Sn out-of-plane shift (Δ_{Sn})	0.30 ± 0.30	0.00 ± 0.30
2	Cu first interlayer spacing (Δ_{12})	0.05 ± 0.30	0.10 ± 0.30
3	Cu second interlayer spacing (Δ_{23})	0.05 ± 0.30	0.10 ± 0.30

Figure 6.13 and Figure 6.14 show the optimised MEIS and CAICISS fits obtained after IFFCO fitting. *R*-factors for these fits are: 8.3 (MEIS) and 5.0 (CAICISS) — initial *R*-factors were: 18.1 (MEIS) and 5.5 (CAICISS). The fit of the major MEIS blocking features is good. Surface vibrational parameters were not included in the first fitting run for this model. The CAICISS fit seems to match the positions of the majority of major backscattering features. The multiple contributions to the wide surface peak in the ⟨110⟩ azimuth dataset are not as well-matched as for the surface alloy model (Figure 6.11). Final parameter values for both techniques are shown in Table 6.6.

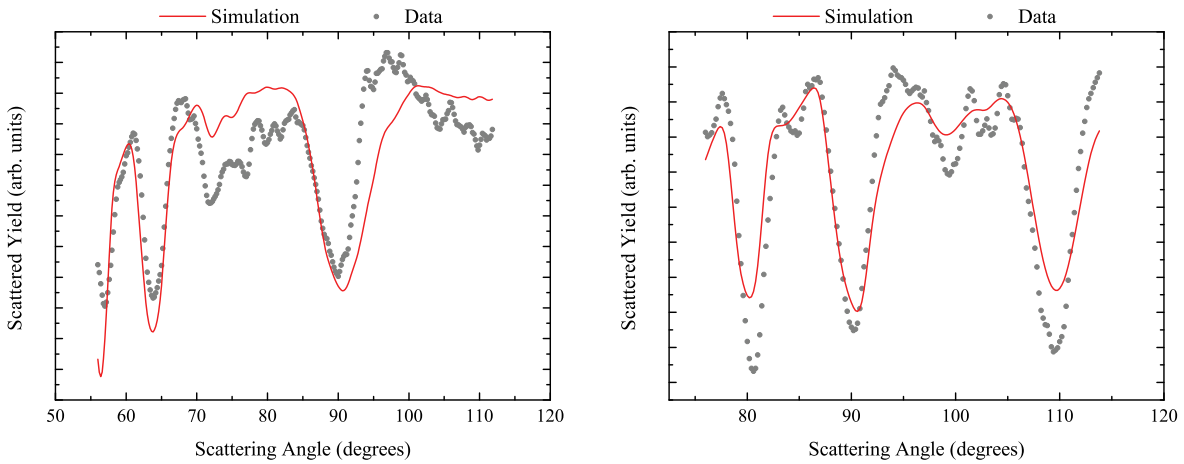

(a) ⟨110⟩ incidence (b) ⟨211⟩ incidence

Figure 6.13 Optimised MEIS Cu scattering fits for Phase 1 hollow-site overlayer model.

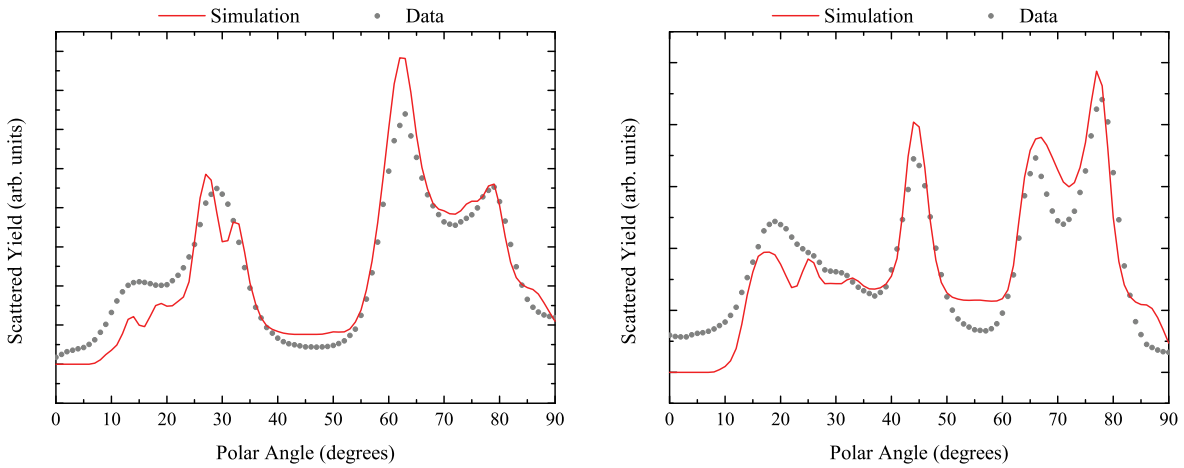

(a) ⟨100⟩ azimuth (b) ⟨110⟩ azimuth

Figure 6.14 Optimised CAICISS Cu backscattering fits from SOAR for Phase 1 hollow-site overlayer model.

Table 6.6 Optimised parameter values from SOAR for Phase 1 hollow-site overlayer model.

			Parameter Value (Å)	
Parameter			MEIS	CAICISS
1	Sn out-of-plane shift	(Δ_{Sn})	-0.33 ± 0.08	-0.20 ± 0.20
2	Cu first interlayer spacing	(Δ_{12})	0.01 ± 0.04	0.03 ± 0.02
3	Cu second interlayer spacing	(Δ_{23})	0.03 ± 0.04	0.09 ± 0.02
4	Sn out-of-plane vibration	(V_{Sn} $\perp$)	0.06 ± 0.02	
5	Sn in-plane vibration	(V_{Sn} $\parallel$)	0.27 ± 0.04	
6	Cu out-of-plane vibration	(V_{Cu} $\perp$)	0.08 ± 0.03	
7	Cu in-plane vibration	(V_{Cu} $\parallel$)	0.03 ± 0.04	
	Sn bulk vibration reference		0.098	
	Cu bulk vibration reference		0.070	

Surface vibrations

Inclusion of MEIS surface vibrational parameters showed improvement to the fit for the surface alloy model, so the same parameters were applied to the hollow site overlayer model. *R*-space plots for the vibrational parameters (Figure 6.15) show similar trends to the alloy model. CAICISS analysis was conducted using the Debye temperatures obtained from analysis of the alloy model (340 K for surface Cu and 170 K for surface Sn). The MEIS fits with vibrational parameters included are shown in Figure 6.16.

Allowing vibrational parameters to drop below bulk values has created some interesting effects in the simulation due to narrowing of blocking features — ions are able to escape from deeper in the crystal because of the lack of movement in the surface layer. Although the fit appears to be better according to the *R*-factor analysis, the vibrational parameter values

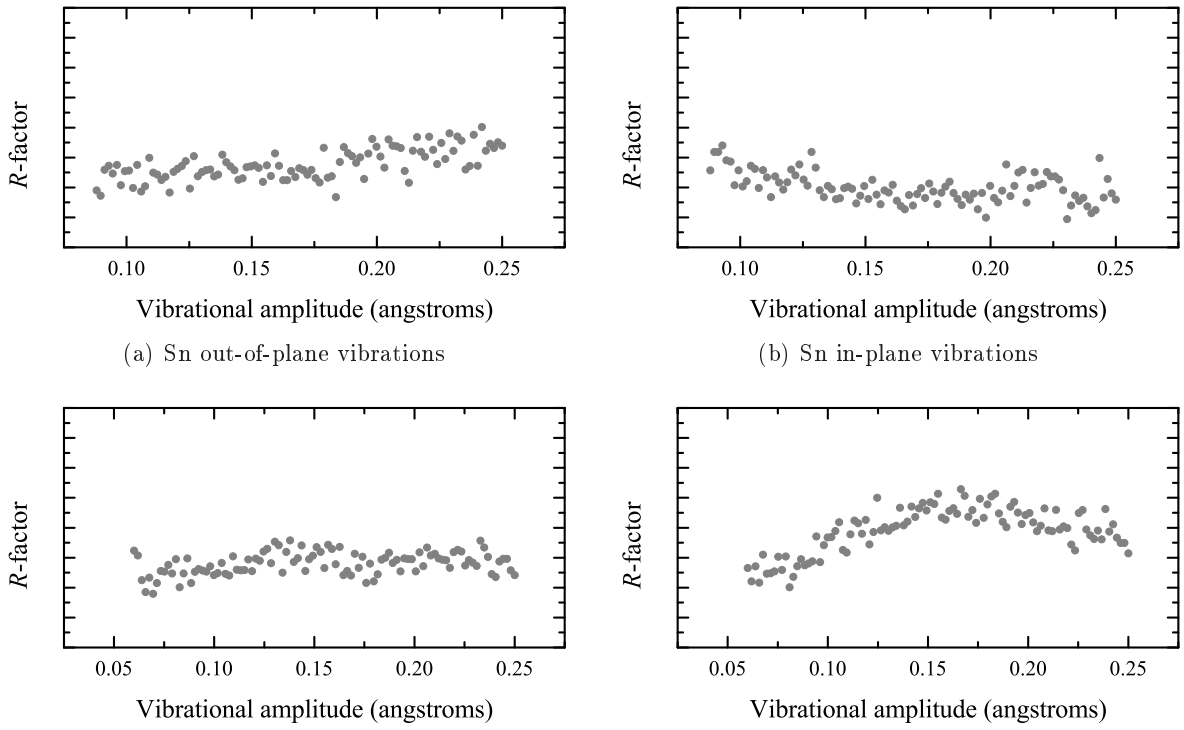

(a) Sn out-of-plane vibrations

(b) Sn in-plane vibrations

(c) Cu out-of-plane vibrations

(d) Cu in-plane vibrations

Figure 6.15 MEIS *R*-space plots for Phase 1 hollow-site overlayer model surface vibrational parameters. Parameter assignments are described in the text.

returned are highly unlikely, and conflict with the results of CAICISS analysis. This highlights the importance of carefully choosing sensible bounds for SOAR. The vibrational parameter values obtained are given in Table 6.6 for reference.

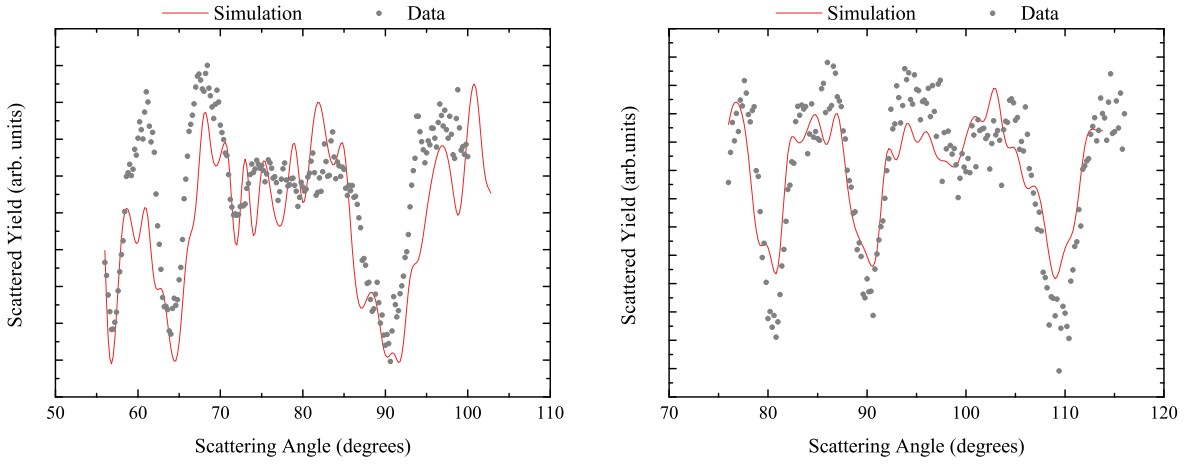

(a) meis vib 110

(b) meis vib 211

Figure 6.16 Optimised MEIS Cu scattering fits from SOAR for the Phase 1 hollow-site overlayer model including vibration parameters.

6.3 CAICISS Sn backscattering

Analysis of the backscattered Cu signal is all that can be hoped for from MEIS data, since Sn atoms have been shown to form a single layer. CAICISS datasets have the advantage that they provide a surface backscattering peak at grazing incidence from each species of atom. This is information not easily obtained from a typical MEIS setup, but CAICISS is ideally suited. Examination of the CAICISS Sn backscattering data will provide additional information about the nature of Sn atom adsorption sites, which may indicate whether Phase 1 is more likely an alloy or an overlayer structure. This is information directly from the Sn atoms, in contrast to the analysis so far, which has relied on inferring Sn atom positions based on changes in the scattered Cu data.

Figure 6.17 shows the recorded data, along with the simulated Sn spectra for each of the Phase 1 models. In this case, it appears that the data collected are not of sufficient quality to show a difference between these two similar models. The large number of counts and very wide peak in the experimental data is indicative of a problem with the CAICISS apparatus.

Obviously there are challenges in obtaining a good signal from adsorbates with low surface coverage; there are a relatively small number of scattering targets so the signal to noise ratio is poor. Surface peaks are even more challenging, due to: the small sample surface area exposed at grazing incidence, the finite size of the beam spot, and spurious signals received from the side of the sample.

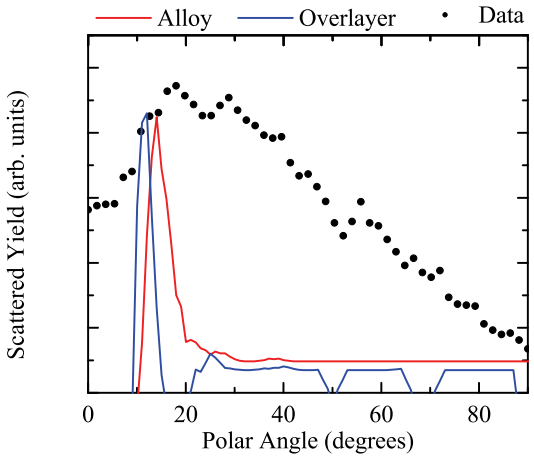

Figure 6.17 CAICISS Sn backscattering spectrum from Phase 1, showing simulated positions of Sn surface peaks.

6.4 Conclusions

Analysis of raw data for Phase 1 led to the exclusion of two models, leaving just two possibilities for further structural fitting — a surface alloy and a hollow site overlayer. Table 6.7 shows a comparison of the optimised R-factors for each technique and model. The surface alloy model produces a better fit with both techniques. Surface vibrational analysis helped to lower the R-factor in the case of the alloy model, but failed to produce any physically sensible results for the overlayer model. Vibrational fitting results from CAICISS were only approximations, but were more consistent; vibrational amplitude enhancements — over bulk values — of between 30 % and 60 % were seen for both models. Analysis of the CAICISS backscattered Sn signal failed to yield any further insight, due to poor signal quality. The conclusion of this investigation — despite some large error margins in parameter values — is that the surface alloy structure is the more likely candidate for the Phase 1 structure.

Table 6.7 Optimised R-factors from SOAR for Phase 1 trial structures.

R-factors	MEIS	CAICISS
Surface Alloy	4.0	4.4
Overlayer (hollow sites)	8.3	5.0

CHAPTER 7

Cu(100)/Sn: Phase 2

Phase 2 was originally identified by Argile and Rhead [77], who observed a LEED pattern based on a $p(2\times6)$ superstructure.They suggested that the periodicity can be satisfied by chains of Sn atoms on the surface. The model they proposed is a 0.42 ML overlayer consisting of chains of Sn atoms where six atomic diameters of Cu are covered by five Sn atoms (see Figure 7.1).

McLoughlin et al. continued the investigation of Phase 2 [78], noting that the LEED spots in the $c(2\times2)$ positions are significantly brighter over a wide energy range than the others of the superlattice. This led the authors to suggest that Phase 2 originates from a $c(2\times2)$ superstructure, with the additional spots observed arising from surface layer stress relief. A number of different structural models were presented, with coverages in the range 0.33 ML to 0.42 ML. While the Argile and Rhead model is consistent with the LEED periodicity observations of McLoughlin, it would not necessarily be expected to produce $c(2\times2)$ diffraction spots with considerably higher intensity than other superlattice beams as observed experimentally. The new models proposed (see Figure 7.2) are based on surface alloys and overlayers with various mixings of $c(2\times2)$ and $p(2\times2)$ structures — they were unable to distinguish between overlayer and alloy models using the LEED I-V technique.

A study by Nara et al. [82] contained the first STM images of Phase 2. By assuming that the protrusions seen in the STM image are Sn atoms, the authors proposed yet another model consistent with the STM images which incorporates formation of Sn dimers (see Figure 7.3). The STM study by Nara also made the first attempt to identify whether Phase 2 is an overlayer or surface alloy structure. By comparing the height of Sn atoms in STM images between Phase 1 and Phase 2 the authors concluded that they must possess the same surface type. The authors then conclude that Phase 2 must be a surface alloy based on the rather speculative premise that Phase 1 is a surface alloy. However, as demonstrated in the previous chapter, this is in fact believed to the case after examination with ion scattering techniques.

Still further structural models were proposed by Lallo et al. [81] during a re-investigation of the Cu(100)/Sn system using spot-profile analysis LEED (SPALEED). Their suggestion that inclusion of a glide plane in Phase 2 models should be mandatory led them to conclude that all

models previously proposed should be discounted because of incorrect symmetries. Instead, they suggested three new possible Sn unit cell models based on a $p(2\times6)$ superstructure which incorporated glide planes (see Figure 7.4), but were unable to ascertain the most likely structure using the techniques available to them.

In this chapter, a total of thirteen structural models are compared with data collected from MEIS and CAICISS. MEIS data are examined first in an effort to exclude some of the possibilities. Then analysis of CAICISS data is presented in order to resolve the most likely structure for this phase.

7.1 Structural models

This section will describe each of the models to be tested, highlighting the important structural parameters for each, and drawing parallels between models where possible.

Figure 7.1 shows the Argile and Rhead overlayer model for Phase 2 of the Cu(100)/Sn system. The important parameters for this structure are the inter-layer spacing changes. The lateral positions of Sn atoms on the surface will not be shifted during analysis of this model in order to maintain the chain structure proposed by the authors; likewise for the models suggested by McLoughlin et al. shown in Figure 7.2. Both overlayer and alloy models are proposed by McLoughlin, with two different levels of Sn coverage (0.28 ML and 0.31 ML). With no solid evidence presented by McLoughlin about which adsorption sites are believed to be occupied in the overlayer models, it was decided that all three of atop, bridge and hollow

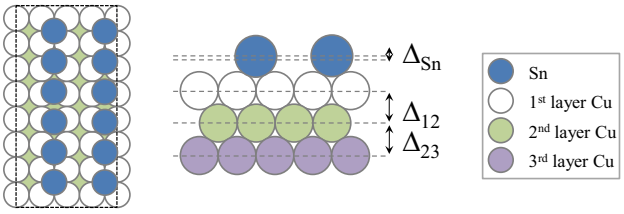

Figure 7.1 Schematic of the structure proposed by Argile and Rhead for Phase 2 [77]. Δ_{Sn} is defined as the displacement of Sn atoms from a bulk Cu lattice position.

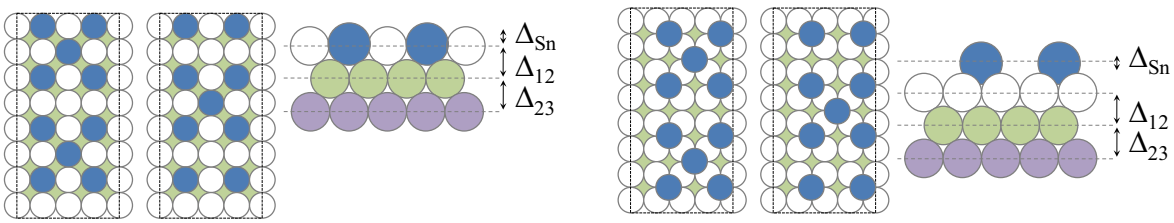

(a) Surface alloy model (b) Hollow-site overlayer model

Figure 7.2 Schematic of the trial structures proposed by McLoughlin et al. for Phase 2 [78].

sites would be tested in order to ascertain which provides the best fit. In all, this means there are eight models resulting from the McLoughlin study.

Some of the more complex models proposed by Nara et al. (Figure 7.3) and Lallo et al. (Figure 7.4) contain glide planes, which introduces additional lateral shift parameters. The Nara model is comparable with the McLoughlin models, with the addition of a glide plane in the unit cell, and formation of Sn dimers.

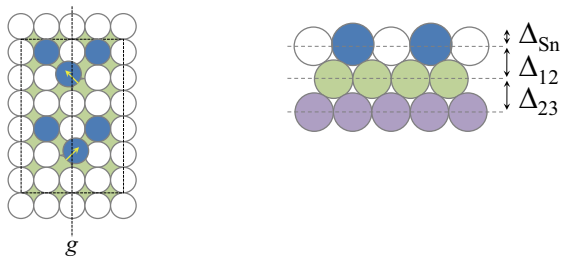

Figure 7.3 Schematic of the trial structure proposed by Nara et al. for Phase 2, showing glide plane locations (g) and lateral displacements (arrows).

The Lallo models provide both overlayer and surface alloy variants. The first model is an overlayer with all Sn atoms in bridge adsorption sites. The second model has the same bridge adsorption sites, but the top layer is now alloyed. The authors suggest that the density of the alloyed Cu atoms in the surface layer must be limited because of large Sn atom displacements from fourfold hollow sites. The third model contains an alloyed layer of Sn atoms with only

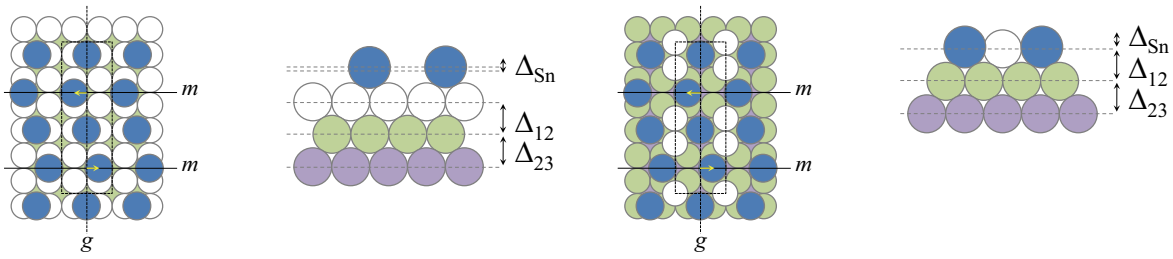

(a) Lallo overlayer with Sn atoms in bridge sites (Lallo:1)

(b) Lallo low density alloy with Sn atoms in bridge sites (Lallo:2)

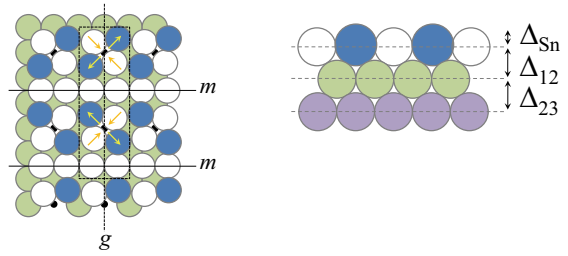

(c) Lallo high density alloy (Lallo:3)

Figure 7.4 Schematic of the three trial structures proposed by Lallo et al. for Phase 2, showing glide plane locations (g), mirror planes (m) and lateral displacements (arrows).

small displacements from fourfold hollow sites. Therefore, the surface is able to support more alloyed Cu atoms. The authors note that this solution seems to be unfavourable without a means for surface stress relief. They propose that stress is relieved through the introduction of regular vacancies within the second layer. This introduces a large number of lateral shifts and rumpling in the outermost layer. All three Lallo models are considered to be possible solutions, and will be referred to as Lallo:1, Lallo:2 and Lallo:3 in the order in which they appear in Figure 7.4.

7.2 Results

The Cu(100) surface was cleaned with IBA cycles, and Sn deposited for 27 minutes in order to obtain the Phase 2 structure. An example of the LEED pattern observed at 59 eV is shown in Figure 7.5. A schematic of the pattern observed over a larger energy range is also shown. Using the calibrated deposition rate of 0.012 MLmin^{-1} (calculated in Section 5.1), the coverage is estimated to be approximately 0.32 ML after 27 minutes of Sn exposure. The LEED pattern and Sn coverage are both in excellent agreement with previous studies [77,78] and AES showed no surface contamination.

7.2.1 MEIS

Figure 7.6 shows the processed MEIS data for Phase 2. There are no blocking features in the Sn data for either dataset, indicating that there is no sub-surface penetration of Sn atoms — a result consistent with all the models proposed to date. Both Cu datasets have the major blocking features labelled to correspond with major crystallographic directions identified in Section 5.1.1.

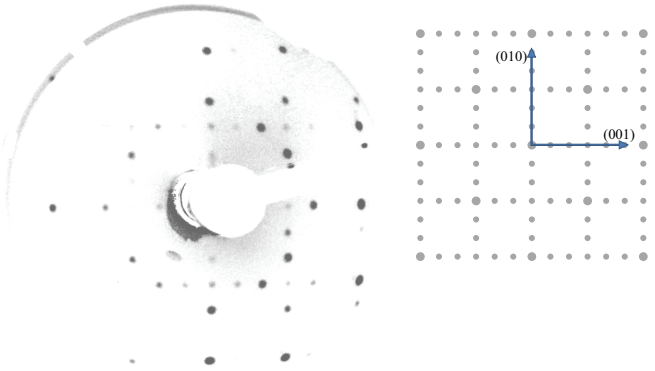

Figure 7.5 Illustration of the LEED pattern obtained for Phase 2 at 59 eV. The calibrated deposition rate of 0.012 MLmin^{-1} gives an approximate coverage of 0.32 ML after 27 minutes of Sn exposure. A photograph and a sketch are shown; the sketch is reproduced from the work of Argile and Rhead [77].

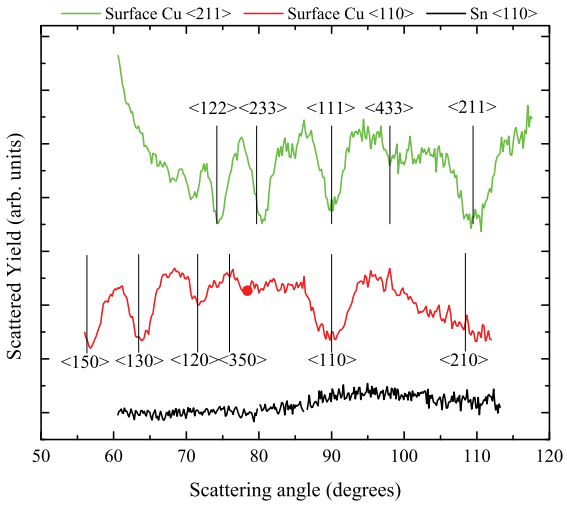

Figure 7.6 Processed Phase 2 MEIS data. Data have been vertically translated for clarity. Note that the Sn data shows no blocking features.

MEIS structural optimisation was begun by constructing each of the proposed models as a bulk-terminated Cu crystal with any additional surface Sn and Cu atoms placed in sites corresponding to an extension of the bulk Cu lattice. Table 7.1 shows the initial R-factors obtained by simulating with the bulk-terminated structures. Examination of the bulk-terminated fits (see Figure 7.7) allows some of the proposed models to be discounted immediately because of large differences between experiment and simulation spectra.

There is little, if anything, to choose between the high and low coverage variants of each of the McLoughlin models. Figure 7.7 clearly shows that any variation between the high and low coverage models is within error limits imposed by noise in the MEIS experimental data.

Table 7.1 Initial MEIS Cu scattering R-factors for each Phase 2 trial structure. The arrows indicate which structures have been retained for further analysis.

Model	MEIS R-factor		Ref.
Argile and Rhead	3.51	$\Longleftarrow$	[77]
McLoughlin: Alloy (H)	3.21		[78]
McLoughlin: Atop site overlayer (H)	3.09		
McLoughlin: Bridge site overlayer (H)	3.33		
McLoughlin: Hollow site overlayer (H)	6.22		
McLoughlin: Alloy (L)	3.24	$\Longleftarrow$	
McLoughlin: Atop site overlayer (L)	2.75	$\Longleftarrow$	
McLoughlin: Bridge site overlayer (L)	3.08		
McLoughlin: Hollow site overlayer (L)	5.54		
Lallo: Overlayer (Lallo:1)	2.35	$\Longleftarrow$	[81]
Lallo: Low density alloy (Lallo:2)	4.49		
Lallo: High density alloy (Lallo:3)	2.85	$\Longleftarrow$	
Nara	3.52	$\Longleftarrow$	[82]

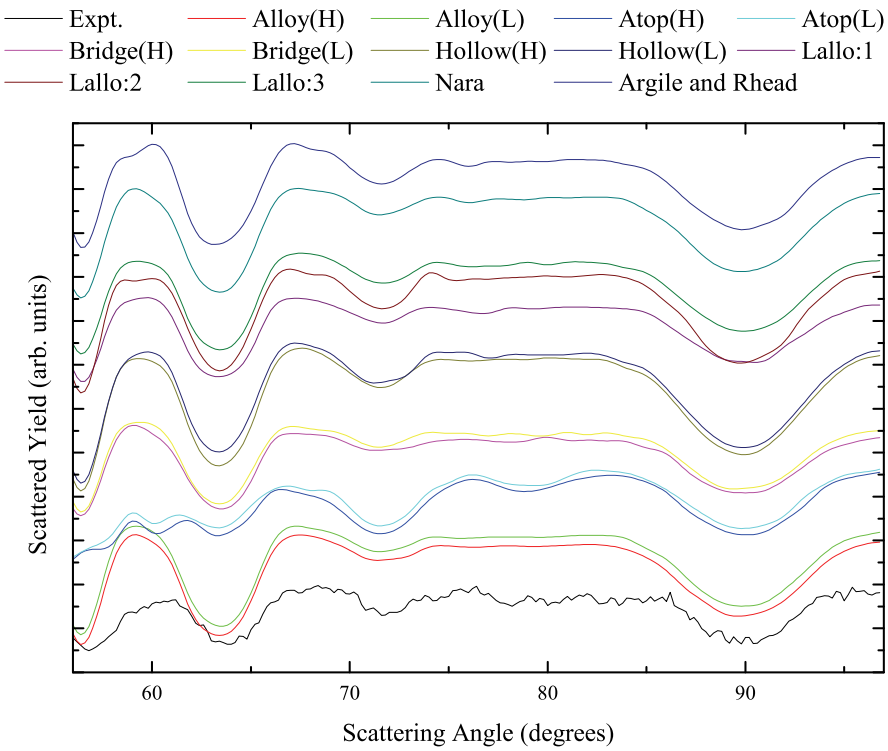

(a) ⟨110⟩ incidence

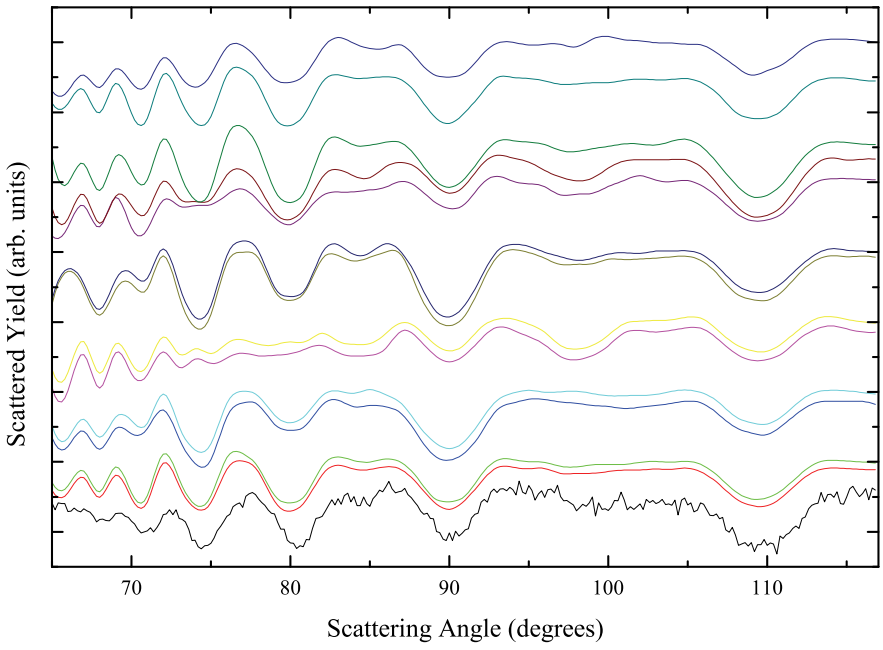

(b) ⟨211⟩ incidence

Figure 7.7 Bulk MEIS Cu scattering fits for Phase 2 models. Data were collected from two incident ion beam directions. The directions chosen provide surface specificity so that the surface structure can be probed.

Nothing is to be gained from simulating both the high and low coverage models, because the adsorption sites are the same in both cases. The low coverage variants return slightly lower R-factors in 3 out of 4 cases, so the high coverage models will be discounted. The hollow site model has a significantly higher R-factor for both coverages, so will be discounted. Excluded also is the bridge model, which shows some obvious differences in relative peak intensity to the experimental data. The alloy and atop models seems to be the best fit of the McLoughlin models, and will be retained for further investigation.

The second model of Lallo et al. (the surface alloy with limited Cu density) is discounted on the grounds that it returns a noticeably higher R-factor than the other two models suggested by these authors, which both show a similar R-factor. The first and third models will be retained. The Nara and Argile models have high R-factors, but the good fits to the experimental data in the $\langle 211 \rangle$ incident direction is worthy of further analysis.

It appears that low scattering angles are causing problems for most models. The fitting of the near surface region will necessarily target this area because the features arising in the region originate in the outermost layers of the crystal. Structural optimisation will be conducted on the six remaining models (identified in Table 7.1 by arrows) to reduce R-factors further.

The structural parameters for each model have already been identified above. All parameters are defined as shifts from bulk-terminated starting positions. R-space plots were conducted for each model in order to ascertain the best interval to use for input into the SOAR codes — a procedure discussed in more detail in previous chapters and thus not included here because of the large number of models.

Final optimised MEIS spectra for five of the six models are shown in Figure 7.8. Corresponding R-factors are give in Table 7.2. The Argile and Rhead overlayer model has been excluded because of the significantly higher R-factor than that seen in the other models. Visual inspection of spectra and the R-factor analysis seem not to agree entirely. The fits are dominated by low scattering angle discrepancies, which raise each of the R-factors, making it

Table 7.2 Optimised MEIS R-factors from SOAR for selected Phase 2 trial structures.

Model	MEIS R-factor
Argile and Rhead overlayer	2.51
McLoughlin: Alloy (L)	1.03
McLoughlin: Atop site overlayer (L)	1.25
Lallo: Overlayer (Lallo:1)	1.69
Lallo: High density alloy (Lallo:3)	1.02
Nara	1.13

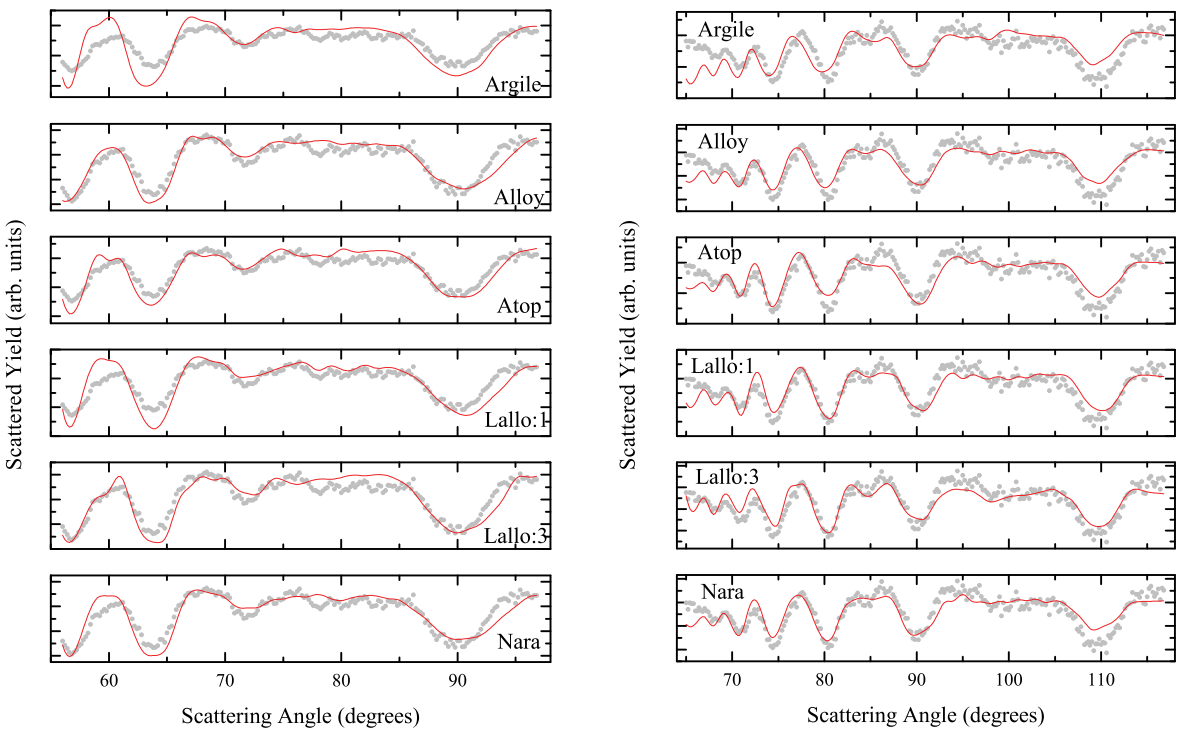

(a) ⟨110⟩ incidence (b) ⟨211⟩ incidence

Figure 7.8 Optimised MEIS Cu scattering fits from SOAR for Phase 2.

hard to distinguish exactly how well the rest of the spectrum matches. This is an unavoidable problem with current analysis methods. The Lallo overlayer model (Lallo:1) looks best in the ⟨110⟩ dataset for reproducing the fine features between 70° and 90°, but suffers from high R-factor because the larger features are not well fitted. In the ⟨211⟩ datasets, there appears to be much less variation between models. According to the combined R-factor analysis of both incident directions, the Lallo high-density alloy model (Lallo:3) is the best candidate (1.02), closely followed by the McLoughlin Alloy (1.03), then the Nara model (1.13).

MEIS analysis alone is unable to conclude which one of the five models is best, but if the R-factor analysis is to be believed, the two remaining overlayer models can be discounted, which leaves only surface alloy structures as possible solutions. Further details of the MEIS structural parameters output from SOAR for each model are given at the end of this chapter after CAICISS data have been examined.

7.2.2 CAICISS

CAICISS data collected on Phase 2 were tested against the same models as MEIS (excluding the Argile overlayer) in the hope of producing a more certain solution. A fixed value of 0.58 was

used for the screening length correction factor.* The same parameters were used for structural fitting so that direct comparison can be made between the final fits of both experimental techniques.

Simulations were examined for a number of different surface Debye temperatures, and a suitable value was chosen which reduced the R-factors to an approximate minimum. A surface Cu Debye temperature of 280 K provided a better fit than the bulk-equivalent value of 520 K. Equation 3.9 shows that this corresponds to approximately 190 % of the vibrational amplitude of bulk Cu. A surface Sn Debye temperature of 170 K was found to improve the fits, giving a vibrational amplitude approximately 160 % that of bulk Sn. The Debye temperatures were later re-examined — after SOAR fitting — to see if the values could be modified to improve the final fit further. No notable improvement could be achieved with modified values.

Figure 7.9 shows the optimised fits for each of the five models in both azimuths. Table 7.3 contains the final R-factors after CAICISS fitting. The final R-factors show that the McLoughlin overlayer ('atop') model can be discounted. Visual examination of the spectra confirms that in the ⟨100⟩ azimuth the backscattering feature at 30° is not well reproduced, and in the ⟨110⟩ azimuth the surface peak is the worst fit of the remaining models. All other models have

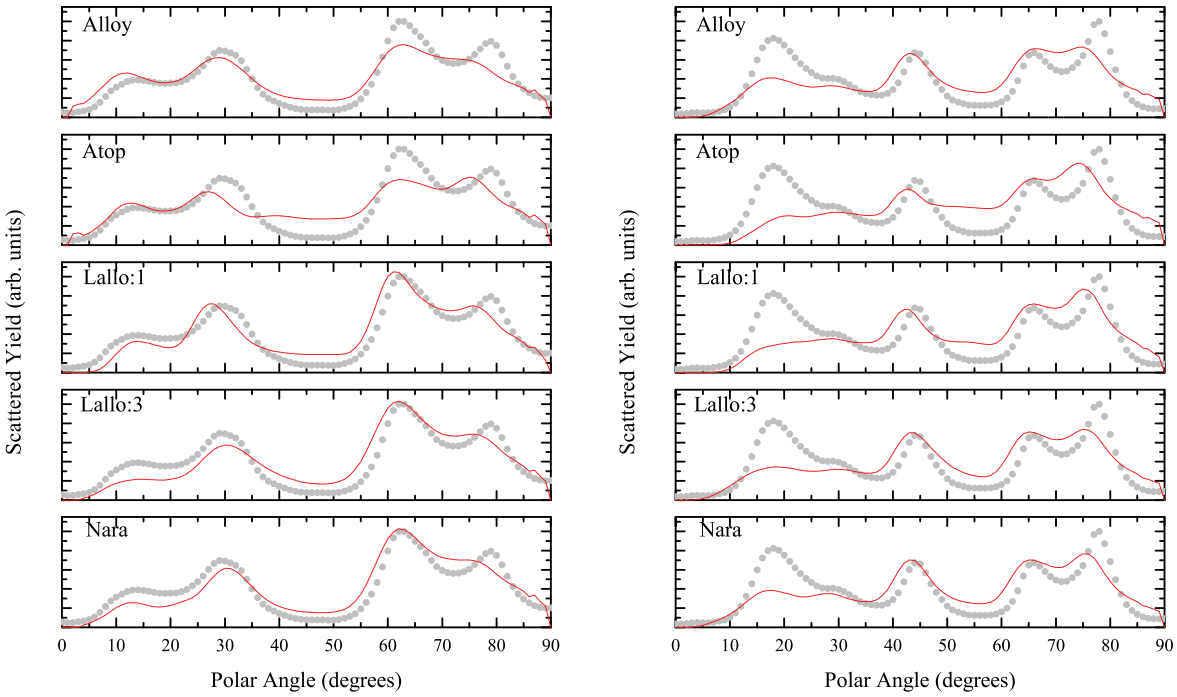

(a) ⟨100⟩ azimuth (b) ⟨110⟩ azimuth

Figure 7.9 Optimised CAICISS Cu backscattering fits for Phase 2. Experimental data are shown as scatter points, and FAN simulations as solid lines.

* Values for CAICISS correction factors have been determined both in previous studies [3], and in a new study presented in a later chapter.

Table 7.3 Optimised CAICISS R-factors from SOAR for selected Phase 2 trial structures.

Model	CAICISS R-factor
McLoughlin: Alloy (L)	5.33
McLoughlin: Atop site overlayer (L)	10.08
Lallo: Overlayer (Lallo:1)	6.68
Lallo: High density alloy (Lallo:3)	6.20
Nara	4.98

similar quality of fit. The Nara model appears to be the best fit, being the only model with an R-factor below 5.0. Further details of the CAICISS structural parameters output from SOAR for each model are given at the end of this chapter.

Visual examination of the optimised spectra provides a different conclusion. As already seen in previous analyses, the R-factor suffers from changes in beam intensity altering relative peak heights. CAICISS data is collected over a period of hours in discrete angular steps, magnifying the effect of beam inconsistencies, so peak heights are not a totally reliable comparator between models. Every effort is made during data collection to ensure a constant beam current, but the changing geometry of the crystal relative to the beam makes it hard to ensure that the same beam dose is incident on the crystal throughout each step of an entire scan.

With intensity problems in mind, it is worth examining spectra by eye also to make sure that feature positions line up. In a good model, the fitting routine will be able to line up the feature positions, but may be unable to match intensities. In a bad model, the constraints placed on the fitting parameters should prevent the fitting routine from finding a solution which matches the feature positions. Obviously this is far more subjective than the measure provided by an R-factor, but until a more suitable R-factor can be determined for CAICISS analysis applying the MEIS R-factor is the best solution, despite these pitfalls.

The McLoughlin overlayer model (labelled 'atop' in figures) is an example of a bad model, with neither of the surface-specific peaks lining up correctly with the data collected in the $\langle 100 \rangle$ azimuth. The Lallo overlayer model (Lallo:1) shows the same problem, but this is slightly masked by the fact that the intensities are matched so much better in this simulation. The difference in the models is very noticeable in the 45° peak of the $\langle 110 \rangle$ azimuth data. The Alloy, Nara and remaining Lallo alloy model are a much closer angular match than the two discounted models.

CAICISS analysis of the backscattered Cu signal is unable to conclude which one of the five models is best. The most useful conclusion that can be drawn from the CAICISS analysis so far is that the best three models are all surface alloy structures.

7.2.3 CAICISS Sn backscattering

Examination of the Sn surface peak in the CAICISS backscattering data can give vital additional information about the nature of Sn adsorption sites. Figure 7.10 shows the backscattered Sn signal extracted from data, and the simulation output for each of the remaining candidate alloy models: Lallo (Lallo:3), Nara, and McLoughlin (Alloy).

The Lallo alloy model is the only model that fits the Sn surface peak data. Not only does it display a Sn surface peak at the correct angle, but it reproduces the intensity of scattering across a wide range of polar angles. The additional information available from CAICISS leads to a definite conclusion... the Lallo [high Cu density] alloy model is the best model for Phase 2.

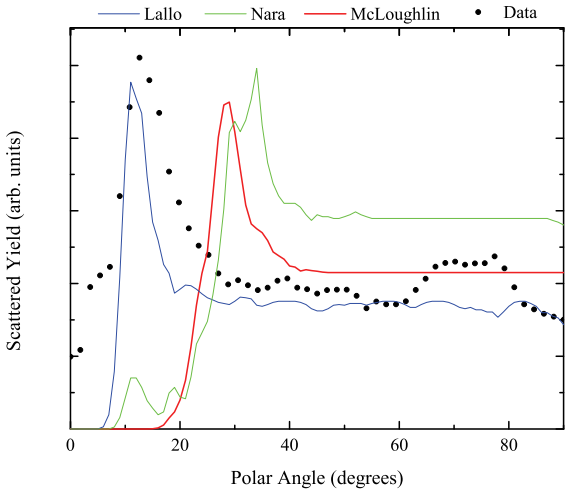

Figure 7.10 Comparison of Phase 2 Sn CAICISS backscattered experimental spectrum with computer simulations from proposed models.

7.3 Conclusions

MEIS analysis was unable to determine which single model provides the best fit. Three of the models (Alloy, Nara and the Lallo alloy) provide very similar final R-factors, with the remaining three (Argile and Rhead overlayer, McLoughlin overlayer, Lallo overlayer) being discounted. CAICISS R-factor analysis leads to the same three models being selected as the best candidates, but with equally little to choose between them. All three of the best models are based on a surface alloy, giving clear evidence that Phase 2 is surface alloy structure rather than an overlayer.

So far, only the final R-factors have been examined for each model. In the hope of distinguishing further between the models, the parameter output values themselves need to be examined. If some of the models are providing unrealistic values for structural parameters, then that may be enough to discount more models. Table 7.4 contains all of the parameter values obtained for each model (along with approximate experimental errors). Values for MEIS and CAICISS are given in separate columns.

The parameter assignments are derived from the original model specification by McLoughlin [78], Nara [82] and Lallo [81], and all parameters are given as a displacement from the bulk-terminated starting positions detailed in Section 7.1. The McLoughlin alloy model has three parameters — first and second inter-layer spacing changes and an additional Sn relaxation parameter (Δ parameters) to allow the atoms to move relative to the outermost Cu layer. The Nara alloy model has five parameters — first and second inter-layer spacing changes and accompanying Sn relaxation, and two orthogonal lateral displacement parameters (Γ_1, Γ_2[†]) which position Sn atoms on the surface to form the 'dimers' proposed by the model. The Lallo alloy model has seven parameters — first and second inter-layer spacing changes and

Table 7.4 Optimised parameter values for selected Phase 2 models. Δ parameters are relaxations, and Γ parameters are lateral displacements. Parameters are discussed in more detail in the the text.

Parameter	MEIS	CAICISS
McLoughlin alloy		
Δ_{12}	$-0.07\,(\pm1.08)$	$-0.28\,(\pm0.25)$
Δ_{23}	$+0.06\,(\pm0.09)$	$+0.04\,(\pm0.23)$
Δ_{Sn}	$-0.03\,(\pm0.50)$	$+0.50\,(\pm0.55)$
Nara alloy		
Δ_{12}	$-0.04\,(\pm0.97)$	$-0.27\,(\pm0.27)$
Δ_{23}	$+0.05\,(\pm0.09)$	$-0.02\,(\pm0.21)$
Δ_{Sn}	$+0.22\,(\pm0.89)$	$+0.70\,(\pm0.43)$
Γ_1	$-0.01\,(\pm1.03)$	$-0.34\,(\pm1.65)$
Γ_2	$-0.18\,(\pm0.67)$	$-0.47\,(\pm0.82)$
Lallo alloy		
Δ_{12}	$+0.03\,(\pm0.40)$	$-0.19\,(\pm0.34)$
Δ_{23}	$+0.02\,(\pm0.10)$	$-0.03\,(\pm0.20)$
Δ_{Sn}	$+0.37\,(\pm0.23)$	$+0.00\,(\pm0.50)$
Δ_{Cu}	$+0.04\,(\pm2.12)$	$+0.00\,(\pm0.50)$
Γ_{Sn}	$+0.05\,(\pm0.21)$	$-0.65\,(\pm2.38)$
$\Gamma_{\mathrm{Cu:1}}$	$+0.02\,(\pm0.24)$	$-0.13\,(\pm0.57)$
$\Gamma_{\mathrm{Cu:2}}$	$+0.29\,(\pm0.12)$	$+0.28\,(\pm0.36)$

† Γ parameters are illustrated by arrows in the illustrations of Section 7.1

accompanying Sn relaxation (Δ_{12}, Δ_{23}, Δ_{Sn}), two diagonal lateral displacement parameters — one for the relevant surface Cu atoms and another for Sn atoms ($\Gamma_{Cu:1}$, Γ_{Sn}), the lateral displacement of surface atoms about the glide plane ($\Gamma_{Cu:2}$), and an additional relaxation of relevant surface Cu atoms due to subsurface vacancies (Δ_{Cu}).

There are large inconsistencies between the results from the two techniques. The Nara model is the most consistent, with four out of five parameters matching in the direction of displacement, although some very different parameter amplitudes are seen. The parameter values obtained from MEIS analysis are all plausible, CAICISS less so, and both seem to be returning nonsensical error estimates for many structural parameters.

It is unclear why the errors have been so vastly overestimated. One possibility is that there could be a large rumpling in multiple layers near the surface. Surface vibration parameters can be included in SOAR, and are a good way of introducing a random rumpling in each layer. These parameters are generally allowed to increase up to 200 % of the bulk values — enough to allow fitting of the expected surface thermal vibration enhancements. Examination of the vibration parameter output (not shown) for this MEIS analysis shows that, in every case, vibrations reached the cap imposed. Large error estimates then arise as SOAR fails to fit the data using the intervals defined.

CAICISS parameter values show some unusually large amplitudes. The problems with CAICISS fitting may also be a result of large surface rumpling. Certainly, there is either something in the analysis that has not been taken into account, or the quality of Cu scattering data collected was less than ideal for both techniques.

Examination of parameter values does not allow any further exclusion to be made from the remaining three models, although all three being surface alloy models lends weight to Phase 2 being an alloy. No values for structural parameters have been determined with any degree of certainty. Additional CAICISS scattering information from Sn atoms allows further distinction to be made between the remaining alloy models. By comparing the positions of surface peaks for each model, it was possible to exclude two more models, leaving only one. It is the conclusion of this investigation that the Lallo [high Cu density] alloy model provides the best candidate for Phase 2.

CHAPTER 8

Cu(100)/Sn: Intermediate Phase

Unlike the other phases of the Cu(100)/Sn system, Phase 2.5 was not observed in the original work conducted by Argile and Rhead [77] — it was a later study by Martínez-Blanco et al. [80] which proposed an intermediate phase between Phase 2 and Phase 3. Phase 2.5, as it will be referred to in this study, is thermally unstable with a $p(2\times2)$ structure above 360 K and what is believed to be a complex $\left(\begin{smallmatrix}-4 & 2\\ 0 & 4\end{smallmatrix}\right)$ structure below.

No viable structural model was proposed for this phase until the study conducted by Lallo et al. [81]. They proposed two possible structures — one overlayer and one surface alloy — for the phase, shown in Figure 8.1. The models differ only in the number of Cu atoms in the outermost layer. The models are based on a $c(4\times8)$ structure, rather than the complex superlattice originally proposed [80], and have an approximate coverage of 0.38 ML. Most Sn atoms sit in hollow sites, but some are displaced, with two glide planes present in the unit cell. Analysis of STM images collected by Lallo et al. was unable to distinguish between the overlayer and alloy structures. The authors also note that only small patches of the surface seem able to support this phase at any one time, surrounded by disordered areas of higher Sn density.

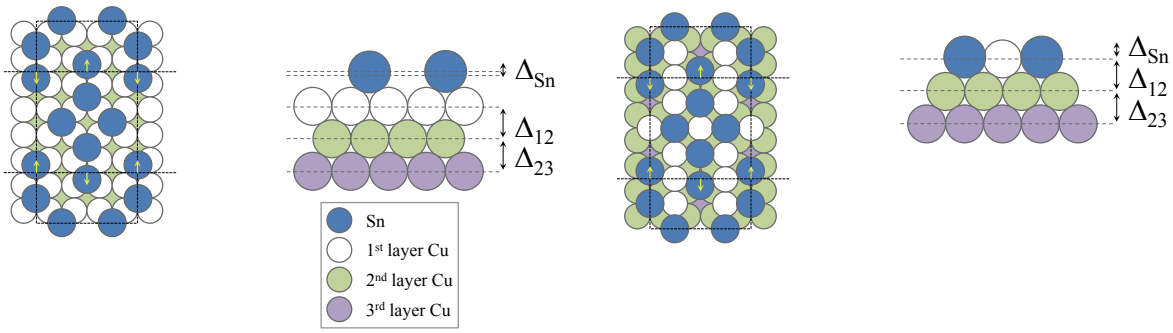

(a) Lallo overlayer model (b) Lallo alloy model

Figure 8.1 Schematics of the two trial structures proposed by Lallo for Phase 2.5.

8.1 Results

The surface was cleaned with IBA cycles, as described previously, and Sn deposited for 29 minutes. The LEED pattern observed at 114 eV is shown in Figure 8.2. A schematic proposed by Martínez-Blanco et al. [80] is also shown. The LEED pattern observed does not match this schematic, but was the closest obtained. Using the calibrated deposition rate of 0.012 MLmin^{-1}, the coverage is estimated to be approximately 0.35 ML. A very small addition of Sn is needed to go from Phase 2 (0.32 ML) to Phase 2.5. This disagrees with the observations of Martínez-Blanco, who found the approximate coverage to be 0.45 ML, and suggests that the data presented in this thesis was not that of a perfect Phase 2.5. However, continued deposition resulted in no improvement to the LEED pattern — Phase 3 spots began to appear instead. The obvious differences between the LEED pattern observed and that seen in previous studies mean that results obtained from analysis of MEIS and CAICISS data on this phase must be taken as preliminary.

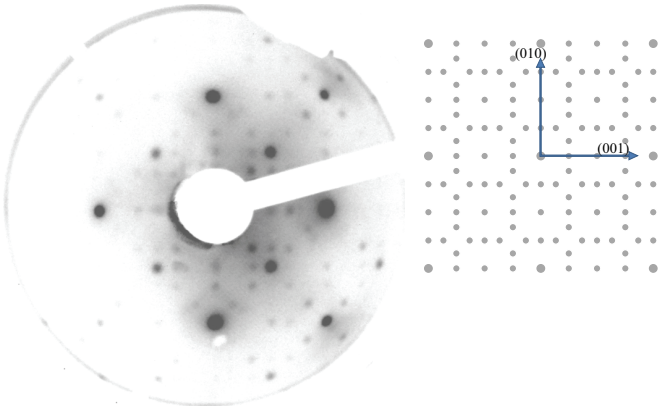

Figure 8.2 Illustration of the LEED pattern seen for Phase 2.5 at 114 eV. The calibrated deposition rate of 0.012 MLmin^{-1} gives an approximate coverage of 0.35 ML after 29 minutes of Sn exposure. A photograph and a sketch are shown; the sketch shown is a schematic for the phase proposed by Martinez-Blanco [80].

8.1.1 MEIS

Processed MEIS data collected on the nearest match to Phase 2.5 are shown in Figure 8.3. Both Sn datasets were flat, consistent with a single layer of adsorbate atoms. The Cu data from the ⟨110⟩ incident direction look good, but there is a worrying absence of many of the expected bulk scattering dips in the ⟨211⟩ direction. Multiple scans were taken, but all show the same lack of features. Further fitting will be conducted to be sure, but it appears as though some of the MEIS data collected on this phase may be unusable.

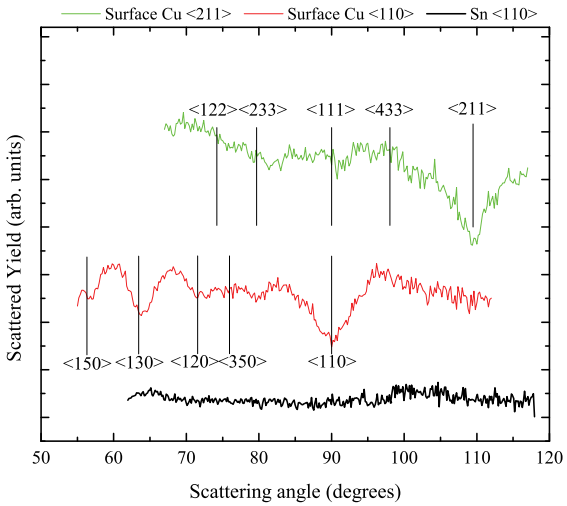

Figure 8.3 Processed Phase 2.5 MEIS data. Data have been vertically translated for clarity. Note that the Sn data shows no blocking features.

R-factor analysis favours the surface alloy rather than the overlayer model (see Table 8.1), but the R-factors are larger than seen in most other phases. Examination of the fitted spectra (Figure 8.4) reveals that the suspect $\langle 211 \rangle$ data collected does indeed appear to be erroneous. Neither model matches, and the erroneous data inflates the R-factor. The lower R-factor of the alloy model arises predominantly from the smaller discrepancy seen in the dip around 57° scattering angle in the $\langle 110 \rangle$ dataset. MEIS analysis is inconclusive. Additional data collection is needed on this phase for MEIS to be able to draw any quantitative structural conclusion. There is further discussion of MEIS data after analysis of CAICISS findings.

Table 8.1 MEIS Cu scattering R-factors for Phase 2.5 trial structures.

Model	Initial R-factor	Final R-factor
Lallo: Overlayer	22.76	9.87
Lallo: Surface Alloy	18.92	9.13

8.1.2 CAICISS

Examination of the fitted CAICISS spectra in Figure 8.5 shows — as expected — how similar the two models are. The most obvious difference between the two simulations arises from shallow angle backscattering where differing amounts of Cu are visible. The alloy model has Cu atoms in the outermost layer, so there is more Cu visible at shallow angles and the surface peak is larger. This is clearly demonstrated in the data — the alloy model has a larger surface peak in both azimuths. Unfortunately, this is the only differentiating factor between the models, and neither matches particularly well to the spectrum as a whole. It was hoped that

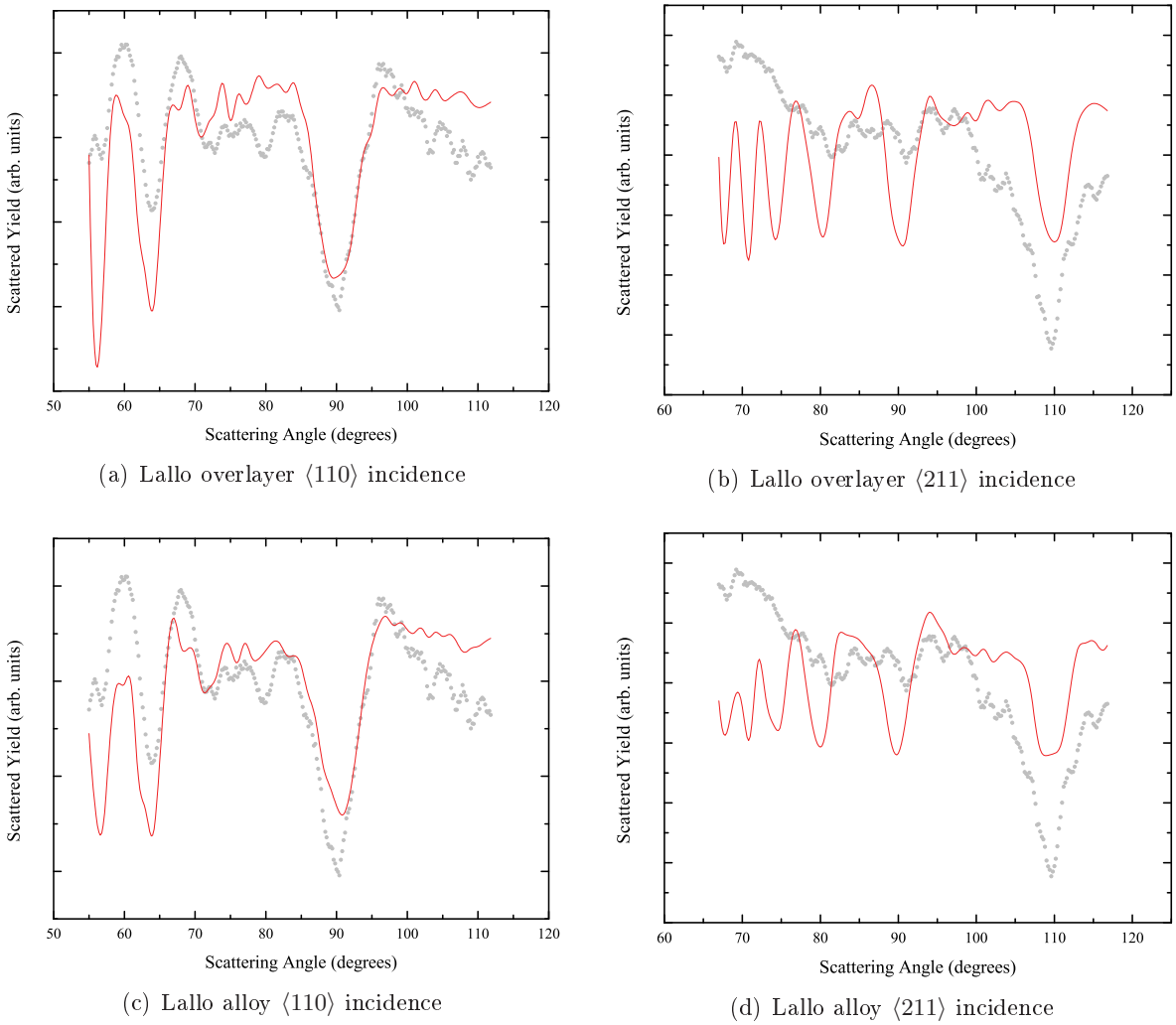

(a) Lallo overlayer ⟨110⟩ incidence

(b) Lallo overlayer ⟨211⟩ incidence

(c) Lallo alloy ⟨110⟩ incidence

(d) Lallo alloy ⟨211⟩ incidence

Figure 8.4 Optimised MEIS Cu scattering fits from SOAR for Phase 2.5. Experimental data are shown by scatter points, and VEGAS simulations by solid lines.

examination of the parameter values (Table 8.2) might show which solution is more physically sensible, but the very large error estimates on all these means there is little confidence in the fit of either model. Surface Debye temperatures of 340 K for Cu, and 170 K for Sn provided the best vibrational fit for this phase — approximately 190 % of the vibrational amplitude of bulk Cu, and 160 % of bulk Sn.

Table 8.2 Optimised parameter values from SOAR for CAICISS Phase 2.5 models.

Parameter	Lallo Overlayer	Lallo Surface Alloy
Δ_{12}	$--$	$-0.20\,(\pm 0.31)$
Δ_{23}	$-0.23\,(\pm 0.21)$	$-0.26\,(\pm 0.23)$
$\Delta_{\mathrm{Sn:1}}$	$+0.13\,(\pm 0.97)$	$+0.56\,(\pm 0.76)$
$\Delta_{\mathrm{Sn:2}}$	$-0.20\,(\pm 0.53)$	$+0.24\,(\pm 0.67)$
Γ_1	$+0.00\,(\pm 0.39)$	$+0.18\,(\pm 0.87)$

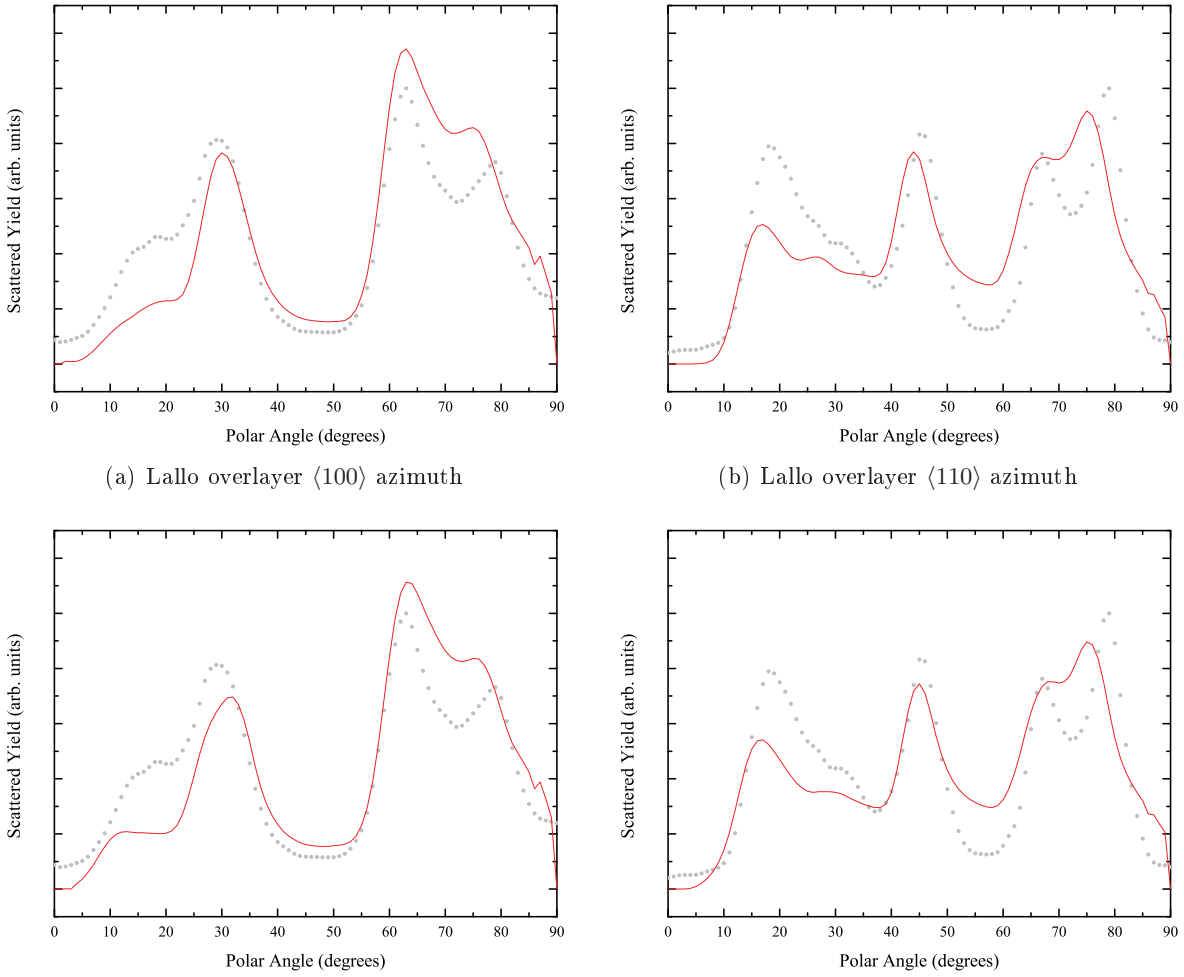

(a) Lallo overlayer ⟨100⟩ azimuth

(b) Lallo overlayer ⟨110⟩ azimuth

(c) Lallo alloy ⟨100⟩ azimuth

(d) Lallo alloy ⟨110⟩ azimuth

Figure 8.5 Optimised CAICISS Cu backscattering fits from SOAR for Phase 2.5.

CAICISS Cu backscattering analysis is inconclusive on this phase. The near identical nature of the models means that the data collected simply is not accurate enough to be able to differentiate them. Final R-factors are shown in Table 8.3.

Table 8.3 CAICISS Cu backscattering R-factors for Phase 2.5 trial structures.

Model	Initial R-factor	Final R-factor
Lallo: Overlayer	7.53	5.44
Lallo: Surface Alloy	6.79	5.09

8.1.3 CAICISS Sn backscattering

Analysis of CAICISS data so far has focused on the backscattered Cu signal, which relies on inferring the position of adsorbed Sn atoms from shifts in the Cu spectrum features. What little differences are seen between simulations of the two models can easily be explained by the limited resolution of the CAICISS scans. However, examination of the Sn scattering signal

may show some differences, especially at grazing incidence; the amount of Sn visible and the location of the surface peak will change depending on whether the surface is an alloy or an overlayer.

Figure 8.6 shows simulated Sn scattering spectra for each model, along with experimental data. The surface peak position appears to show that the Lallo:1 (overlayer) model is a better candidate for this phase. Some additional peaks in the experimental spectrum are not reproduced in the simulations. Those features arise from the underlying Cu layers, and have appeared due to beam chopping problems. Unfortunately, such spurious peaks were unavoidable until improvements were later made to the CAICISS system (see Chapter 12).

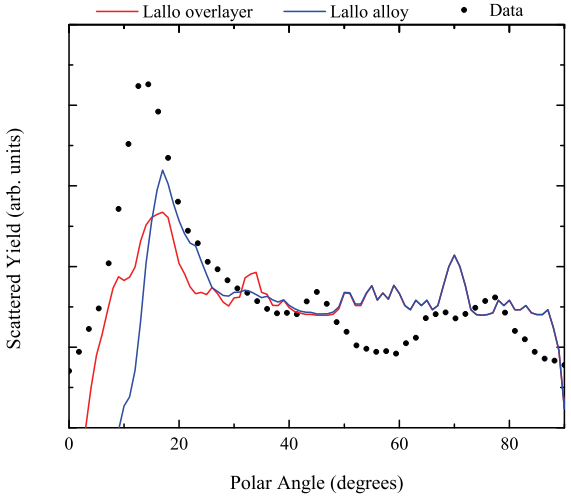

Figure 8.6 Comparison of Phase 2.5 Sn CAICISS backscattered experimental spectrum with computer simulations from proposed models.

8.2 Conclusions

MEIS cannot produce any conclusive answer as to which of the two models is better for Phase 2.5, which, given the similarity of the two models, is not entirely surprising. CAICISS faired no better under examination of Cu backscattering data, although differences were seen in the Sn scattering spectra — the overlayer model could be said to provide a better surface peak fit. The MEIS data collected are questionable, and the large error estimates obtained from CAICISS analysis mean that the parameter values obtained are unreliable. It has already been noted that it was not possible during the course of this study to reproduce the original LEED patterns observed by Martínez-Blanco and Lallo, although a similar phase was seen. This will undoubtedly have contributed to the difficulties in fitting to the models proposed by Lallo. More data collection is needed on this phase.

CHAPTER 9

Cu(100)/Sn: Phase 3

Phase 3 was identified in the first instance by Argile and Rhead [77]. They proposed a $c(2\times2)$-based overlayer structure — which can also be described as a $p(3\sqrt{2}\times\sqrt{2})\mathrm{R}45^\circ$ — with all Sn atoms either in, or near, hollow sites. Through examination of LEED I-V data they concluded that the surface unit cell of Phase 3 must contain three Sn atoms — two would not be compatible with the attenuation observed, and four would make it more dense than the higher coverage Phase 4. The incorporation of a missing row of Sn atoms, as shown in Figure 9.1(a), provides the necessary periodicity and Sn atom density.

McLoughlin et al. [78] reinvestigated Phase 3. By using a calibrated rate of deposition, the authors were able to ascertain that the transition from Phase 2 is completed by addition of only an extra ≈ 0.10 ML of Sn. A new overlayer model was proposed (Figure 9.1(b)) still based on a $c(2\times2)$ superlattice, but with no missing row. Instead, pairs of Sn atoms are 'pinched' together, providing a means of surface strain relief. The authors also showed through LEED simulations that the amount of lateral displacement produces a noticeable change in the diffraction spots, with a 0.2 Å shift per atom providing the best match.

Pussi et al. [79] conducted a further study as an extension to the work of McLoughlin. Up until this study only two structures had been proposed, both of which were based on an overlayer of Sn atoms. It was the belief of the authors that an alloy structure is favoured according to TLEED data. Pussi et al. examined variations on the Argile and Rhead and the McLoughlin models and arrived at a third potential model based on a $c(2\times2)$ surface alloy structure — an alloy equivalent of the McLoughlin overlayer model. Further improvement to the agreement of the alloy model was gained by removing every third row of Cu atoms in the outermost layer (Figure 9.1(c)). Strain is released in the Pussi missing row model by both lateral relaxations and rumpling within the layers. The combination of relaxations and displacements in the surface layer means that the unit cell contains two inequivalent Sn atoms.

The first STM images of Phase 3 were published by Nara [82]. All images were consistent with the Sn atom positions of the Pussi model, although the existence of a missing row of surface Cu atoms could not be confirmed from the images taken. Further STM images taken by

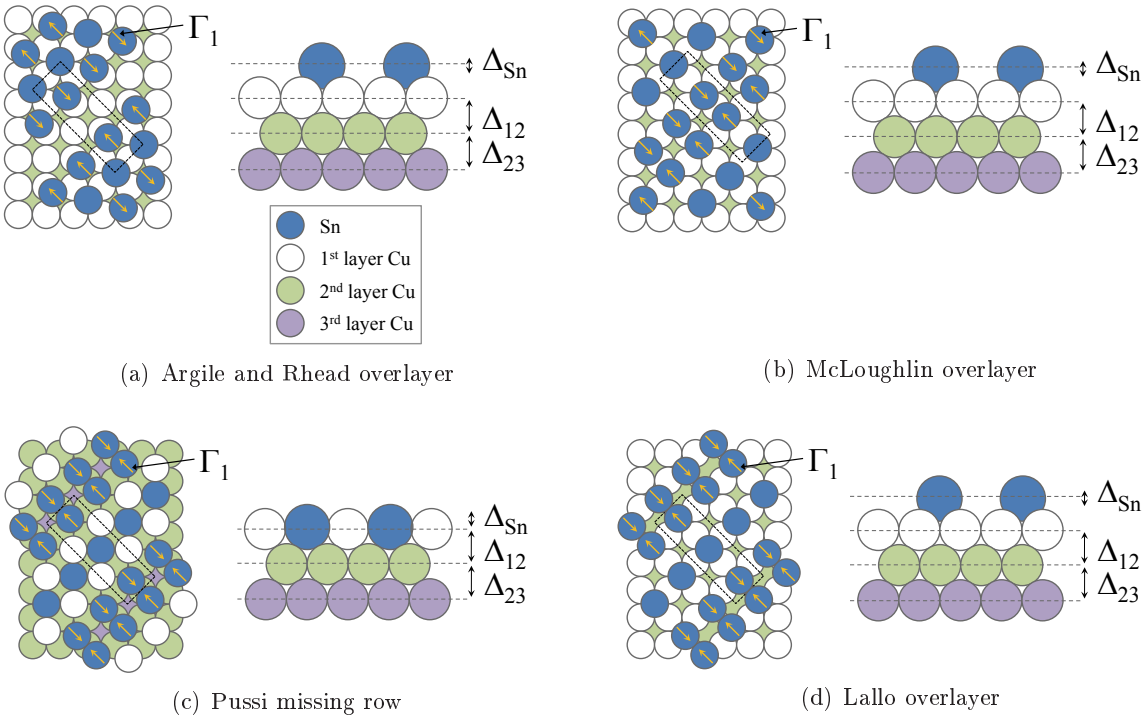

(a) Argile and Rhead overlayer

(b) McLoughlin overlayer

(c) Pussi missing row

(d) Lallo overlayer

Figure 9.1 Schematics of the four trial structures and structural parameters proposed for Phase 3.

Lallo et al. [81] are also fully consistent with the model suggested by Pussi, however a possible alternative structure is put forward by the authors — an overlayer structure with subsurface missing Cu atom rows (see Figure 9.1(d)). While the authors concede that subsurface missing rows are a less commonly accepted means of surface stress relief, the model is no less valid as a candidate. The inability of STM images to reliably distinguish the overlayer and alloy models means that no models can yet be excluded — all models will be compared with ion scattering data in order to resolve this surface.

One final study conducted by Martìnez-Blanco et al. [80] investigated a reversible phase transition at 360 K between the $p(3\sqrt{2}\times\sqrt{2})R45°$ (Phase 3) and a new high temperature phase with a $p(\sqrt{2}\times\sqrt{2})$R45 ° structure. No new models were proposed for either high or low temperature phases as a result of this work. No MEIS or CAICISS data have yet been collected on the high temperature phase.

9.1 Results

The surface was cleaned with IBA cycles — as detailed previously — and Sn deposited for 35 minutes. The LEED pattern observed at 213 eV is shown in Figure 9.2. At the relatively high electron energy used — compared to other phases imaged in this study — spots outside the initial (1×1) of the clean surface can be seen in the image. The (1×1) area is marked

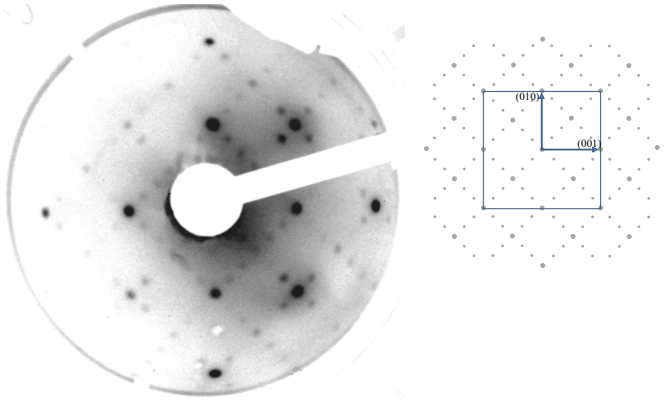

Figure 9.2 Illustration of the LEED pattern seen for Phase 3 at 213 eV. The calibrated deposition rate of 0.012 MLmin^{-1} gives an approximate coverage of 0.42 ML after 35 minutes of Sn exposure. A photograph and a sketch are shown; the sketch is reproduced from the work of Argile and Rhead [77].

with a square. The LEED pattern and Sn coverage are both in excellent agreement with previous studies [77, 78] and AES showed no surface contamination. McLoughlin calculated the change from Phase 2 to Phase 3 was completed by adding approximately 0.10 ML of Sn — a calculation verified by the LEED patterns in this study; Phase 2 was found to have a coverage of approximately 0.32 ML. And, using the calibrated deposition rate of 0.012 MLmin^{-1}, the Phase 3 coverage is estimated to be approximately 0.42 ML. MEIS and CAICISS data were collected in the same geometries as previous phases (MEIS incident directions of $\langle 110 \rangle$ and $\langle 211 \rangle$, and CAICISS azimuths of $\langle 100 \rangle$ and $\langle 110 \rangle$). Illustrations of the geometries can be found in Section 5.1.1.

9.1.1 MEIS

Figure 9.3 shows the MEIS data for Phase 3. Sn data contains no blocking features in either incident direction, indicating no sub-surface penetration of Sn atoms — consistent with all proposed models. Both Cu datasets have major blocking features labelled to correspond with crystallographic directions identified in Figure 5.2.

By comparing raw MEIS data with bulk fits for each of the models proposed, two models can be identified as providing the most likely solution. Figure 9.4 shows bulk fits for each of the models. By visual examination alone, it is clear the Argile and Rhead ('Argile') and 'McLoughlin overlayer' models are the worst-fitting of the five models. The 'McLoughlin alloy' model has no missing row, but is otherwise identical to the 'Pussi' model. Inclusion of a missing row clearly improves the fit in the $\langle 211 \rangle$ incident direction in the region between 95° and 105° scattering angle. The improvement to the fit is supported by the R-factor analysis shown in Table 9.1. The 'Lallo' overlayer model is the best fit in the R-factor analysis. Visual analysis

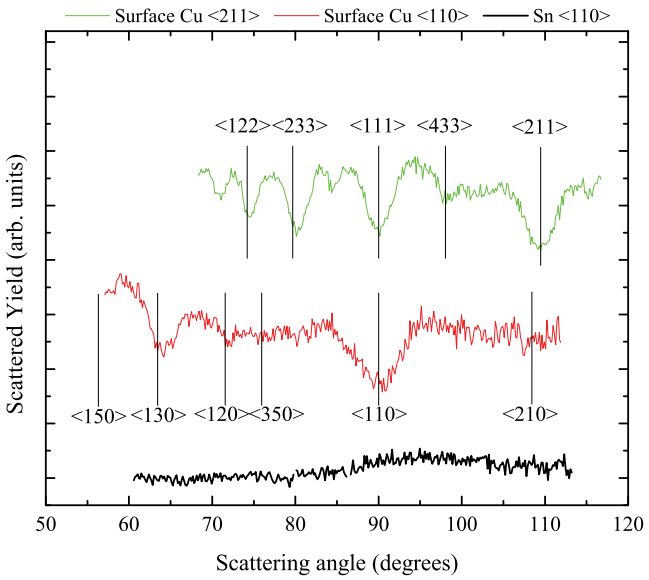

Figure 9.3 Processed Phase 3 MEIS data. Data have been vertically translated for clarity. Note that the Sn data shows no blocking features.

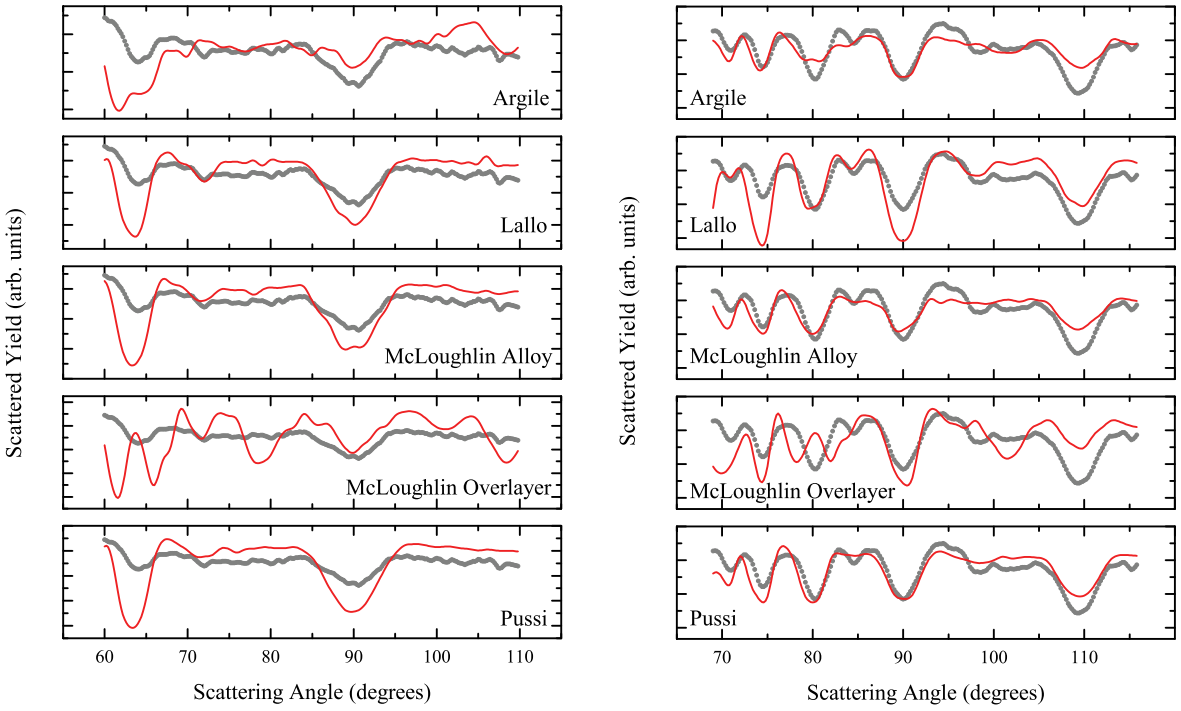

(a) ⟨110⟩ incidence (b) ⟨211⟩ incidence

Figure 9.4 Bulk MEIS Cu scattering fits for Phase 3 models.

shows the intensities of smaller features in the ⟨211⟩ incidence data are reproduced better than with any other model — particular attention is drawn to the regions 83° to 87°, and 95° to 105° — although the relative intensities of larger features seem to be better fitted by the Pussi model. Only two models need be pursued further in the MEIS and CAICISS analysis — the Pussi alloy and Lallo overlayer.

Table 9.1 Initial MEIS R-factors for Phase 3 trial structures.

Model	MEIS R-factor	
Argile and Rhead	10.82	
McLoughlin: Overlayer	13.30	
McLoughlin: Alloy variant	9.33	
Pussi: Missing row alloy	8.50	$\Longleftarrow$
Lallo: Overlayer	7.31	$\Longleftarrow$

Figure 9.5 shows the final optimised fits with MEIS data for both models. Final R-factors of 2.88 and 4.35 were obtained for the Pussi and Lallo models respectively, which suggests that the Pussi model should provide a significantly better fit.

Visual examination of the fits does not seem to correlate with the much better R-factor returned by the Pussi model. The finer MEIS features do not seem to be well reproduced in either case. Both models struggle to fit data at low scattering angle — possibly because the models contain too much blocking or because the nature of the Sn adsorption sites is not well matched — and there are other obvious problems with relative intensities of features.

Table 9.2 shows the final parameter output from SOAR. Not shown in the table, both models exhibit very large (> 200 % of bulk) surface vibrational amplitudes, suggesting that a large amount of rumpling is required in both models in order to fit the data. The Lallo model exhibits a large surface Sn atom offset towards the outermost Cu layer. The parameter is clamped at a maximum value of ± 0.40, and that limit has been reached during fitting. The Pussi model contains parameters with very near zero values, meaning that SOAR was unable to find an improved fit in the intervals examined. There is a pinching together of Sn atoms about the missing row as expected and interlayer spacings are near identical to that of a bulk Cu crystal. The zero value for Sn relaxation is a surprising result given the difference in radii between Sn and Cu — one would expect the resulting surface stress to induce some preferential rumpling; the zero value with large vibrational amplitudes suggests that the rumpling is more random. MEIS analysis seems to suggest that the Pussi model be favoured.

Table 9.2 Optimised parameter values from SOAR for MEIS Phase 3 models.

Parameter	Pussi	Lallo
Δ_{12}	$+0.00\,(\pm 0.10)$	$+0.02\,(\pm 0.10)$
Δ_{23}	$+0.00\,(\pm 0.10)$	$+0.05\,(\pm 0.07)$
Δ_{Sn}	$+0.00\,(\pm 0.10)$	$-0.40\,(\pm 0.14)$
Γ_1	$-0.40\,(\pm 0.17)$	$+0.40\,(\pm 0.18)$

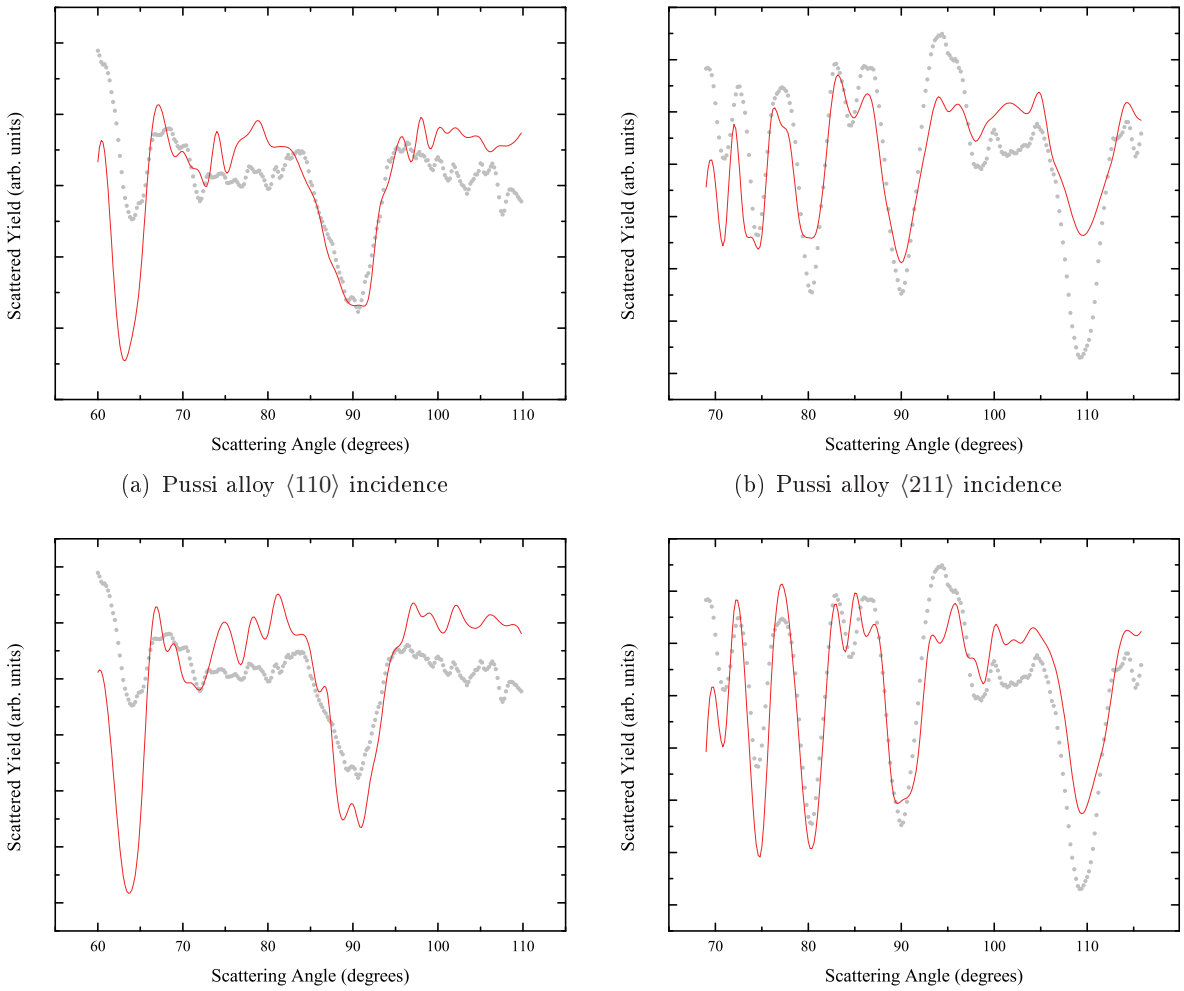

(a) Pussi alloy ⟨110⟩ incidence

(b) Pussi alloy ⟨211⟩ incidence

(c) Lallo overlayer ⟨110⟩ incidence

(d) Lallo overlayer ⟨211⟩ incidence

Figure 9.5 Optimised MEIS Cu scattering fits from SOAR for Phase 3. Experimental data are shown as scatter points, and VEGAS simulations as solid lines.

9.1.2 CAICISS

Structural fits were conducted for CAICISS data, returning initial R-factors of 6.47 and 6.69 for the Pussi alloy and Lallo overlayer models respectively. Simulations were examined for a number of different surface Debye temperatures. A surface Cu Debye temperature of 340 K provided a better fit than the bulk value (520 K). Applying Equation 3.9 shows this corresponds to approximately a 150 % of the vibrational amplitude of bulk Cu. A surface Sn Debye temperature of 170 K was found to improve the fits, giving a vibrational amplitude approximately 160 % that of bulk Sn.

The final optimised CAICISS spectra are shown in Figure 9.6. Visual examination of the surface peak alone is enough to show the Pussi model is a better fit to the CAICISS data collected. An overlayer structure has less Cu visible at shallow incident angle, and therefore has a reduced surface peak intensity. Surface Debye temperatures were re-examined after

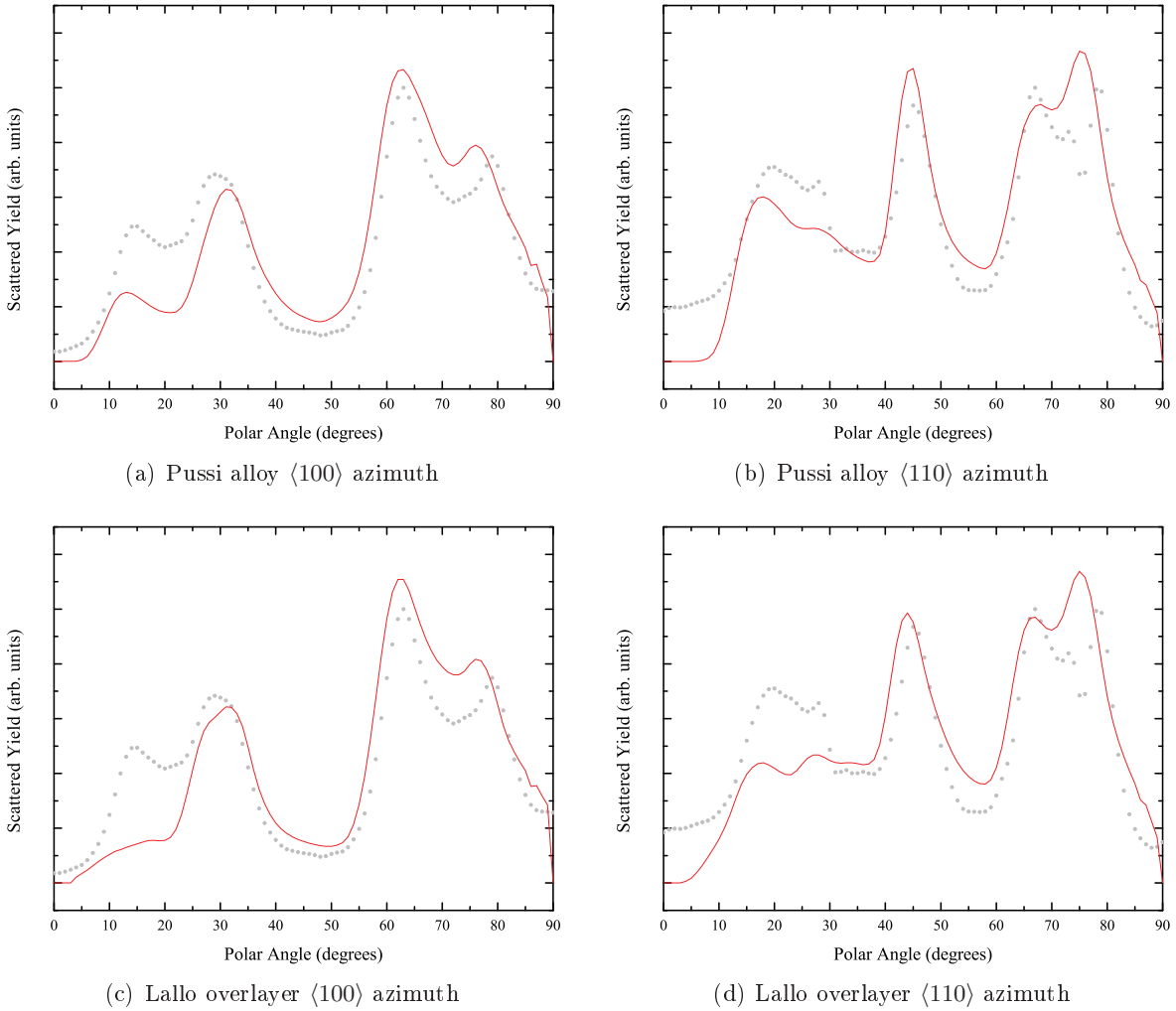

(a) Pussi alloy ⟨100⟩ azimuth

(b) Pussi alloy ⟨110⟩ azimuth

(c) Lallo overlayer ⟨100⟩ azimuth

(d) Lallo overlayer ⟨110⟩ azimuth

Figure 9.6 Optimised CAICISS Cu backscattering fits from SOAR for Phase 3. Experimental data are shown as scatter points, and VEGAS simulations as solid lines.

SOAR fitting to see if the values could be modified to improve the final fit further. No notable improvement in the fits could be achieved with modified values. The final R-factor analysis reflects the better fit of the surface peaks, with the Pussi and Lallo models returning values of 4.79 and 5.04 respectively.

Examination of the structural parameter values output from SOAR (see Table 9.3) leads to a similar conclusion. The additional parameter shown in Table 9.3 ($\Delta_{\mathrm{Sn:2}}$) is included as

Table 9.3 Optimised parameter values from SOAR for CAICISS Phase 3 models.

Parameter	Pussi	Lallo
Δ_{12}	$+0.00\,(\pm0.10)$	$-0.22\,(\pm0.22)$
Δ_{23}	$-0.02\,(\pm0.02)$	—
Δ_{Sn}	$+0.00\,(\pm0.10)$	$+0.00\,(\pm0.10)$
$\Delta_{\mathrm{Sn:2}}$	$-0.19\,(\pm0.11)$	$-0.19\,(\pm0.13)$
Γ_1	$-0.26\,(\pm0.18)$	$-0.57\,(\pm0.43)$

a refinement to the MEIS analysis. It is an additional relaxation that creates inequivalent Sn atoms in the surface layer. It allows relaxation of the Sn atoms adjacent to the missing row, thus introducing some ability for SOAR to actually fit the rumpling of the surface layer without resorting to large vibrational amplitudes. It is obvious from Table 9.3 that the Pussi model returns the more plausible parameter values.

9.1.3 CAICISS Sn backscattering

Figure 9.7 shows the Sn backscattering spectra. The experimental data show a very wide surface peak. Neither model matches the location of the surface peak well. The simulation of the Lallo overlayer model provides a slightly wider surface peak, but the plot is far from conclusive.

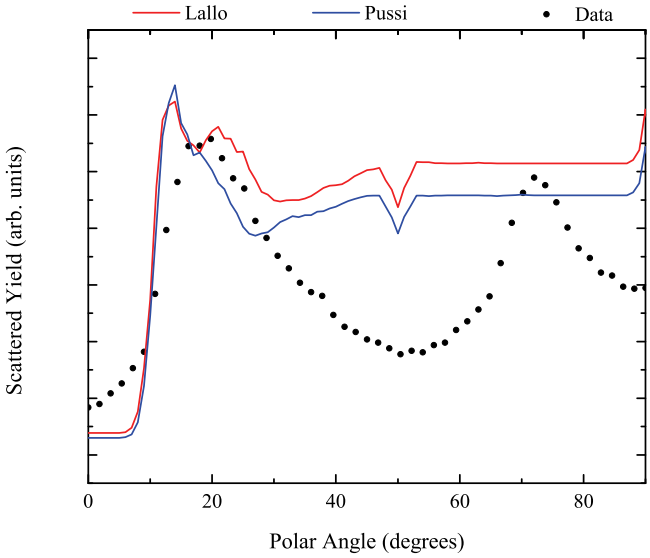

Figure 9.7 Comparison of Phase 3 Sn CAICISS backscattered experimental spectrum with computer simulations from proposed models.

9.2 Conclusions

In both cases (MEIS and CAICISS) the Pussi model returns the better R-factor of the two models. Examination of spectra and structural parameter values also indicates that the Pussi model should be favoured. As a final confirmation that the Pussi model is a good description of Phase 3, the parameter values obtained through SOAR were compared to the corresponding values proposed by Pussi et al. in their original paper [79]. Table 9.4 shows the SOAR values alongside those of the original Pussi paper. The Pussi model also includes a large amount of rumpling in subsurface layers, which is not included in the MEIS or CAICISS models. This may account for some of the differences seen in parameter values — particularly Cu

relaxations. The most obvious discrepancy is that of Δ_{Sn}. Both MEIS and CAICISS analysis return a value near zero shift, but Pussi suggests a value of over 0.3 Å; the reasons for this are unclear — one would certainly expect that the much larger Sn atoms would sit above the surface layer of Cu atoms in order to relieve surface stress, although the missing row does provide an alternative means of stress relief, and large vibrational amplitudes are seen which suggest surface rumpling. Overall, the agreement with the work of Pussi et al. is good, with most parameter values falling within the error estimates.

Table 9.4 Comparison of structural parameters proposed by Pussi and those returned by SOAR optimisations.

Parameter	Pussi	MEIS	CAICISS
Δ_{12}	$+0.06\,(\pm0.04)$	$+0.00\,(\pm0.10)$	$+0.00\,(\pm0.10)$
Δ_{23}	$+0.01\,(\pm0.04)$	$+0.00\,(\pm0.10)$	$-0.02\,(\pm0.02)$
Δ_{Sn}	$+0.33\,(\pm0.07)$	$+0.00\,(\pm0.22)$	$+0.00\,(\pm0.10)$
$\Delta_{Sn:2}$	$-0.12\,(\pm0.08)$	–	$-0.19\,(\pm0.13)$
Γ_1	$-0.26\,(\pm0.10)$	$-0.40\,(\pm0.17)$	$-0.26\,(\pm0.18)$

CHAPTER 10

Cu(100)/Sn: Phase 4

Phase 4 is the most dense of the Sn reconstructions observed. Argile and Rhead [77] interpreted the phase as a complete overlayer of Sn, with a coverage of 0.625 ML and $c(4\times4)$-based structure (see Figure 10.1(a)). The authors observed that continued deposition (after reaching perfection in Phase 4) results in spots gradually disappearing to be replaced by a uniform background intensity, presumed to result from the formation of a disordered second layer.

Later application of helium atom scattering (HAS) by Lallo et al. [81] to Phase 4 proved to be largely consistent with the observations of Argile and Rhead. The authors note that they cannot be certain that the $c(4\times4)$ Phase 4 structure fills the entire surface — at coverages greater than that of Phase 4 even the specular feature of the LEED pattern is absent. Analysis of STM line scans revealed that the number density of high-Sn features was less than the anticipated Sn density, leading to a new model with Sn in multiple layers — a combination of overlayer and second layer alloying. There are two two inequivalent Sn atom positions and lateral displacement of Sn atoms from four-fold hollow sites (see Figure 10.1(b)). MEIS and CAICISS have been applied to Phase 4. Analysis of the Sn scattering signal should provide more evidence whether the phase is single or multi-layer.

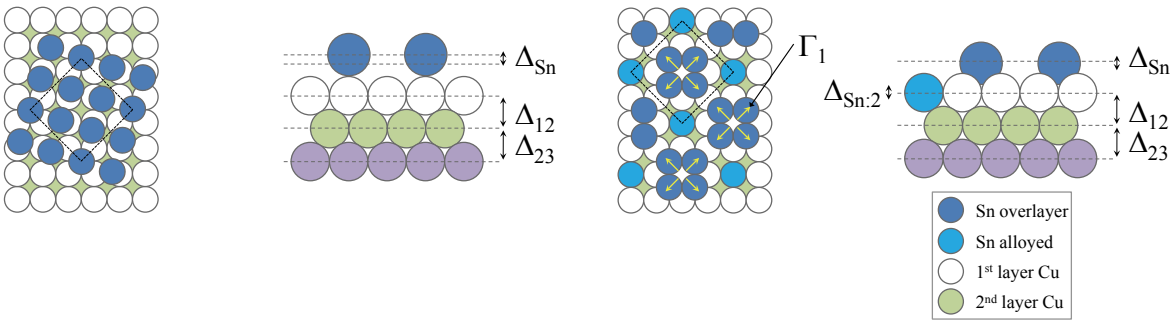

(a) Argile and Rhead overlayer (b) Lallo overlayer

Figure 10.1 Schematics of the two trial structures proposed for Phase 4.

10.1 Results

The surface was cleaned with IBA cycles, and Sn deposited for 52 minutes to reproduce Phase 4. The LEED pattern observed — at 108 eV — is shown in Figure 10.2 along with a schematic reproduced from the work of Argile and Rhead [77]. Using the calibrated deposition rate of 0.012 MLmin^{-1}, the coverage is estimated to be approximately 0.62 ML. The LEED pattern and Sn coverage are both in excellent agreement with previous studies [77, 78, 81] and AES showed no surface contamination.

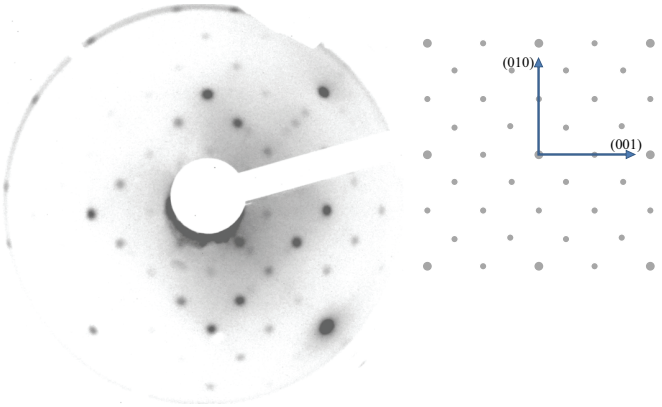

Figure 10.2 Illustration of the LEED pattern seen for Phase 4 at 108 eV. The calibrated deposition rate of 0.012 MLmin^{-1} gives an approximate coverage of 0.62 ML after 52 minutes of Sn exposure. A photograph and a sketch are shown; the sketch is reproduced from the work of Argile and Rhead [77].

10.1.1 MEIS

Figure 10.3 shows the processed MEIS data for Phase 4. There are no obvious blocking features in the Sn data in either the ⟨110⟩ or ⟨211⟩ datasets, which supports the hypothesis that there is

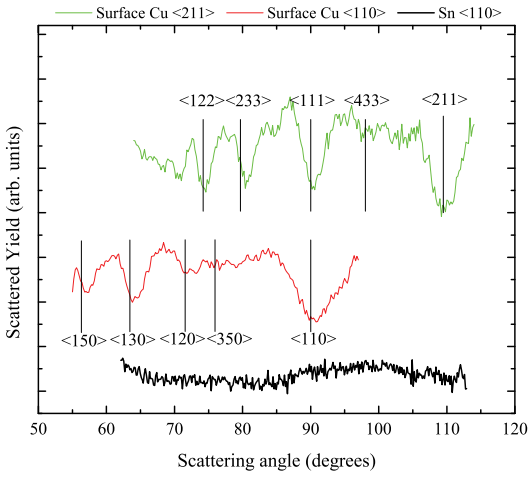

Figure 10.3 Processed Phase 4 MEIS data. Data have been vertically translated for clarity. Note that the Sn data shows no blocking features.

no deep sub-surface penetration of Sn atoms, but the limited resolution of the Sn signal does not conclusively rule out the dual-layer Lallo overlayer model — far fewer counts are returned from the surface Sn than the surface Cu because of the low surface coverage. Both Cu datasets have the major blocking features labelled to correspond with the major crystallographic directions identified in Section 5.1.1.

Figure 10.4 and Table 10.1 shows the final optimised fits with MEIS data for both models and the corresponding R-factors. Final R-factors of 1.03 and 1.28 were obtained for the Argile and Lallo models respectively, which suggests that the Argile model should provide a better fit. Visual examination of the spectra reveals that the majority of the discrepancy between the models is seen in the $\langle 110 \rangle$ direction at low scattering angle. The Argile model matches these surface-specific features more closely. Some differences are also seen between 70° and 80° in the $\langle 110 \rangle$ direction, due to the variation in number of Sn layers in the models. The presence of Sn in the second layer in the Lallo model changes the blocking characteristics; the Lallo model seems to match the experimental data more closely in this region, although neither model provides a totally satisfactory fit. Vibrational analysis of MEIS datasets shows that the Argile model requires the usual enhanced surface vibrations in order to fit the data — with both surface Sn and Cu having vibrations enhanced to ~ 150 % of bulk values. The Lallo model had vibrational parameters included also, but no better fit was found by SOAR than using the bulk values.

Table 10.2 shows the final parameter output from SOAR. The parameter values used to fit the Argile model are all simple inter-layer spacing changes. The best fit was found by starting with all atoms in a bulk Cu lattice, then expanding the second inter-layer spacing (Δ_{23}) , by +0.05 Å, and the height of Sn atoms from the surface ($\Delta_{Sn:1}$) by +0.30 Å. Clean Cu generally

Table 10.1 Initial and Final MEIS R-factors for Phase 4 trial structures.

Model	Initial R-factor	Final R-factor
Argile and Rhead	1.96	1.03
Lallo: Overlayer	10.77	1.21

Table 10.2 Optimised parameter values from SOAR for MEIS Phase 4 models.

Parameter	Argile	Lallo
Δ_{12}	+0.00 (±0.10)	+0.03 (±0.10)
Δ_{23}	+0.05 (±0.10)	+0.03 (±0.08)
$\Delta_{\mathrm{Sn:1}}$	+0.30 (±0.49)	+0.40 (±0.13)
$\Delta_{\mathrm{Sn:2}}$	–	+0.39 (±0.16)
Γ_1	–	+0.53 (±0.19)

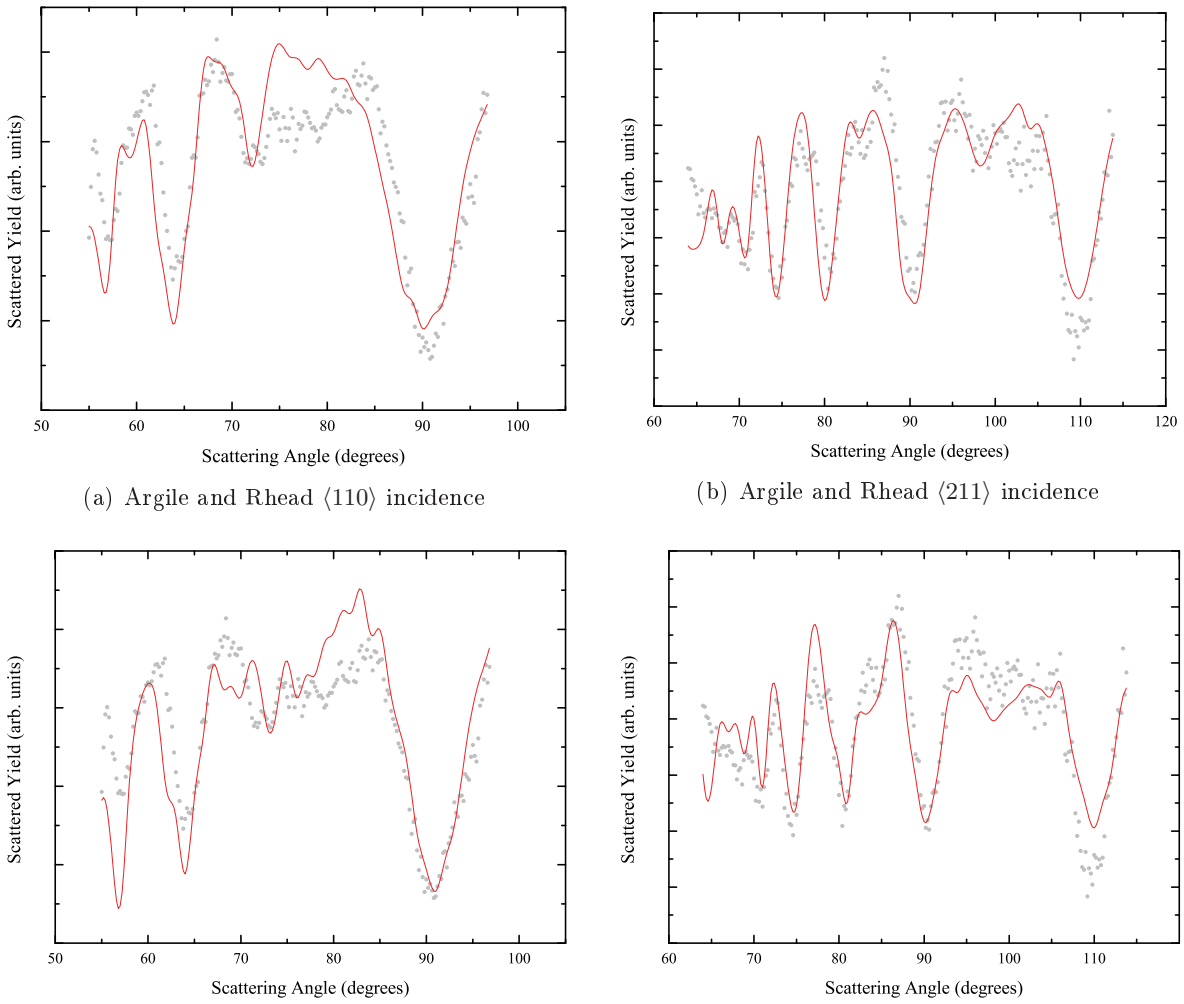

(a) Argile and Rhead ⟨110⟩ incidence

(b) Argile and Rhead ⟨211⟩ incidence

(c) Lallo ⟨110⟩ incidence

(d) Lallo ⟨211⟩ incidence

Figure 10.4 Optimised MEIS Cu scattering fits from SOAR for Phase 4. Experimental data are shown as scatter points, and VEGAS simulations as solid lines.

displays an expansion [4] in the first inter-layer spacing. In this instance, the spacing was unchanged from that of a bulk Cu crystal; most likely an effect of the high mass Sn atoms in the overlayer.

The Lallo model is inherently more complex, containing lateral shifts and Sn atoms at different relaxation levels from the underlying Cu. Still, it can be described by only five parameters — four relaxations and a single lateral shift parameter which acts on multiple atoms from a common centre. Three of the relaxation parameters are equivalent to those used in the Argile model fitting. The additional relaxation parameter ($\Delta_{Sn:2}$) arises from the relaxation of the lower-level alloyed Sn atoms. The lateral shift parameter (Γ_1) allows the four topmost Sn atoms to shift relative to each other. The arrows in Figure 10.1(b) show how the parameter is defined. The parameter acts on all four atoms simultaneously. Lallo fitting shows that the four Sn atoms in the overlayer are pushed apart. When in bulk positions, the

Sn atoms are separated diagonally by 3.62 Å. After application of the lateral shift reported by SOAR, the separation is increased by 29 % — somewhat larger than the increase proposed by Lallo [81] (~ 10 %).

10.1.2 CAICISS

The same structural parameters were applied to each model for CAICISS data analysis. *R*-factor analysis for CAICISS is inconclusive — both models show similar values (see Table 10.3). Vibrational analysis shows that reducing surface Cu Debye temperatures to 340 K provides a better fit, corresponding to ~ 150 % of the vibrational amplitude of bulk Cu. A surface Sn Debye temperature of 170 K was also applied, giving a vibrational amplitude ~ 160 % that of bulk Sn.

Visual inspection of the spectra (Figure 10.5) shows some large discrepancies in surface peak amplitude in both models. The position of the majority of backscattering features is well reproduced, with the exception of the highest polar angle peak. This peak should be the least sensitive to surface changes because it originates (for the most part) from deeper in the crystal structure. The inability of SOAR to fit this peak within the given physically sensible parameter intervals is concerning and warrants further investigation, for which there was no time in this study. Examination of the structural parameter values (Table 10.4) shows some large inter-layer spacing changes, and some equally large error estimates for all parameter values. Similarly to the MEIS analysis, CAICISS analysis of the Lallo model shows that Sn atoms in the outermost layer are laterally displaced in order to fit the experimental data. The inflated error estimates associated with CAICISS fitting have been observed repeatedly, and are believed to be due to a number of factors, one of which is the aforementioned high polar

Table 10.3 Initial and Final CAICISS *R*-factors for Phase 4 trial structures

Model	Initial *R*-factor	Final *R*-factor
Argile and Rhead	7.21	5.34
Lallo: Overlayer	8.59	5.40

Table 10.4 Optimised parameter values from SOAR for CAICISS Phase 4 models.

Parameter	Argile	Lallo
Δ_{12}	$+0.20\,(\pm 0.28)$	$-0.35\,(\pm 0.22)$
Δ_{23}	$+0.15\,(\pm 0.29)$	—
$\Delta_{\mathrm{Sn:1}}$	$+0.34\,(\pm 1.04)$	$+0.39\,(\pm 0.22)$
$\Delta_{\mathrm{Sn:2}}$	—	$+0.40\,(\pm 0.81)$
Γ_1	—	$+0.60\,(\pm 0.47)$

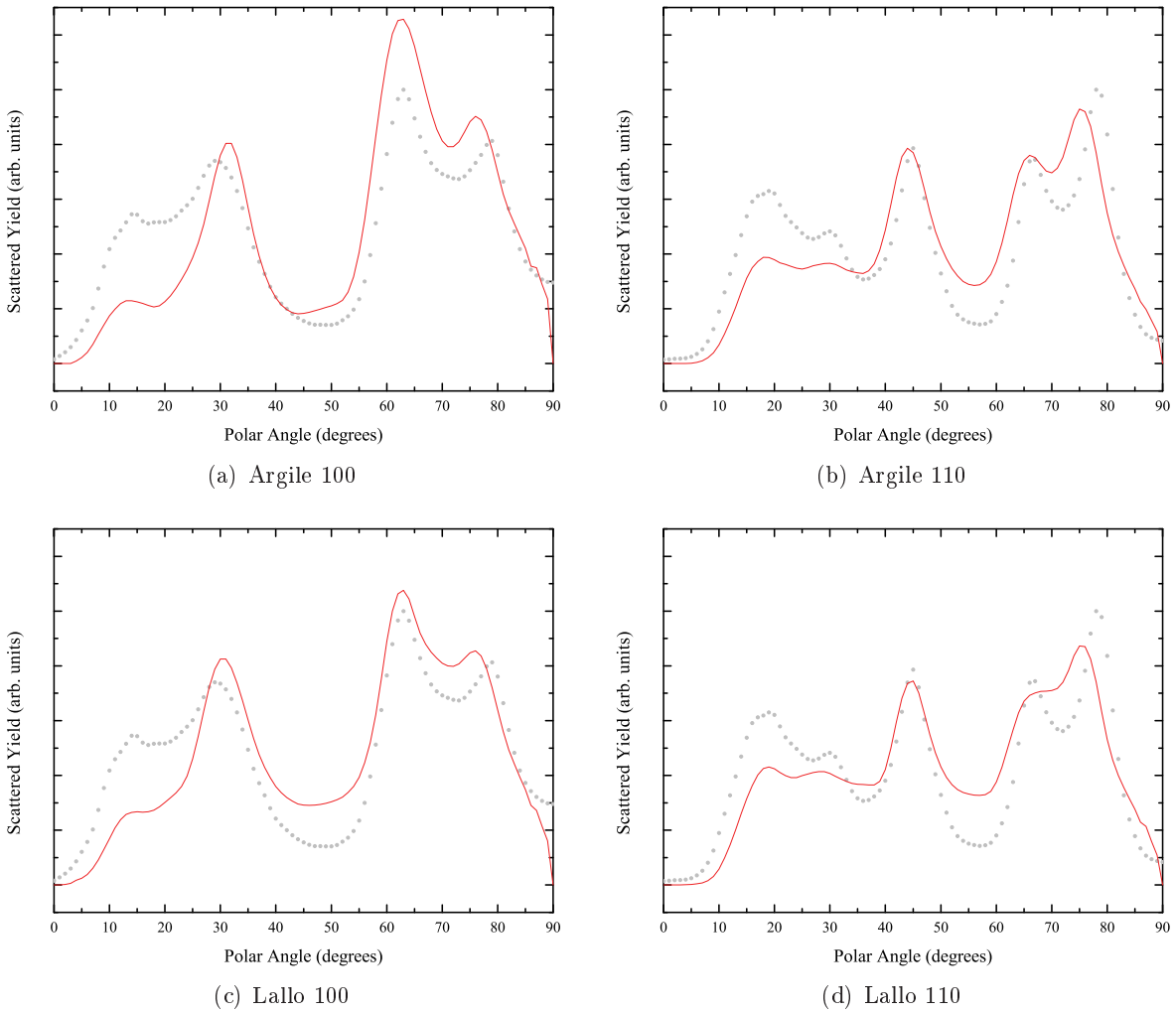

(a) Argile 100 (b) Argile 110

(c) Lallo 100 (d) Lallo 110

Figure 10.5 Optimised CAICISS Cu backscattering fits from SOAR for Phase 4. Experimental data are shown as scatter points, and VEGAS simulations as solid lines.

angle peak discrepancy. Further discussion of this problem and some ideas for steps which can be taken to resolve it are presented in Chapter 12. For now, the large error estimates and make it difficult to draw any solid conclusions from CAICISS analysis of Phase 4.

10.1.3 CAICISS Sn backscattering

If Lallo et al. are correct in their description of Phase 4, then the CAICISS Sn backscattering spectrum should display two peaks for Sn — one arising from scattering within the outermost layer and another at high polar angle arising from lower-level scattering. Figure 10.6 shows the Sn backscattering spectra. The Lallo model displays a clear double surface peak, which arises from the inequivalent Sn atoms in the model — Sn atoms are found in clusters and in multiple layers. In contrast, the Argile and Rhead model displays a very narrow surface peak because all Sn atoms are at the same relaxation above the Cu surface. The Lallo model seems to present a better fit to the broad surface peak of the experimental data. The double

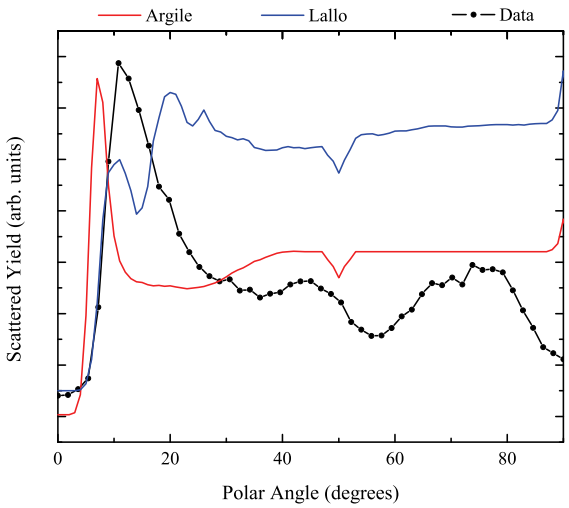

Figure 10.6 Comparison of Phase 4 Sn CAICISS backscattered experimental spectrum with computer simulations from proposed models.

surface peak may be unresolved in the experimental data due to the limited angular resolution of CAICISS scans. The conclusion of Sn backscattering analysis appears to be that the Lallo model provides the best fit for Phase 4.

10.2 Conclusions

The basic structure of each model is very similar, so it is not surprising that the R-factors obtained are also similar. MEIS R-factor analysis seems to favour the Argile and Rhead model; CAICISS R-factor analysis is inconclusive. STM images collected by Lallo et al. [81] seem to support their model, but because of the similarity of the structures proposed by the two previous studies, it is feasible that the images may also be explained by introducing additional rumpling into the Argile and Rhead model, thus creating the two inequivalent Sn atom relaxations proposed by Lallo. In this case, the models reduce to virtually the same structure. The parameters values returned from SOAR fitting of MEIS data are generally reasonable, and the similarity of values between the two models once again highlights just how similar the structures are.

CAICISS Cu data analysis was less conclusive in this case. Both models agree with MEIS analysis within the error estimates returned, but the errors estimates seem to be vastly inflated. Visual inspection of the CAICISS fits shows some large discrepancies between experimental data and both models, which offers some explanation as to why the error estimates are so large. Examination of the CAICISS Sn backscattering signal was able to show a difference between the two models. The Lallo model appears to reproduce the Sn surface peak slightly better, although the fit of the Argile and Rhead model may be improved with introduction

of a larger surface rumpling amplitude which would widen the Sn surface peak observed in Figure 10.6.

The lateral shift of surface Sn atoms (Γ_1) returned by SOAR fitting does not agree with previous studies. Lallo et al. proposed that the expansion was outward from a common centre, with a magnitude 0.18 ± 0.07 Å. Both MEIS and CAICISS analysis return a value in excess of 0.5 Å, although the very large error estimate from CAICISS analysis means that there is a small chance that this study does agree with the results of Lallo.

It seems that none of the analyses conducted are able to conclusively produce a single candidate for Phase 4. MEIS and CAICISS Cu scattering analysis is hampered by the very similar nature of the two models. CAICISS Sn scattering analysis shows some additional differences, but given the large magnitude of the error estimates for the structural fits, the result is far from reliable.

CHAPTER 11

Cu(100)/Sn System Summary

The Cu(100)/Sn system is a complex bi-metallic system that displays a number of different surface reconstructions dependent on Sn coverage [77, 78, 81, 82]. In this study, the various reconstructions of the Cu(100)/Sn system have been examined with ion scattering techniques. Four of the reconstructions, Phase 1, Phase 2, Phase 3, and Phase 4 were reproduced (verified by LEED and AES) and MEIS and CAICISS data collected. A fifth intermediate reconstruction located between Phase 2 and Phase 3 was unable to be accurately reproduced, although a complex LEED pattern was observed similar to that reported in previous studies [80].

Computer simulations were conducted, then compared to the data collected and to previous studies in order to identify the best structural model for each phase. The complexity of the surface reconstructions means that the exact structures of many of the phases has proven to be difficult to determine, with some phases still having multiple candidate models after elimination of those models which do not fit the data. The phases known as Phase 1, Phase 2, and Phase 3 are all found to be best described by surface alloy models. It is therefore tempting to conclude Phase 2.5 should also be based on an alloy model; analysis wasn't able to arrive at a conclusive structure for this phase. Phase 4 is also best described by an overlayer model.

Phase 1 is best described as a $p(2 \times 2)$-based superlattice with anti-phase domains [78]. Analysis of ion scattering data for Phase 2 showed that all overlayer models can be discounted, leaving only a small number of alloy models for further consideration. Analysis of CAICISS Sn backscattering data narrowed this to a single model — an alloy structure with stress relieved through the introduction of regular vacancies within the second layer. Two competing models for Phase 3 are difficult to distinguish, but the best structure appears to contain missing Cu rows in the outermost layer [79]. Analysis of Phase 4 showed that the 'complete overlayer' model of Argile and Rhead [77] seems to fit the collected MEIS and CAICISS Cu scattering data better when examined by the more objective R-factor analysis. But, that observation disagrees with recent STM images collected by Lallo [81], and with the analysis of CAICISS Sn scattering data, which shows evidence that the Lallo overlayer model provides a better fit for the surface layer Sn periodicity. The Lallo model contains a combination of overlayer

and second layer alloying. The LEED pattern observed by Martìnez-Blanco et al. for the intermediate phase was unable to be reproduced. Some data were collected from a similar surface, but were of dubious quality. In order to characterise this phase it is essential that the original LEED pattern be reproduced, and new data be acquired.

During the course of this study details of a new investigation of the Cu(100)/Sn system have been published by Yaji et al. [83], who present additional STM images which corroborate those of Lallo and cast further doubt on the validity of the Argile and Rhead model. A further reconstruction is proposed with a coverage of approximately 2 ML not yet seen in any other study. The new 'Phase 5' is thought to possess a complex $\begin{pmatrix} 4 & 3 \\ -3 & 4 \end{pmatrix}$ structure, and have domains separated by areas of disorder. It is said by the authors that Phase 5 can be considered as an initial growth structure of a bulk β-Sn crystal. No data were collected in this study at Sn coverages above that of Phase 4. The study of Yaji presents a good case that there are most likely no further single layer reconstructions to be seen beyond Phase 4. Another recently published paper by Fuhr et al. [94] (with contribution from Martínez-Blanco) focuses on a Density Functional Theory (DFT) and STM study of Phase 3. It shows good supporting evidence that creation of Cu vacancies in the top surface layer produces a significant energy reduction. Therefore, their conclusion also is that the Pussi missing row alloy model provides the best candidate for the phase. They also find that a two missing row structure can occasionally be observed, and propose a new model which incorporates this feature.

The quality and reliability of CAICISS data and simulations has been constantly called into question during this study. There seems to be problems with the equipment that result in inconsistent beam properties. With a scan taking upwards of 3 hours, any variation in the beam during this time has a large effect on the data. The CAICISS simulation codes currently in use do not seem to accurately reproduce the intensities seen in the experimental spectra, and as a result application of the MEIS R-factor to CAICISS analysis produces vastly overestimated error estimates.

It is vital that these issues be addressed if conclusions drawn from CAICISS analysis are to be trusted. With the CAICISS apparatus being in-house there is obviously opportunity for alterations to be made to enhance the reliability and resolution of data acquisition. In the next chapter are details of a number of changes made to the CAICISS apparatus in response to the shortcomings found during this study. Equipment has been replaced, software rewritten and analysis procedures revised, in order to make CAICISS a more reliable and powerful surface analysis technique.

Part III
Interaction Potentials

List of Chapters

CHAPTER 12

Warwick CAICISS: Modifications and Improvements

The Warwick CAICISS system entered its second decade in 2005. During the first ten years since its construction there have been minor changes, but no systematic attempt had been made to identify and address the limitations of the design, or to carry out anything but the most essential maintenance in order to keep the equipment operational. This chapter identifies some shortcomings of the Warwick CAICISS apparatus and analysis process, and then describes changes made in order to improve the system*. The key areas of the CAICISS apparatus which will be examined are: Pumping, ion beam production, and data acquisition. Improvements made to the procedures for data analysis and interpretation are then discussed. The final section of this chapter outlines some future works which may yield further improvement, and discusses work in progress on a new sample transfer and deposition chamber.

12.1 CAICISS apparatus

12.1.1 Pumping

The arrangement of UHV and roughing pumps as they were in 2005 [3], including the locations of valves and vent points, is somewhat different from the original design [34]. The system as inherited is in a state where the pumping is simply not adequate. A number of issues were identified as needing attention.

The main chamber ion pump was in need of refurbishment and has been removed. In its place was installed a 340 ls^{-1} turbo molecular pump (Leybold, 340M). Installation of the turbo pump provides cleaner (oil-free) standby operation of the system. Pumping to the ion source chamber has been improved (see Figure 12.1). The discharge chamber of the Nielsen Ion Source was pumped only through the anti-cathode aperture and a 'mini-conflat' flange with small bore, leading to very poor pumping speed, and a tendency for the anti-cathode to pop out of its housing when venting to atmosphere. Consequently there was a lot of contamination in the source, and therefore in the ion beam also. The He gas reservoir was found to be leaky.

* The system 'as-was' has been described numerous times by other authors [3, 14, 34].

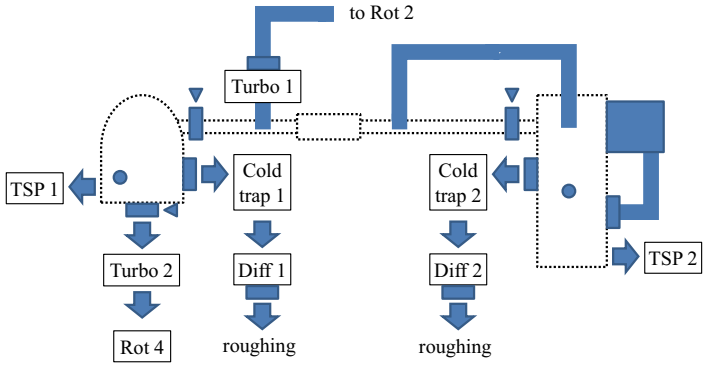

(a) Chamber, Ion Column and UHV pump arrangement.

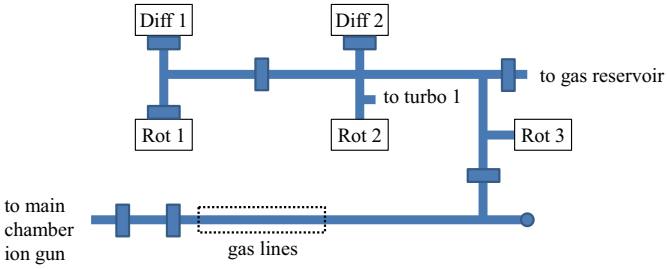

(b) Roughing pump arrangement.

Figure 12.1 CAICISS pumping arrangement after system improvements.

In addition to fixing the leaks, the reservoir has been enlarged, and is now capable of holding three times the volume of gas; it now provides for a more consistent and pure ion beam. Roughing — previously carried out through the column — has now been moved to the main body of the ion source chamber. A titanium sublimation pump (TSP) has been attached and set to fire regularly. The vacuum base pressure has improved by an order of magnitude to 2×10^{-9} mbar.

Flight-tube and column pumping has also been improved by the addition of a small 50 ls^{-1} turbo pump (Pfeiffer, TPU050), and a pumping bypass. The flight tube was previously pumped only through the chopping aperture (0.5 mm diameter) unless open to the main chamber, causing main chamber contamination during data runs. The roughing pump arrangement has been improved to make it independent of diffusion pump backing (see Figure 12.1).

A new heater-tape system has been put in place for improved bakeout temperature. The bake is now hotter all over, at the expense of creating some hot spots. A new bakeout controller was designed (and constructed by the in-house electronics workshop) to provide up to 3 kW of heating power. A separate low temperature heater tape is in place for the Nielsen ion source, which cannot be baked to full temperature because of plastic components. The base pressure of the main chamber has improved from 8×10^{-10} mbar to 1×10^{-10} mbar.

12.1.2 Ion beam production

The original specification for the ion source (designed and constructed by Prof. Mark Dowsett of Warwick University) suggested that it should be capable of more beam production than than observed[†]. Experiments in the early days of Warwick CAICISS took anything up to 26 hours to perform, because of the poor beam intensity, and low signal to noise ratio. By 2005 this had been reduced to 3 hours, but maintaining a consistent surface given the poor base pressure of the main chamber at the time was problematic.

The source had not been fully cleaned in over 3 years. In response, it has been cleaned, including a complete disassembly of the ion source discharge chamber and filament housing. Poor pumping to the discharge chamber had left a lot of deposits on the anode and other components. All components were cleaned using an ultrasonic bath — components were immersed in a solution of iso-propyl alcohol (IPA) and alumina paste for a number of hours until deposits had been removed. In the case of the anode, the deposits were so thick that the only solution was to remove them using abrasives, after which the same ultrasonic procedure was followed. All components were rinsed once more in IPA before being reassembled.

During reassembly, modifications were made to the filament housing in an attempt to increase the electron density in the discharge chamber and improve plasma production. The filament was reshaped and filament rods extended to move the filament further into the discharge chamber. The can was previously surrounding the filament, and therefore acting as a weak Wehnelt cylinder. By extending the filament beyond the end of the can, electrons are able to more freely move into the discharge chamber. Figure 12.2 shows a cross-section of the ion source with all components labelled.

A bad weld in the source meant that the required positioning and alignment of the source lens changes with energy, leading to a very small range of energies that would provide a usable beam flux at the sample. On the other hand, it provides a bend in the column to separate ions and neutrals in the beam. A method was needed of steering the beam before it reached the bad weld, so a set of quadrupole plates was added to the end of the lens assembly, to increase the range of beam energies that could be successfully steered down the column. Although a set of quadrupole plates does not in itself provide two-dimensional steering capability, the effect of the plates was found to be sufficient to achieve an improvement in the beam intensity. The new quadrupole system required new steering electronics to be developed, including outputs

[†] The source is a modified Nielsen ion source, typical examples of which are capable of producing a beam current the order of 50 μA [95]

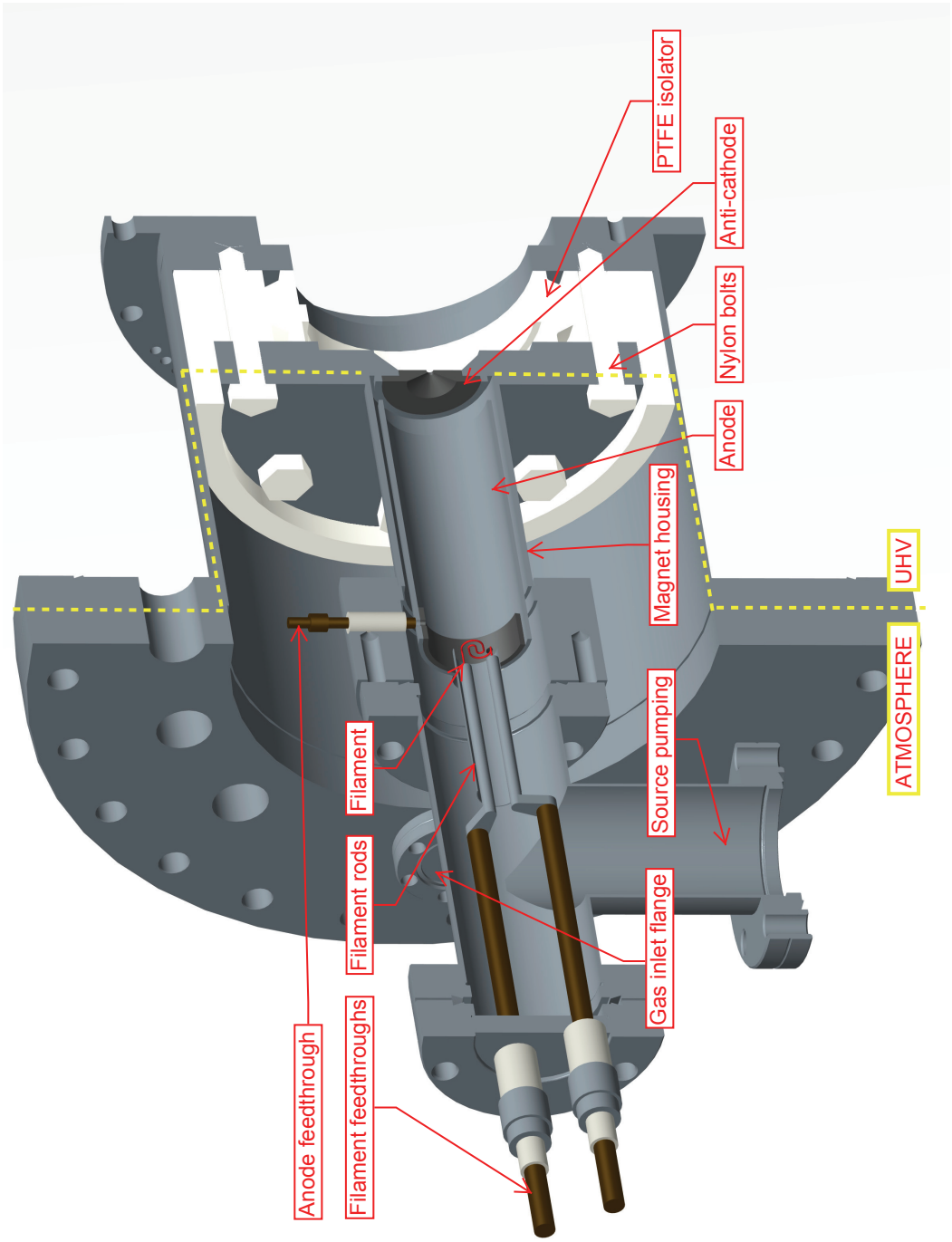

Figure 12.2 Cross-section of the Warwick CAICISS ion source, with major components labelled.

for driving the existing steering plates. The new steering electronics were designed with future improvements in mind; specifically they are capable of driving a quadrupole triplet lens system without needing any modification. With additional steering, the beam energy range of the CAICISS apparatus is now 1 keV to 5 keV.

The source immersion lens was repositioned with respect to the anti-cathode in order to reduce its strength (moved from a distance of 5 mm to 10 mm). The adjustment of the lens voltage is now far less sensitive, allowing for more accurate control of the beam focal point — very important to the beam intensity at the sample. To get more beam to the sample the focal point of the lens needs to be closer to the sample. To this end, the apertures in the column have been rearranged to allow a wider beam into the first steering section, so that the focal point can be extended down the column. The optical bench on which the lens assembly sits was also realigned to ensure that the lens system is coaxial to the source discharge chamber and anti-cathode. Figure 12.3 shows a labelled cross-section of the rearranged focusing system, including the new quadrupole plates.

The steering and focusing systems in the column were inadequate. In order to maintain a coaxial beam, sets of steering plates must be installed in multiples. Figure 12.4 shows a schematic of the requirements for accurate ion beam steering (in one-dimension). Top: a single set of steering plates (green), is able to navigate the ion beam (red) through the aperture, but cannot maintain a co-axial beam. Middle: Adding a second set of plates after the aperture

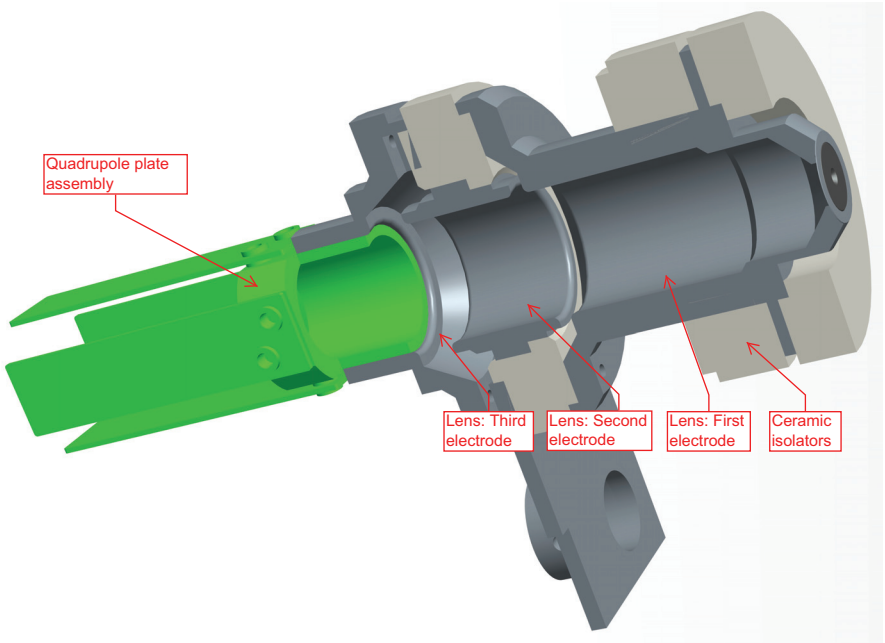

Figure 12.3 The CAICISS lens assembly, with newly attached quadrupole plates (in green).

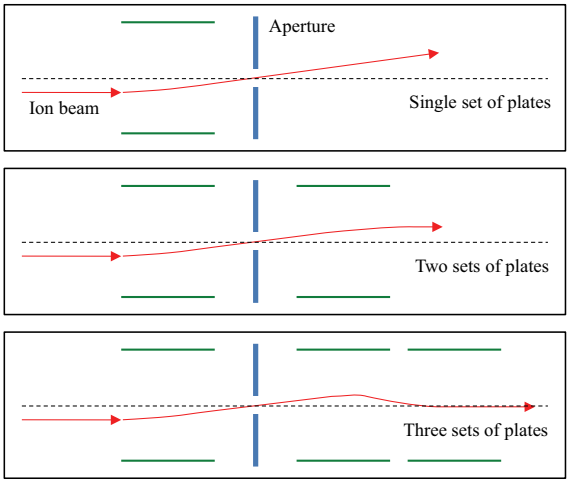

Figure 12.4 Schematic showing the required arrangement of steering plates in order to maintain a co-axial ion beam in one-dimension. A single set of plates is insufficient; three sets is the ideal.

allows the beam direction to be restored. Bottom: Adding a third set allows for complete control of ion beam direction and position. In addition, the lens system of the ion source creates a divergent beam, which cannot be corrected by steering alone.

Previously, typical maximum beam current on the chopping aperture was around 80 nA. Following the improvements to beam production outlined above, the current at the same beam energy was found to be around 250 nA. A new current monitor plate was also added before the steering section so that the total output from the source could be monitored. The plate is mounted on a z-shifter so it can be inserted into the path of the beam as required; it showed that the source is now producing around 5 μA beam current — still well below what the source should be capable of producing, but sufficient for CAICISS studies.

The chopping arrangement did not supply sufficient voltage to the steering plates to sweep the ion beam the entire way across the chopping aperture, leading to a small proportion of beam traversing the column continuously — introducing useless background counts to the received signal. An amplifier capable of providing higher plate voltages was installed to ensure that the beam sweeps fully across the chopping aperture. Some modification will be required to this amplifier in future to allow the chopping voltage to be fine-tuned. There is a trade-off between time resolution (improved by short pulses of ions) and the amount of signal (improved by longer pulses of ions). The 300 V sweep that the amplifier provides at present means that pulses for beams with energy below 2 keV contain very few ions. Still, the capability to perform CAICISS scans of a consistent quality in a continuous energy range between 2 keV and 5 keV is a marked improvement.

12.1.3 Data acquisition

Despite having plenty of beam current, collection of the CAICISS signal was still causing problems due to electronic noise and poor calibration. In order to reduce electronic noise, wiring in the racks has been tidied, and timing electronics simplified. All timing is now driven by a single signal generator. Most of the load previously was from driving the chopping plates, which is now handled by a separate amplifier. All non-essential wiring has been removed and what remains has been shortened to decrease the capacitive load. The acquisition electronics were re-calibrated to ensure maximum signal collection.

Previously, finding the crystal in the chamber could be problematic. Because of variations in beam alignment, the optimum sample stage position changes daily. The ToF system can make it difficult to distinguish between surfaces in the vacuum. Perfect alignment could take up to several hours and needed to be repeated whenever the azimuthal angle or beam energy are altered. To help with sample alignment, the reverse of the manipulator head has been modified to provide a focal point for the beam. A small metal plate has been attached and wired to a feed through for external monitoring of current. By optimising the current on the plate the beam can be accurately located in the main chamber in a matter of minutes. The plate is placed directly behind the sample centre, so once the beam is focused, the polar angle can be rotated through 180° and the beam will be incident on the sample centre.

All the apparatus changes discussed have resulted in a reduced time for a CAICISS data run. A low-count test scan can now be completed in less than 15 minutes (8 minutes is possible if the beam current is pushed close to maximum, although this results in drastically reduced source filament lifetime). A full run takes approximately 1 hour, compared to a runtime of around 3 hours previously. There are yet more improvements that can be made in the future, some of which are discussed later in this chapter.

12.2 Software and data interpretation

12.2.1 Data analysis

The basic procedure for analysis of CAICISS data remains the same as outlined in Chapter 4. Presentation of the two-dimensional datasets has has been made more similar to the format received from MEIS scans — a false colour scale is used to represent counts. It is felt that this helps to draw parallels between the two techniques, and highlight that scattered ion energy is essentially equivalent to time-of-flight. Figure 12.5 shows an example of both formats. A big addition to the analysis procedure is the introduction of automated structural optimisation.

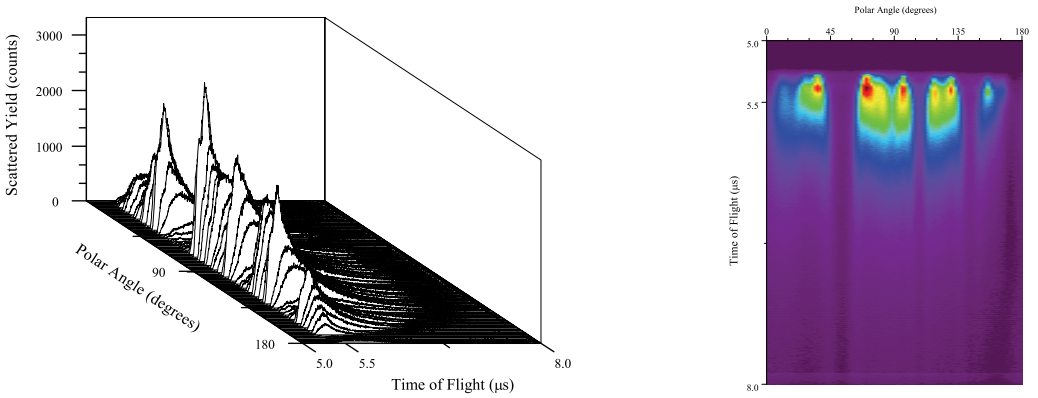

(a) Three-dimensional plot showing a compilation of all single time-of-flight spectra.

(b) Showing counts on a false colour scale.

Figure 12.5 CAICISS unprocessed data presentation formats. The same dataset has been plotted in both views.

12.2.2 Structural optimisation automation routine (SOAR)

SOAR is an attempt to fit crystal surface structures using parameters that alter simulation atom positions automatically. Similar codes exist for MEIS already, but until now there has been no CAICISS equivalent. No objective measure of the quality of fit between an experimental dataset and simulation — an R-factor — was applied for CAICISS. All structural optimisation was carried out by manually altering crystal atom positions and re-running simulations until the fit 'looked' correct.

The pre-existing MEIS codes cannot be made to work for CAICISS without modification — the simulation packages are too different. Fortunately, the MEIS codes are based on the separately available IFFCO codes [54], with which there was definite potential for integration. The first version of the CAICISS SOAR codes was written and used for the Cu(100)/Sn study already presented, and the first of the crystal surfaces (Pt) in the interaction potentials investigation (presented in Chapter 13).

In most cases, errors for structural parameters are vastly over-estimated with version one of SOAR. The clean surface Pt(111) data is an exception to this — the CAICISS spectra from this particular crystal contain notably sharp peaks. Reasons for this are unclear. Similar results were seen by Walker [3] with the same Pt sample — the crystal was easy to clean and provided very good quality data — so the variation may be down mainly to crystal quality. The majority of crystals provide less sharp peaks, thus errors are inflated in most cases.

A second version of the SOAR codes was developed and used for analysis of the remainder of the interaction potentials investigation. Version one R-factors were not always directly comparable between crystals because there was no normalisation in the CAICISS datasets.

Fortunately, all datasets presented for the Cu(100)/Sn system were collected at an energy of 3 keV, negating the need for normalisation. Version two introduces a normalisation to the datasets so that R-factors can be compared between different crystals more effectively. An attempt was also made tackle some of the limitations imposed by the FAN simulation codes — a single unit cell can now be specified, and SOAR will build a larger crystal for use by FAN, a process that had to be done manually up until now. Changes were also made to the error calculation procedure in an attempt to account for the problems of applying an R-factor — developed primarily for MEIS data — to CAICISS datasets. There is further discussion of these changes during the interaction potentials investigation in Chapter 13.

12.3 Future work

Good progress has been made on improving the Warwick CAICISS system. Even so, there are many more works that can be carried out. This section will outline some of the more important possibilities, and then present the work conducted so far on the construction of a new sample transfer system which will be attached to the CAICISS system and become functional in early 2010.

Pumping to the system could be improved by restoring the functionality of the titanium sublimation pump in the main chamber. Only the lack of a suitable electronic control unit is preventing this at present. The combination of TSP with diffusion pump should help to keep the scattering chamber clean enough that the duration of experiments becomes unimportant. Ultimately, it would be preferable to replace the ageing diffusion pumps with cleaner — and safer — alternatives, such as turbo molecular pumps, to avoid lengthy downtimes caused by power failures or backing pump malfunctions in the past. The ion pump should be refurbished and reattached.

Ion source bakeout temperature is still a potential issue. The nylon studs that attach the source to the chamber — whilst still retaining electrical isolation — should be replaced with Polyether ether ketone (PEEK) studs, which can be subjected to a full temperature bake without becoming brittle and risking failure. That should mean less water vapour, and therefore less deposits in the source. Still, even with a cleaner vacuum, regular cleaning of the source is a necessity to maintain optimum beam intensity and stability.

The amount of beam reaching the sample needs to be optimised. In the short-term, an increased range of energies should be obtainable by making the chopping voltage variable — the pulse length can then be adjusted for any ion beam energy. The source cooling could be

improved to allow for more beam production in the first instance. But, in the longer term, the biggest improvement in beam intensity will be seen when the column steering arrangement is completely overhauled. Additional steering plates are required in order to maintain a well-focused coaxial ion beam. With a full re-design the CAICISS beam production can be made much more compact and efficient.

Just some of the possible improvements to CAICISS data acquisition include: increasing stepper-motor resolution, motorisation of other manipulator axes, and full computer control. If beam production is to be increased, then there will be a necessity to upgrade the computer hardware so that it is able to process a larger count rate. With run times already down as low as 8 minutes in some cases, it seems reasonable to aim to reduce this further by implementing system improvements. If the run-time can be reduced by an order of magnitude again — so that runtime is of the order of 1 minute — then the powerful combination of *in situ* MBE and CAICISS angular scans becomes a real possibility.

The newly developed SOAR codes have greatly sped up the analysis procedure, but are not without problems. A better R-factor measure is needed for CAICISS — one that takes better account account of the small percentage change in CAICISS spectra between different structures. The MEIS R-factor as it stands provides adequate results, but overestimates error if no correction is applied. The source code for the FAN simulation package is not available, which has hindered efforts to produce a more integrated solution. Ideally, a new simulation package should be created that is based on the same principle, but more customised to the specific requirements of CAICISS, and capable of running in a parallel-computing environment to reduce simulation times.

12.3.1 New sample transfer system

Changing a sample currently involves venting the main chamber. Turnaround is extremely slow given the speed of the technique once the sample is prepared. The new sample transfer system — designed in early 2009 (by the author) and shown in Figure 12.6 — will double as a preparation and deposition chamber. It will be pumped by a turbo-molecular pump, and have sample heating capabilities. By conducting sample degassing in this secondary chamber, the main chamber vacuum can be kept clean. Multiple deposition sources will be attached to the secondary chamber to allow surface preparation without main chamber contamination if desired. Sample turnaround time will be reduced from five days to several hours. Possible future work could include an intermediate storage chamber, which would allow for the storage

of multiple samples under vacuum. The Daresbury MEIS facility already has such a system, used to great effect.

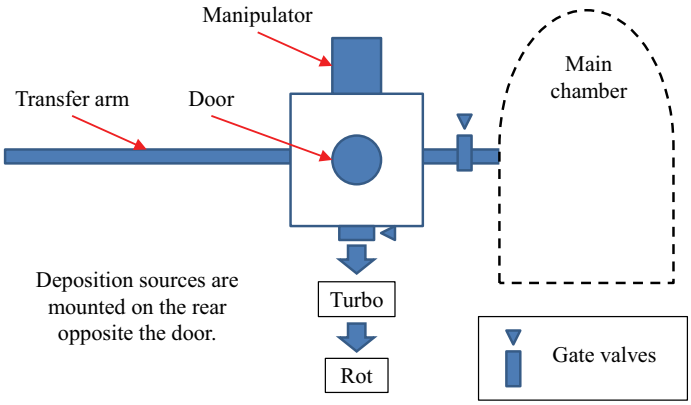

Figure 12.6 Schematic of the proposed design of the new sample transfer and deposition chamber.

12.4 Conclusion

Details have been presented of a number of improvements made to the Warwick CAICISS system, which have resulted in increased vacuum quality, and production of a higher intensity ion beam for experimental studies. CAICISS run times have reduced accordingly, with collection of a 180° polar angle scan now taking 1 hour rather than 3 hours. Data analysis processes have also been examined and improved, and new computer codes written to provide automated fitting capability for both MEIS and CAICISS. Some possible future work has been identified, and details of a near-completed sample transfer system presented.

CHAPTER 13

CAICISS Screening Length Correction Factors

Structural fitting of CAICISS data requires a detailed understanding of the ion-surface interaction. In order to accurately simulate trial structures, it is vitally important that the correct interaction potential is chosen. There are two commonly applied screened Coulomb potentials for LEIS techniques — the Molière approximation to the Thomas-Fermi model (TFM) [20,21], and the 'universal' Ziegler-Biersack-Littmark (ZBL) [8]. The TFM potential* has been used throughout this study for simulation of both MEIS and CAICISS; it is described in more detail in Chapter 3.

Previous CAICISS studies [3] have shown that use of the ZBL potential is unable to accurately reproduce low energy ion beam results even for a simple low-index clean metal surface such as Cu(100). This is believed to be due to an overestimated strength of repulsion at large impact parameter values (i.e. in the backscattering regime required for CAICISS) [96]. The TFM potential can be applied to CAICISS data, but a correction is required to the screening length to allow for the long ion-surface interaction time resulting from the use of very low beam energies (1 keV to 4 keV). The correction modifies the Firsov screening length [22] by a constant factor determined by the particular incident ion and target atom combination. Work by O'Connor [24] provided a commonly accepted set of correction factor values for LEIS studies. Some recent CAICISS studies [3, 43, 90] have shown significant deviations from the O'Connor correction factor values (Ni: 0.60 compared to the O'Connor value of 0.84, Cu: 0.53 compared to 0.85, Pt: 0.78 compared to 1.00). In all cases there is a general consensus that the values of O'Connor are too high when applied to CAICISS data. Other authors have noted similar deviations when working with different surface science techniques. A range of published values exist for the He–Cu ion-surface interaction [97–99], all of which exhibit correction factors below the O'Connor values.

As a result of the discrepancies found, CAICISS studies have been undertaken on a series of low-index clean metal surfaces with well-known surface relaxations. The aim of these

* The TFM potential is a repulsive Coulomb potential with an electron screening correction function.

studies is to investigate the mass and energy dependence on the correction factor for CAICISS experiments. Modifying the screening length via changes to the correction factor alters the width of shadow cones, causing the location and relative amplitudes of CAICISS spectrum features to shift. By constraining structural parameters near to commonly accepted values it is possible to optimise the correction factor value which should be used for each ion beam to target atom combination. Results of studies of five clean metal surfaces are presented here — Cu(100), Ni(110), Pt(111), Au(111) and Pd(111) — in the beam energy range 1.5 keV to 4 keV.

Experimental details

Clean surfaces were prepared with multiple cycles of 1.5 keV Ar^+ ion bombardment followed by high temperature annealing. Different annealing temperatures were used for each crystal, in accordance with established cleaning procedures [85], as shown in Table 13.1. LEED was checked for a (1×1) pattern between each cycle, and AES showed all surfaces to be free of contamination before CAICISS data acquisition.

CAICISS raw data were processed according to the procedures outlined in Chapter 4. For each surface, an initial estimate of the screening length correction factor (C_f) can be made from the angular position of the surface peak. This analysis requires no simulation, but is limited in accuracy because it examines the position of only a single peak. Even so, it is a worthwhile stage in analysis; the surface peak is arguably the most important feature in determination of correction factor. Fauster's expression [27] relates surface layer inter-atomic spacing to surface peak polar angle for the TFM potential (Equation 3.8); it can be rearranged to give an estimate of C_f, so long as one makes the assumption that the inter-atomic spacing (d) is known, as is the case here for a series of much-studied clean metals. Care should be taken interpreting these initial estimates; they rely on the assumption that the outermost surface layer is planar. In reality there may be surface rumpling which alters the shape and position of the surface peak. In order to determine the correction factor with any real accuracy it is

Table 13.1 Approximate anneal temperatures for each crystal.

Crystal	Anneal Temp. (K)
Ni(110)	900 ± 25
Cu(100)	1050 ± 25
Pd(111)	1050 ± 25
Pt(111)	950 ± 25
Au(111)	950 ± 25

necessary to conduct a full fitting of the near-surface layers through comparisons with computer simulations. Experimental spectra were simulated using the FAN codes (Niehus) [16], and structural optimisation was conducted via SOAR. Development and usage of SOAR is detailed in Chapter 4.

13.1 Copper (Cu)

Clean copper surfaces have been the subject of many studies [39, 41, 100–106], including previous CAICISS studies [90]. It is important to establish that a physically sensible structural solution can be arrived at using the newly developed SOAR codes. The wealth of previous studies means that there are plenty of proposed structures — from a large range of surface techniques — for results to be compared to. A number of previous studies have been compiled into a single review by Rodriguez [4], providing a good primary source of comparison for new investigations.

The surface was prepared *in situ* with cycles of IBA (as described above); a sharp (1×1) LEED pattern was obtained at 74 eV after cleaning. AES scans showed no contamination of C, O, S or Ar.

Previous CAICISS Cu(100) studies [90] have focused on a single incident beam energy of 3 keV, the analysis of which concluded that the best correction factor for fitting experimental data was 0.53. In this new study, data from four different beam energies are presented (1.5 keV, 2.0 keV, 2.5 keV and 3.0 keV). Analysing each dataset independently not only provides a method of testing the dependence of correction factor on beam energy, but is also a means to test the structural solving capabilities of SOAR, to see if multiple datasets from the same surface converge on a single physical solution as one would expect.

Results

Data were collected from the Cu(100) surface at the four incident beam energies detailed above, in two azimuths — $\langle 100 \rangle$ and $\langle 110 \rangle$. Figure 13.1 shows the raw data collected. In all cases, there are some residual counts below the critical surface peak polar angle due to the ion beam impacting the side of the sample. Once the surface peak is reached the entire beam is on the sample face. There are some obvious trends in the datasets as incident ion energy in increased. Peaks become better resolved — particularly those originating from deeper within the surface — and the surface peak moves to lower polar angle. These changes are attributable to the narrowing width of shadow cones with increasing energy. The origins of each of the

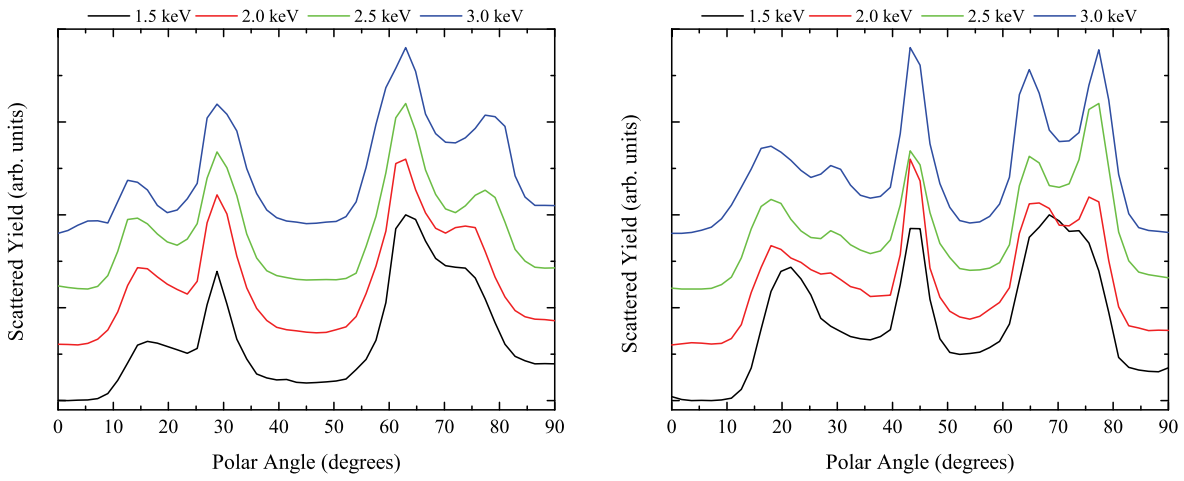

(a) ⟨100⟩ azimuthal data (b) ⟨110⟩ azimuthal data

Figure 13.1 Raw data collected for clean Cu(100) in two azimuths. Data have been vertically translated for clarity.

features in these spectra have already been discussed in a previous study (see Part II on the Cu(100)/Sn system).

As discussed above, some limited estimates of correction factor can be made directly from the raw data using Fauster's expression (Equation 3.8). Previous experimental studies [3] have shown that the surface peak should be measured at a position around 80 % of the full peak height. The exact reasons for this are unclear, but it is believed to be partly due to experimental broadening and multiple-scattering events [14]. Figure 13.2 shows the theoretical correction factor variation† as a function of surface peak position for each of the primary beam energies in the ⟨100⟩ azimuth. Several lines are marked on the plot. The dotted line corresponds to the commonly accepted O'Connor correction factor value (from Equation 3.6). The solid lines are estimates calculated from the surface peak position in each of the Cu datasets.

These estimates have errors which are difficult to quantify, but one can conclude that, in order to match experimental data, it seems to be necessary to apply a significantly lower correction factor than that suggested by O'Connor. Experimental datasets suggest a value somewhere between 0.60 and 0.65 should provide a good fit. Further fitting (with computer simulations) of the spectrum as a whole will determine the correction factor for each incident energy with more accuracy.

There is no evidence from LEED images that the clean Cu surface has a different reconstruction to the underlying bulk crystal. Therefore, the key structural parameters for fitting of the clean Cu surface are relaxations in the form of changes to the first and second inter-layer

† The values of correction factor were calculated using Fauster's expression (Equation 3.8) in conjunction with application of a commonly accepted lattice constant for Cu of 3.615 Å.

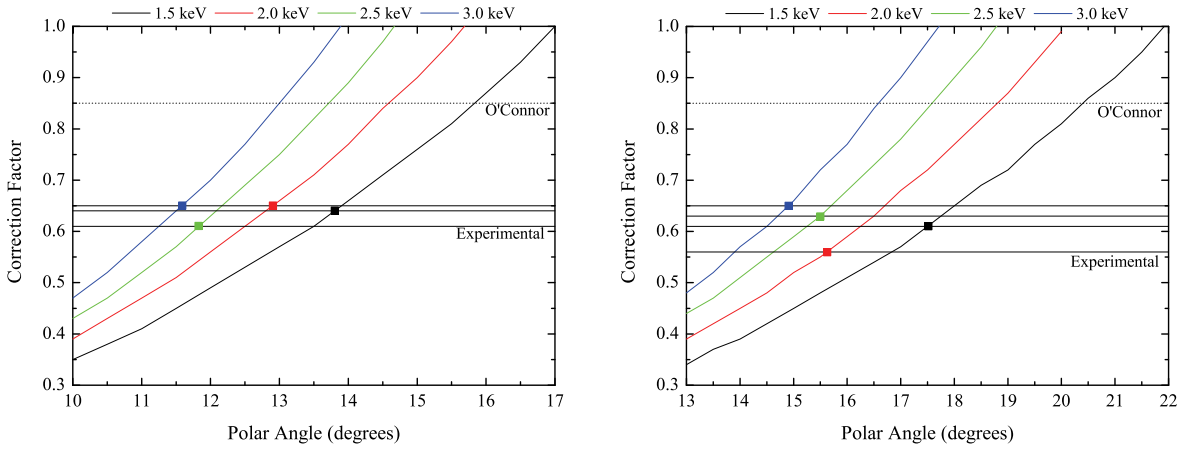

(a) ⟨100⟩ azimuthal data (b) ⟨110⟩ azimuthal data

Figure 13.2 Theoretical correction factor (C_f) variation for each incident beam energy on Cu(100), as a function of the angular position of the surface peak.

spacings (Δ_{12} and Δ_{23} respectively). In this simple case, it is easy to identify parameters such that values correspond directly with the physical structure. A value of zero for each of the identified parameters corresponds to the bulk structure. R-space plots conducted for each structural parameter (not all shown), display simple, single minimum variations. This allows for easy assignment of intervals for input to SOAR, as given in Table 13.2. As already discussed, R-space plots alone are insufficient for providing a final structural solution, but they do provide a useful means of narrowing-down the SOAR parameter intervals to ensure convergence on a physically sensible solution. Figure 13.3 shows an R-space plot of correction factor variation for each dataset. The results seem to agree with the earlier estimates from the raw data, with the optimum correction factor consistently found to be much lower than that suggested by O'Connor (0.85) — between 0.55 and 0.60. Importantly, this plot appears to show very little, if any, dependence of C_f on incident beam energy.

SOAR fitting was conducted on datasets from each incident energy individually, so that any energy dependent factors could be identified. Figure 13.4 shows the final optimised fit for each incident energy. The peak positions match well in all cases. The most important scattering features for surface analysis are those that originate at shallow polar angle ($\lesssim 45°$)

Table 13.2 Approximate SOAR fitting intervals for each parameter determined from analysis of R-space plots.

Parameter		Lower	Upper
Correction Factor	C_f	+0.50	+0.70
First inter-layer spacing change	Δ_{12}	−0.200	+0.100
Second inter-layer spacing change	Δ_{23}	−0.150	+0.150

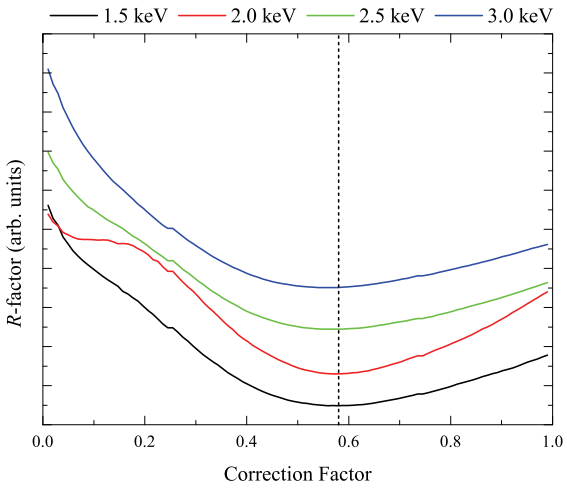

Figure 13.3 Correction factor R-space plot, showing the variation of R-factor with C_f for each incident beam energy for Clean Cu(100).

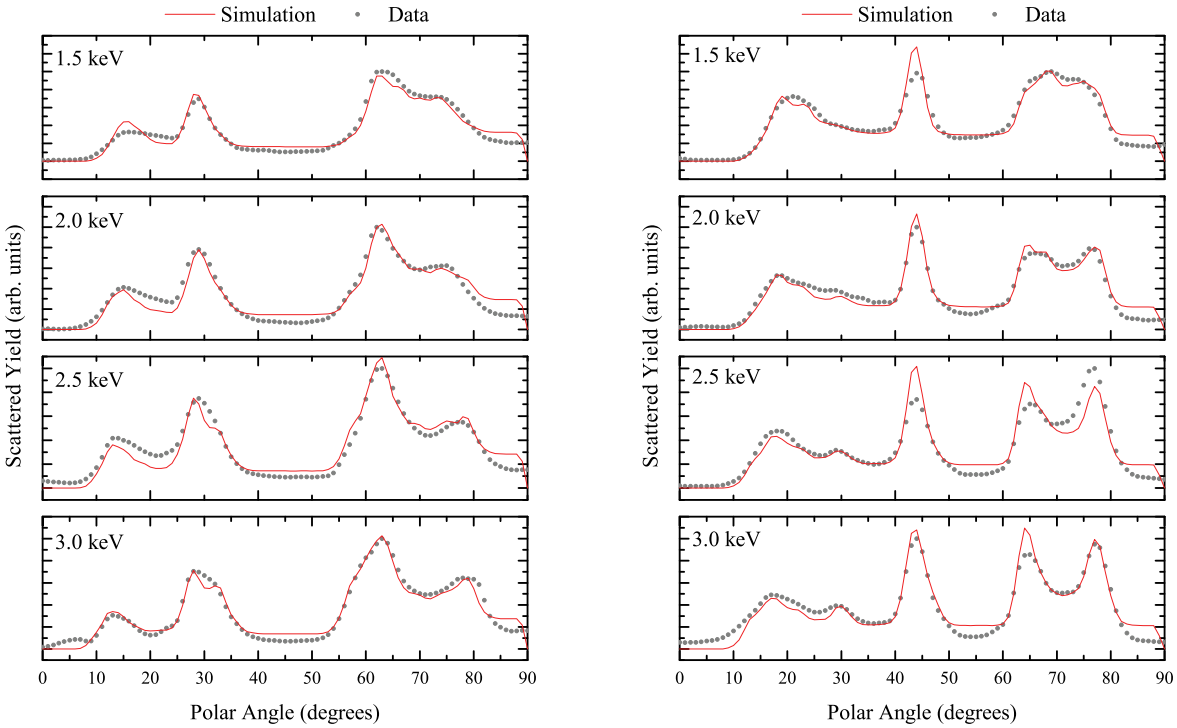

(a) ⟨100⟩ azimuth (b) ⟨110⟩ azimuth

Figure 13.4 SOAR optimised fits for clean Cu(100).

— and are therefore surface specific — all of which are well reproduced by SOAR. Some of the relative intensities of peaks were unable to be reproduced by SOAR within the defined intervals: for example, the peak around 75° polar angle in the 2.5 keV ⟨110⟩ azimuth dataset. Examination of the datasets at higher and lower energies both show a smaller peak in the same position. So, it seems likely in this case that the larger size of the feature is an anomaly caused by fluctuations in beam production. The beam setup when these datasets were collected was

prone to fluctuation, causing large beam intensity changes at the sample. Changes to the CAICISS equipment have resulted in reduced frequency and magnitude of these fluctuations, and are explained in Chapter 12.

Table 13.3 shows the R-factor improvement gained via SOAR, and Table 13.4 shows the structural solution obtained for each dataset. R-factors are reduced by at most 5 % through optimisation. The reasons for this have been discussed in an earlier chapter, but essentially it is due to invariant areas of the spectrum introducing an overhead to the R-factor. In addition, the large invariant areas of the spectrum make the R-space variation of each parameter artificially much more shallow than it would have otherwise been. Because error estimates are calculated from the rate of change of R-space, they are also affected — by being vastly inflated, as shown by column two of Table 13.4. Ideally, a new method of spectrum comparison is needed for CAICISS data which avoids all the pitfalls of the current algorithms, but time did not permit development of any more new code.

More reasonable error estimates can be obtained by correcting for the R-factor overhead. Inspection of R-space variation plots suggests a constant factor should be applied to all parameters. A value of 0.2 produces error estimates for all parameters that still reflect the R-space relation — shown in the third column of Table 13.4. This multiplication factor

Table 13.3 Comparison of bulk and SOAR optimised R-factors.

Energy (keV)	R-factor	
	Bulk	Optimised
1.5	1.51	1.44
2.0	2.42	2.36
2.5	2.22	2.14
3.0	2.56	2.45

Table 13.4 The final parameter values for clean Cu(100), with associated error estimates. Further discussion of error estimates and their adjustment is found in the text.

	Value	Error Est.	Adjusted		Value	Error Est.	Adjusted
Energy: 1.5 keV				Energy: 2.5 keV			
C_f	+0.58	±0.08	±0.02	C_f	+0.57	±0.11	±0.02
Δ_{12}	−0.060	±0.257	±0.051	Δ_{12}	−0.051	±0.260	±0.052
Δ_{23}	+0.042	±0.281	±0.056	Δ_{23}	+0.022	±0.201	±0.040
Energy: 2.0 keV				Energy: 3.0 keV			
C_f	+0.58	±0.10	±0.02	C_f	+0.57	±0.12	±0.02
Δ_{12}	−0.104	±0.244	±0.049	Δ_{12}	−0.070	±0.225	±0.045
Δ_{23}	+0.027	±0.229	±0.046	Δ_{23}	+0.025	±0.206	±0.041

changes how sensitive error estimates are to the R-space gradient change, and generates a new equation for calculation of CAICISS error estimates for each parameter (σ) based on the earlier Equation 4.2, given by:

$$\sigma = 0.2 \sqrt{\frac{2}{\left.\frac{d^2 R_\chi}{dZ^2}\right|_{R=R_{\min}}}} \tag{13.1}$$

Examination of the parameter values output from SOAR reveals that all datasets seem to show the same or similar structure. The averaged correction factor is (0.58 ± 0.01). The first inter-layer spacing is contracted from the bulk Cu value of 1.81 Å by an average of (3.9 ± 1.4) %, and the second inter-layer spacing is expanded by an average of (1.6 ± 1.3) %. These values compare well with previous studies [4], which consistently report expansions and contractions of similar magnitude and direction. Many metal surfaces display the same pattern of 'damped oscillatory relaxations'. Importantly, all datasets show optimum fitting at very similar correction factor values, suggesting that the Cu(100) surface shows no correction factor variation with incident beam energy in the range tested.

The CAICISS correction factor results presented here are clearly at odds with the previous work of O'Connor. Figure 13.5 shows a comparison of the FAN fits obtained for the different correction factor values — CAICISS (0.58) and O'Connor (0.85); the difference is clear. The O'Connor correction factor consistently fails to reproduce the experimental features observed. Particular attention should be paid to the inability of the O'Connor correction factor to reproduce the surface peak. As already established, the location of the surface peak is of paramount importance, and is defined by a combination of the inter-atomic distance in the

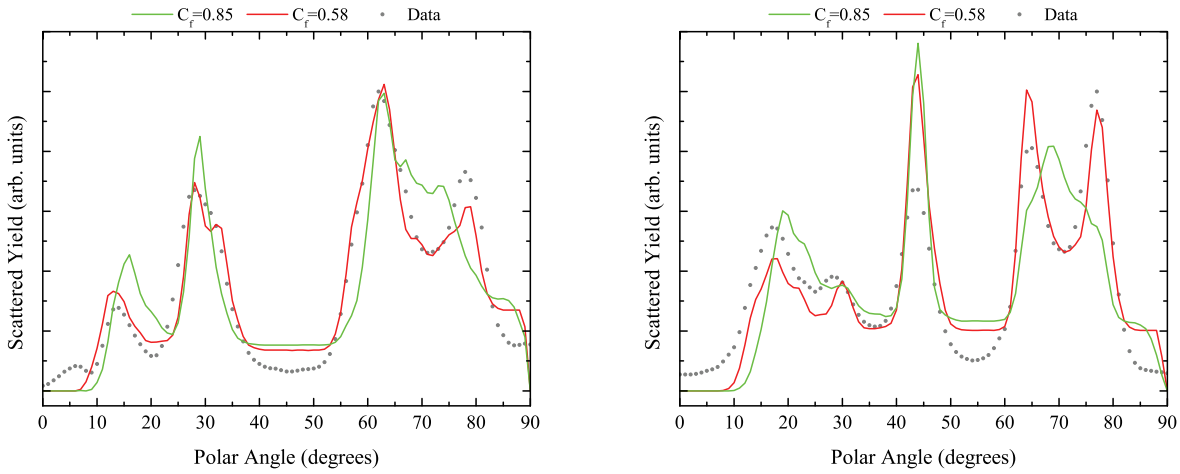

(a) ⟨100⟩ azimuthal data (b) ⟨110⟩ azimuthal data

Figure 13.5 Comparison of the CAICISS correction factor to the value suggested by O'Connor [24] for He–Cu. Data and simulations are shown for both the ⟨100⟩ and ⟨11⟩ azimuths.

surface layer and the effect of the correction factor on shadow cone width; inter-layer spacing changes are unable to alter its location. So, either a lower correction factor value is needed, or a large number of lateral displacements in the surface layers. All other spectrum features lead to a similar conclusion. LEED images show no evidence of surface layer reconstruction, so there exists only one possibility; a lower correction factor value.

13.2 Nickel (Ni)

Having established that the new SOAR codes can produce a structural solution comparable with previous studies, the next priority is to further investigate the relationship between atomic number and correction factor. With similar atomic number to Cu, it is hoped that Ni(110) will show a similar correction factor value. The surface was prepared *in situ* with cycles of IBA (as described above); a sharp (1×1) LEED pattern was obtained at 78 eV after cleaning. There is no evidence from LEED images of any surface reconstruction. AES showed no contamination of C, O, S or Ar. Previous CAICISS studies conducted by Walker [3] have suggested a correction factor value of 0.60 for Ni at 3.0 keV. This new study repeats the 3.0 keV measurement and adds three additional energies, 2.0 keV, 2.5 keV and 4.0 keV, for investigation of correction factor energy dependence.

Results

Data were collected at the four incident beam energies detailed above. Having established that SOAR is capable of producing a realistic structural fit, and taking into account that LEED images show no evidence of surface reconstruction, only a single azimuth, $\langle\bar{1}10\rangle$, was collected for Ni(110) at each energy. A single dataset, if chosen carefully, is sufficient for determination of inter-layer spacings if no surface reconstruction is present. Figure 13.6 shows the raw data. Initial inspection reveals some of the expected trends in the data: Peaks become more easily resolved, and the surface peak position moves to lower polar angle with higher beam energy, due to the narrower shadow cones. A notable discrepancy is a large shift in the fourth backscattering peak (around 75°) for the 4.0 keV dataset. Such a large shift in a feature which originates primarily from deep layer atoms immediately suggests an error in data acquisition, and is likely to cause problems with SOAR fitting. Measurement of the theoretical surface peak position (see Figure 13.7) shows that these experimental datasets give a much lower estimate of correction factor than that of O'Connor [24] (0.84) A value somewhere around 0.60 seems more appropriate — in-keeping with the value already obtained for Cu, which is of similar mass.

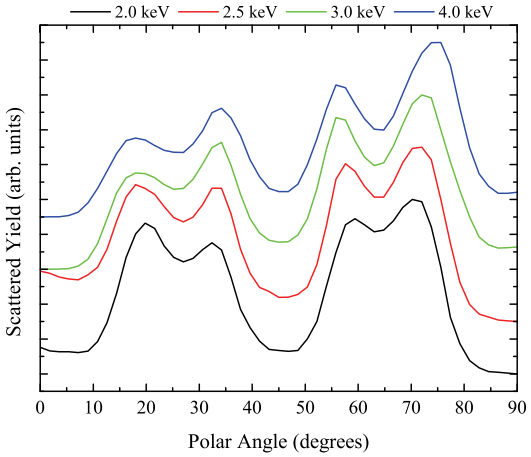

Figure 13.6 Raw data collected for clean Ni(110) in the $\langle\bar{1}10\rangle$ azimuth.

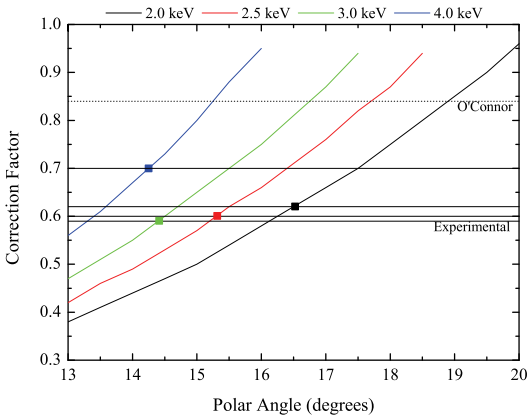

Figure 13.7 Theoretical correction factor (C_f) variation for each incident beam energy on Ni(110), as a function of the angular position of the surface peak in the $\langle\bar{1}10\rangle$ azimuth.

R-space plots (not shown) of correction factor variation for each incident beam energy return optimum correction factor values consistently between 0.55 and 0.60, which is in agreement with previous CAICISS studies [3], and the earlier result for Cu. It appears, from preliminary analysis that there is no variation of correction factor in the energy range tested. A constant value of 0.60 was chosen for production of *R*-space plots for the remaining structural parameters. Important structural parameters were identified as the first and second inter-layer spacing changes (Δ_{12} and Δ_{23} respectively). No surface reconstruction has been observed. Table 13.5 shows the intervals used for SOAR. Data from each incident beam energy was simulated independently to test convergence upon a common structure.

Figure 13.8 and Table 13.6 show the final optimised fits for the Ni datasets and corresponding *R*-factors. Higher background intensity in the 2.0 keV and 2.5 keV datasets is the cause of the higher *R*-factors. The position of features is fitted well in all but one case — the $\sim 75°$ peak of the 4.0 keV dataset. This was discussed as a possible problematic peak in the lead up to optimisation, and it proved to be so. The inability of SOAR to fit this peak with any sensible parameter values has contributed to the larger error estimates seen for the 4.0 keV dataset. Final parameter values with error estimate are shown in Table 13.7. Invariant areas

Table 13.5 Approximate intervals for input to SOAR.

Parameter		Lower	Upper
Correction Factor	C_f	+0.50	+0.70
First inter-layer spacing change	Δ_{12}	−0.200	+0.300
Second inter-layer spacing change	Δ_{23}	−0.100	+0.250

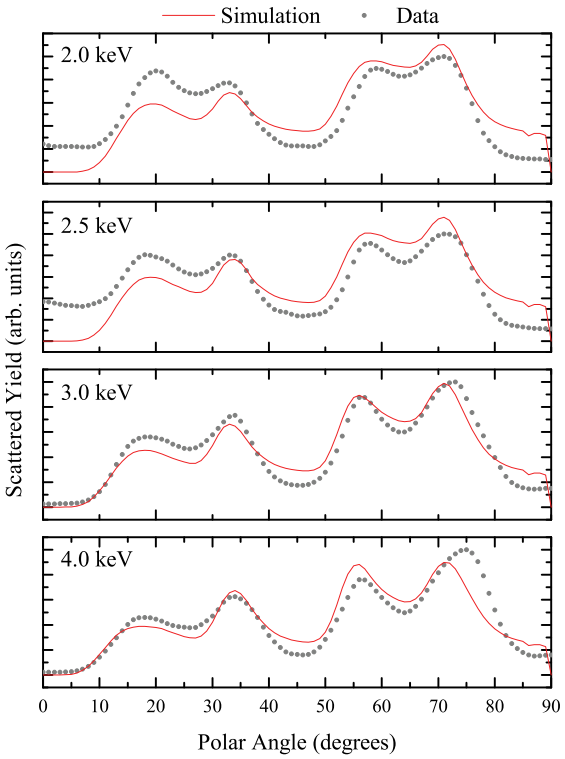

Figure 13.8 SOAR optimised fits for clean Ni(110) in the $\langle\bar{1}10\rangle$ azimuth.

Table 13.6 Comparison of bulk and SOAR optimised R-factors.

Energy (keV)	R-factor	
	Bulk	Optimised
2.0	9.57	9.25
2.5	10.39	9.83
3.0	2.81	2.44
4.0	2.95	2.29

of the spectra are once again causing overestimated errors. Adjustment using Equation 13.1 derived during Cu data analysis provides more reasonable estimates.

All datasets seem to show a similar structural solution, and exhibit the same oscillatory relaxation seen for clean Cu — a correction factor of (0.57 ± 0.02), a first inter-layer contraction from the bulk Ni value of 1.25 Å of (4.0 ± 3.2) %, and a second inter-layer spacing expansion of (2.4 ± 2.4) %. The close agreement of most datasets suggests that errors are still being overestimated. The proposed structural solution compares well with a number of previous studies which were reviewed by Rodriguez [4]. In general, Rodriguez found that first inter-layer spacing were reported to contract by around 7 %, and the second inter-layer spacing to expand by around 3.5 %.

Table 13.7 The final parameter values for clean Ni(110), with associated error estimates. Further discussion of error estimates and their adjustment is found in the text.

	Value	Error Est.	Adjusted		Value	Error Est.	Adjusted
Energy: 2.0 keV				Energy: 3.0 keV			
C_f	+0.56	±0.20	±0.04	C_f	+0.57	±0.24	±0.05
Δ_{12}	−0.100	±0.483	±0.097	Δ_{12}	−0.044	±0.409	±0.082
Δ_{23}	+0.024	±0.238	±0.048	Δ_{23}	+0.016	±0.278	±0.056
Energy: 2.5 keV				Energy: 4.0 keV			
C_f	+0.60	±0.35	±0.07	C_f	+0.57	±0.19	±0.02
Δ_{12}	−0.028	±0.387	±0.077	Δ_{12}	−0.030	±0.485	±0.098
Δ_{23}	+0.031	±0.243	±0.049	Δ_{23}	+0.041	±0.522	±0.104

The screening correction factor derived from CAICISS analysis seems to be at odds with the accepted O'Connor correction factor. All datasets show a similar value for correction factor (around 0.57), with no evidence for any incident beam energy dependence. This is a similar result to that observed for Cu, adding weight to the argument that the CAICISS correction factor really does deviate from the values predicted by O'Connor. A larger range of target masses is required in order to properly assess the variation of correction factor. A pair of high atomic number elements were studied in similar fashion to Cu and Ni. The choice was limited by availability of materials, but two suitable candidates were found — Pt and Au.

13.3 Platinum (Pt)

The study of the Cu(100) and Ni(110) surfaces seems to show that there is a reproducible discrepancy between results from CAICISS experiments and the O'Connor correction factors. To assess the variation of correction factor it is important to establish the correction factor variation over a range of target masses. If a similar correction factor relation to that proposed by O'Connor holds true, then it is expected that an increase in correction factor will be observed for heavier elements.

Pt is a good element to begin the high-Z investigation. Walker conducted a recent CAICISS study [3] of the clean Pt(111) surface at a single incident beam energy (3 keV) using the same apparatus, which provided a structural solution and an estimate of 0.78 ± 0.02 for the correction factor. If a similar correction factor to that observed by Walker is seen over the range of energies presented in this thesis then it provides more good evidence of a modified correction factor relation; the suggested O'Connor correction factor is 1.00 for Pt. The Pt(111)

surface was prepared *in situ* with cycles of IBA; a sharp (1×1) LEED pattern was obtained at 130 eV after cleaning. AES showed no contamination of C, O, S or Ar.

Results

Raw data were collected at five energies — 2.0 keV, 2.5 keV, 3.0 keV, 3.5 keV and 4.0 keV. Figure 13.9 shows the raw Pt backscattering data collected and the theoretical variation of correction factor with surface peak position. Raw data shows an improvement in resolution and decrease in surface peak angle with increasing energy, consistent with the reduction in shadow cone radius at higher energies.

Accurate correction factor estimation from raw data is more challenging in this case because of the wide, and low-count, surface peaks obtained from Pt(111). The lack of intensity in the surface peaks is consistent across all datasets. The most likely explanation is that the beam was aligned such that at low polar angles it was not fully incident on the crystal face. This problem will always be present to some degree because of the finite size of the beam spot. The beam spot is approximately 2 mm in diameter. Simple geometry shows that at grazing incidence the visible width of the Pt(111) crystal face is $\sim$ 1 mm. The alternative case has already been seen in the analysis of Ni(110) data — where the beam impacts the side of the sample, creating a large number of background counts at grazing incidence.

Despite this, some estimate of correction factor can still be made — albeit with large uncertainty. Surface peaks appear to occur in the polar angle range 11° to 15°, which translates to correction factors in the range 0.5 to 0.9. It is worth noting that the previous result (0.78) of Walker fits the surface peak position of all the datasets better than the O'Connor factor (1.00). A more detailed fitting of the data will allow a more accurate correction factor value

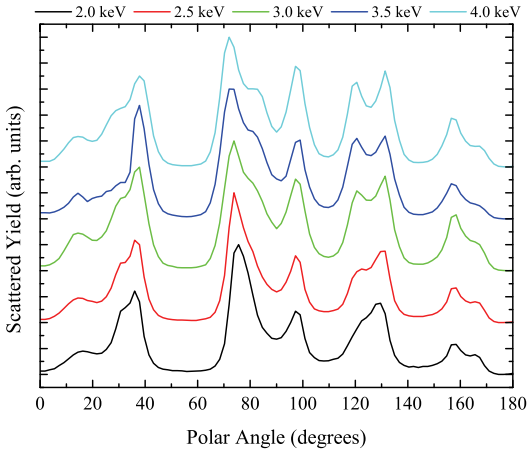

Figure 13.9 Raw data collected for clean Pt(111) in the ⟨211⟩ azimuth.

to be identified. Beginning with a bulk-terminated crystal, the R-space variation of correction factor was mapped out for each dataset.

SOAR was run for data from each incident beam energy independently using the intervals shown in Table 13.8, the results of which are shown in Figure 13.10 as a final optimised fit for each dataset. The 40° polar angle feature in the 3.0 keV and 3.5 keV datasets shows signs of possible ion source fluctuations. The number of counts in the affected features is noticeably higher than for the other three incident beam energies. R-factors for optimised fits are between 5 % and 10 % lower than the initial bulk-terminated structures.

Table 13.9 shows the structural parameters output by SOAR for each dataset. It was not necessary to apply adjusted error estimates (Equation 13.1) to the data obtained from the clean Pt(111) surface. This may be due to the significantly larger number of counts in these datasets than those obtained for any other of the clean surfaces. The CAICISS ion beam was initialised and aligned according to the same procedure throughout all studies. So, why exactly this crystal returns more counts than the other high-Z element tested (see the Au study below) is somewhat of a mystery to be investigated at a later date, although variations in crystal quality and beam alignment seem the most likely causes. All datasets show a common structural solution within the error estimates. The first inter-layer spacing was found to contract from the bulk Pt value of 2.27 Å by an average of (3.1 ± 0.9) %; the second inter-layer spacing showed an expansion of (7.0 ± 0.9) %, and the outermost surface layer exhibits a rumpling of amplitude approximately (0.1 ± 0.02) Å. Importantly, all datasets show the same correction factor within the error estimates (0.74 ± 0.01).

The correction factor resulting from CAICISS analysis (0.74) is once again lower than the O'Connor correction factor (1.00). The Pt(111) datasets show no incident energy dependence on correction factor, and the most consistent structural results from SOAR obtained to date. The structural solution agrees well with previous studies by Walker and Rodriguez [3, 4]. Investigation of another high-Z element will help to establish the correction factor for this region with more certainty.

Table 13.8 Approximate intervals for input to SOAR.

Parameter		Lower	Upper
Correction Factor	C_f	+0.65	+0.85
First inter-layer spacing change	Δ_{12}	−0.300	+0.200
Second inter-layer spacing change	Δ_{23}	−0.100	+0.300
First layer rumpling amplitude	Γ_1	−0.250	+0.250

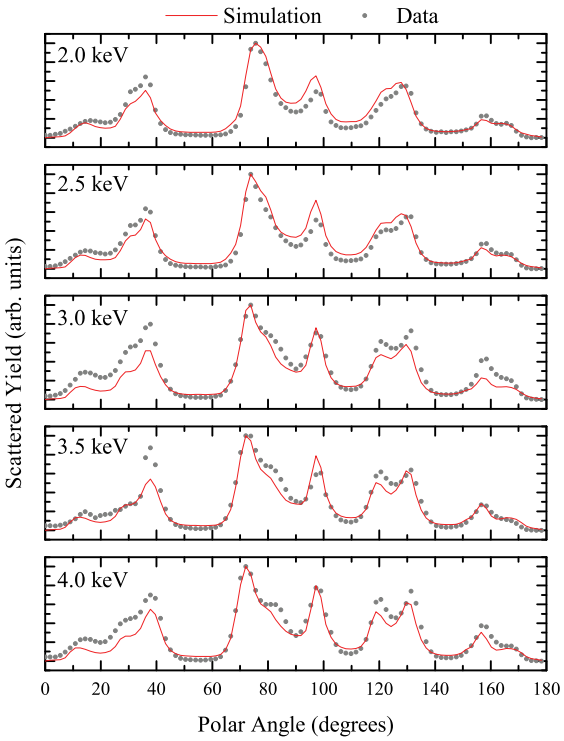

Figure 13.10 SOAR optimised fits for clean Pt(111) in the ⟨211⟩ azimuth.

Table 13.9 The final parameter values for clean Pt(111), with associated error estimates.

Parameter	Value	Error Est.	Parameter	Value	Error Est.
Energy: 2.0 keV			Energy: 3.5 keV		
C_f	+0.74	±0.02	C_f	+0.72	±0.02
Δ_{12}	−0.059	±0.042	Δ_{12}	−0.082	±0.041
Δ_{23}	+0.123	±0.033	Δ_{23}	+0.180	±0.032
Γ_1	+0.116	±0.041	Γ_1	+0.106	±0.050
Energy: 2.5 keV			Energy: 4.0 keV		
C_f	+0.74	±0.02	C_f	+0.74	±0.02
Δ_{12}	−0.041	±0.041	Δ_{12}	−0.064	±0.057
Δ_{23}	+0.134	±0.034	Δ_{23}	+0.189	±0.055
Γ_1	+0.118	±0.059	Γ_1	+0.095	±0.058
Energy: 3.0 keV					
C_f	+0.74	±0.02			
Δ_{12}	−0.104	±0.050			
Δ_{23}	+0.170	±0.048			
Γ_1	+0.116	±0.036			

13.4 Gold (Au)

Investigations of the clean Cu(100), Ni(110) and Pt(111) surfaces have provided an indication that the requirement for reduced correction factor values to fit CAICISS data is consistent across a wide range of target masses. Further investigation focusing on the clean Au(111) surface will allow the correction factor relation with atomic number in this region of the periodic table to be determined with more certainty. The surface was prepared *in situ* with cycles of IBA; a sharp (1×1) LEED pattern was obtained at 53 eV after cleaning. AES showed no contamination from C, O, S or Ar. Data were collected at four incident beam energies — 2.0 keV, 3.0 keV, 3.5 keV and 4.0 keV — in the ⟨211⟩ azimuth.

Results

Surface peak positions of each dataset (Figure 13.11) were measured to give an initial estimate of correction factor. Because of the broad surface peak seen in every dataset, measuring the position with any accuracy is not possible. This is reflected in the large range of experimental lines shown in Figure 13.12, although it is clear that all values once more lie well below the value suggested by O'Connor. A similar situation existed for data collected from the Pt(111) surface in Section 13.3. Values lie between 0.67 and 0.78 — consistent with the result obtained for Pt (0.74).

R-space plots (not shown) were conducted for the bulk-terminated Au(111) crystal; the resulting SOAR intervals are shown in Table 13.10. All datasets show a minimum in correction factor between 0.70 and 0.80, with no clear trend shown up or down with incident energy. The

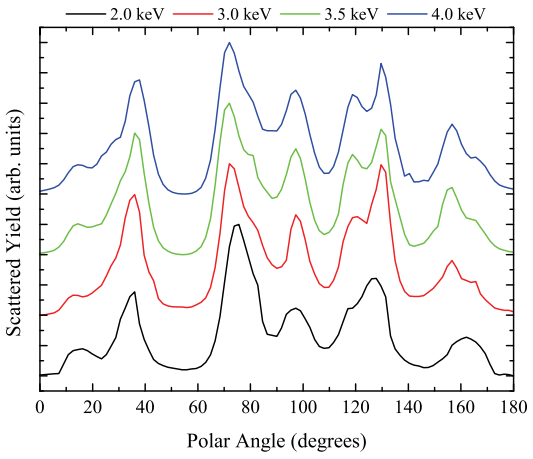

Figure 13.11 Raw data collected for clean Au(111) in the ⟨211⟩ azimuth.

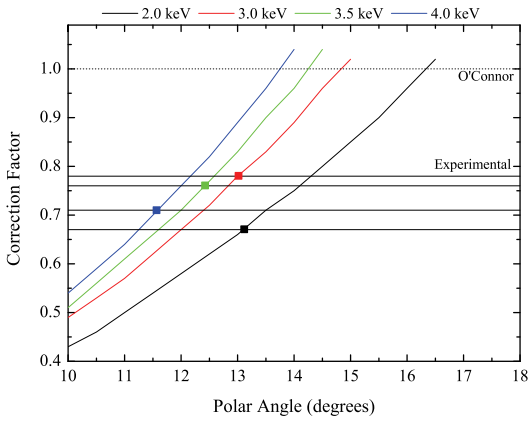

Figure 13.12 Theoretical correction factor (C_f) variation for each incident beam energy on Au(111), as a function of the angular position of the surface peak in the ⟨211⟩ azimuth.

Table 13.10 Approximate intervals for input to SOAR.

Parameter		Lower	Upper
Correction Factor	C_f	+0.65	+0.85
First inter-layer spacing change	Δ_{12}	−0.200	+0.200
Second inter-layer spacing change	Δ_{23}	−0.100	+0.300
First layer rumpling amplitude	Γ_1	−0.300	+0.300

key structural parameters identified were the same as for the Pt(111) system above — first and second interlayer spacing changes, and first layer rumpling. Both inter-layer spacings show a simple single-minimum relation. Rumpling shows approximate symmetry[‡] about zero displacement with a minimum either side (with exception of the 2.0 keV dataset, which shows almost no variation in the range tested. This is attributed to one of the surface peaks being poorly resolved from its neighbour). The rumpling parameter is defined such that it shifts adjacent atoms in alternating directions, so it is expected that a degeneracy will be seen here — depending on which atoms are up and which are down. For these simulated cases differences may be seen depending on which minimum is chosen because the periodic rumpling is propagated across many unit cells. In a real system the rumpling is likely to be more random and short-range, averaging out any difference between the minima.

SOAR was run independently for datasets of each incident beam energy; optimised fits are shown in Figure 13.13. The 2.0 keV dataset proved to be the most problematic for SOAR to fit, due to the poorly resolved surface peak. This has led to a very large error estimate for first layer rumpling — not unexpected because of how flat the R-space plot was for this parameter. The large error estimates for the 2 keV dataset likely result from the lack of resolved peaks in the raw data, which is particularly noticeable in peaks at polar angles higher than 110° (possibly due to the beam spot not being fully incident on the sample). The surface peak, which displays well-resolved multiple contributions at all other incident energies, is recorded as a single feature. All datasets show similar relaxations (parameter values are given in Table 13.11), and no variation of correction factor with incident beam energy. The first inter-layer spacing is contracted by an average of (3.0 ± 1.3) % from the bulk Au value of 2.36 Å. The second inter-layer spacing in expanded by (4.7 ± 2.5) %. The rumpling amplitude was found to be (0.1 ± 0.03) Å if one excludes the problematic 2.0 keV dataset as anomalous. The results compare well with the review of previous studies compiled by Rodriquez [4] — relaxations are in the same direction and of similar magnitude. Results also compare well

‡ The symmetry here is only approximate, because the crystal is not symmetric about normal incidence in this azimuth.

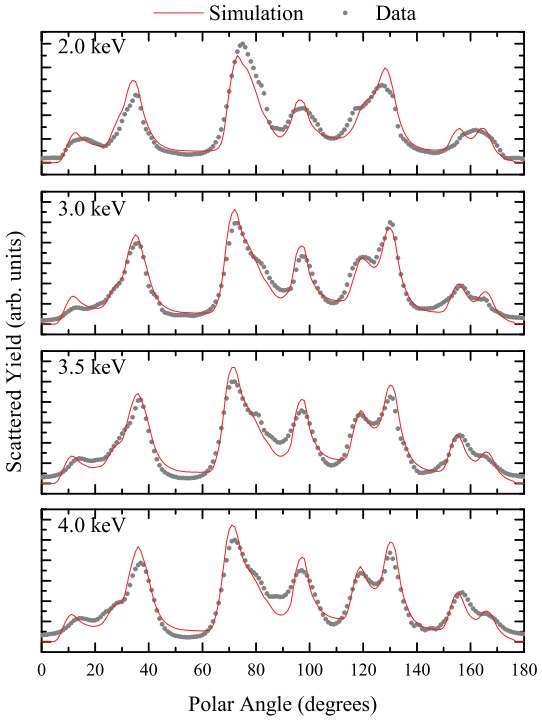

Figure 13.13 SOAR optimised fits for clean Au(111) in the ⟨211⟩ azimuth.

Table 13.11 The final parameter values for clean Au(111), with associated error estimates.

Parameter	Value	Error Est.	Parameter	Value	Error Est.
Energy: 2.0 keV			Energy: 3.5 keV		
C_f	+0.74	±0.02	C_f	+0.75	±0.03
Δ_{12}	−0.069	±0.042	Δ_{12}	−0.098	±0.051
Δ_{23}	+0.091	±0.080	Δ_{23}	+0.139	±0.185
Γ_1	−0.029	±0.413	Γ_1	−0.089	±0.044
Energy: 3.0 keV			Energy: 4.0 keV		
C_f	+0.75	±0.02	C_f	+0.77	±0.03
Δ_{12}	−0.033	±0.060	Δ_{12}	−0.072	±0.054
Δ_{23}	+0.094	±0.089	Δ_{23}	+0.099	±0.075
Γ_1	−0.100	±0.047	Γ_1	−0.100	±0.045

to the values seen for clean Pt(111) in Section 13.3, with both surfaces exhibiting oscillatory relaxations.

Analysis of CAICISS data collected from the Au(111) surface has produced a correction factor of approximately 0.75, which is very close to the value found for Pt(111) (0.74). The level of consistency seen so far in correction factor between elements of similar atomic number is very good evidence that there is a discrepancy between CAICISS results and O'Connor correction factors. There also appears to be an approximately constant deviation from the O'Connor values, with CAICISS results producing correction factors around 0.25 lower for all elements. Hopefully this can be confirmed by taking an additional point in between the two atomic number ranges tested already.

13.5 Palladium (Pd)

Investigation of Pd(111) was undertaken with the intention of beginning to fill in the gaps in the relation between correction factor and atomic number. Four surfaces have been tested to date — two with high-Z (Pt(111) and Au(111)) and two with low-Z (Ni(110) and Cu(100)). All have shown a decreased correction factor from that predicted by O'Connor [24]. A previous CAICISS study [3] of InN with an incident beam energy of 3.0 keV produced an approximate correction factor value of 0.70 for In, although the authors noted that the spectral fits were limited in accuracy, possibly due to mobile In atoms in the surface layer. Pd is close in atomic number to In, so it is expected that Pd will show a similar correction factor. The surface was prepared *in situ* with cycles of IBA (as described above); a sharp (1×1) LEED pattern was obtained at 56 eV after cleaning. AES showed no contamination from C, O, S or Ar.

This study presents data collected at five different incident beam energies — 2.0 keV, 2.5 keV, 3.0 keV, 3.5 keV and 4.0 keV. For each dataset, a structural solution is identified, and an estimate of correction factor is made.

Results

The processed raw data is shown in Figure 13.14. As has been the case with previous studies, the surface peak in each dataset is quite wide. This is useful in suggesting that there is a rumpling in the outermost atomic layer, but makes measurement of surface peak position difficult. Despite this, some estimate of correction factor can still be made — albeit with large uncertainty. Surface peaks appear to occur in the polar angle range 11° to 14°. The value for In (0.70) of Walker fits the surface peak position of all the datasets better than the O'Connor

factor (Figure 13.15). A more detailed fitting of the data will allow a more accurate correction factor value to be identified.

The key structural parameters were identified as being the same as the two previously studied (111) oriented crystals (see Table 13.12). Raw data has already suggested there is a rumpling in the first layer, and inter-layer spacings are very likely to be modified due to the change of potential in the near surface layers. Obviously, correction factor is also varied, so that the optimal value for each dataset can be found.

R-space plots (not shown) were conducted via simulations of a bulk-terminated Pd crystal; They showed that optimum correction factor values fall in the range 0.65 to 0.75 for all datasets. This is right in the region expected to be consistent with the other elements tested in this study and previous studies. All inter-layer spacings showed a simple variation with a single minimum, so they should pose no great problem for SOAR fitting. The first layer rumpling parameter variation was very shallow, which is caused by the poorly resolved surface peaks in the raw data. As a result, large error estimates are expected for this parameter. The intervals used for SOAR fitting are shown in Table 13.12.

Table 13.12 Approximate intervals for input to SOAR.

Parameter		Lower	Upper
Correction Factor	C_f	+0.65	+0.85
First inter-layer spacing change	Δ_{12}	−0.200	+0.200
Second inter-layer spacing change	Δ_{23}	−0.100	+0.300
First layer rumpling amplitude	Γ_1	−0.300	+0.300

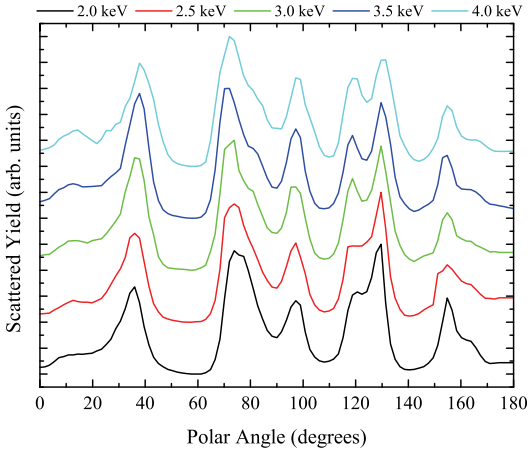

Figure 13.14 Raw data collected for clean Pd(111) in the ⟨211⟩ azimuth.

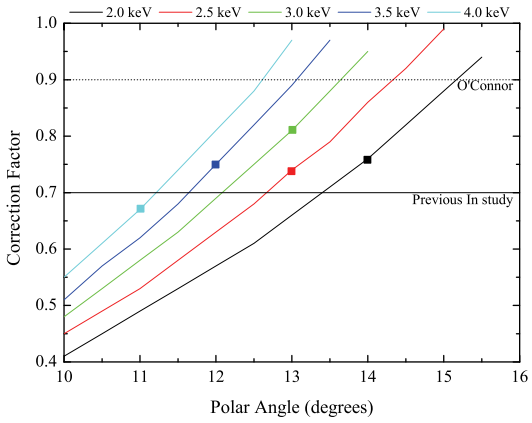

Figure 13.15 Theoretical correction factor (C_f) variation for each incident beam energy on Pd(111), as a function of the angular position of the surface peak in the ⟨211⟩ azimuth.

The optimised plots after SOAR fitting are shown in Figure 13.16. The positions of all major backscattering features are well reproduced for all datasets. Some of the usual background intensity problems are present, but relative peak intensities seem to be reasonably good in nearly all cases. Surface peaks are noticeably wider in the raw data than in the computer simulations, although their intensity is well matched. This suggests that the data collected at very shallow polar angles is still subject to some distortion created by beam spot size — beam not being fully on the desired face of the crystal. SOAR fitting reduces R-factors by ~ 10 % compared to the bulk terminated crystal.

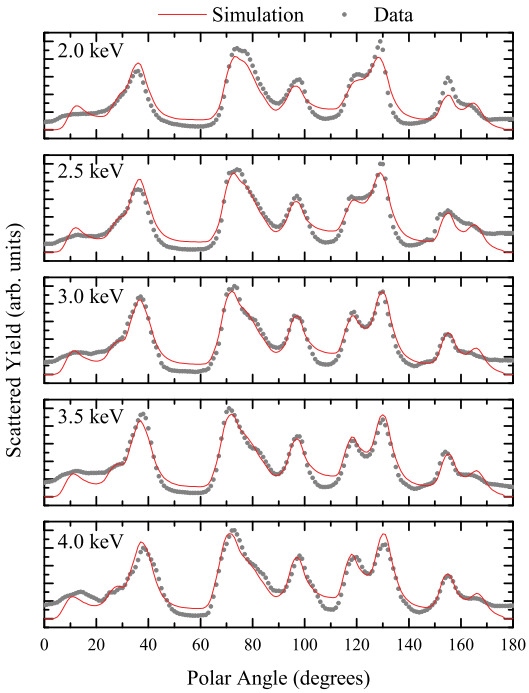

Figure 13.16 SOAR optimised fits for clean Pd(111) in the ⟨211⟩ azimuth.

The structural parameters output by SOAR (see Table 13.13) show a common solution with the estimated error bounds. Errors have been adjusted using Equation 13.1. The first inter-layer spacing is contracted by an average of (3.6 ± 1.3) % from the bulk Pd value of 2.25 Å. The second is also contracted by (1.3 ± 1.8) %. The large errors predicted to be seen for first layer rumpling because of the shallow R-space variation are very obvious in the final results. Most datasets settled on a value very close to zero for rumpling, the average being (-0.02 ± 0.06) Å.

The correction factor for Pd was found to be (0.71 ± 0.02) — very close to the predicted value. This fits well with the value determined by Walker [3] for In (which is of similar mass) and with CAICISS results presented here for other elements. Once again, this is lower than the value predicted from the work of O'Connor.

Table 13.13 The final parameter values for clean Pd(111), with associated error estimates.

Parameter	Value	Error Est.	Parameter	Value	Error Est.
Energy: 2.0 keV			Energy: 3.5 keV		
C_f	+0.69	±0.02	C_f	+0.73	±0.03
Δ_{12}	−0.102	±0.063	Δ_{12}	−0.051	±0.077
Δ_{23}	−0.042	±0.067	Δ_{23}	−0.034	±0.092
Γ_1	−0.011	±0.090	Γ_1	−0.015	±0.155
Energy: 2.5 keV			Energy: 4.0 keV		
C_f	+0.71	±0.03	C_f	+0.73	±0.04
Δ_{12}	−0.100	±0.069	Δ_{12}	−0.072	±0.085
Δ_{23}	−0.042	±0.070	Δ_{23}	−0.024	±0.111
Γ_1	+0.000	±0.180	Γ_1	−0.006	±0.104
Energy: 3.0 keV					
C_f	+0.70	±0.04			
Δ_{12}	−0.063	±0.043			
Δ_{23}	−0.028	±0.037			
Γ_1	−0.045	±0.140			

13.6 Conclusions

Results of studies of five clean metal surfaces have been presented in an attempt to explain discrepancies seen between CAICISS studies conducted at Warwick and results from other researchers using similar techniques. Previous work by O'Connor [24] provided an empirical formula for correction factor values. However, recent CAICISS studies [3, 43, 90] have shown significant deviation from the O'Connor formula. In all cases to date the values of O'Connor have been too high when applied to CAICISS data. The previous CAICISS studies have all been limited in the scope of their investigation of the effect because it was not the primary focus of the work. Comparison of CAICISS studies to other ion beam techniques led to the idea that the combination of a low-mass and low-energy incident ion beam may be the cause of the deviation.

Clean metal surfaces generally have simple surface structure. They have been studied many times previously, and as a result, there are many results with which to compare structural fitting from CAICISS data. Using a structural fitting routine (SOAR) on each dataset, the aim was to find the incident beam energy and target atomic number dependence on the correction factor for CAICISS experiments. Each of the 5 elements studied shows that the correction factors obtained were independent of the incident beam energy used. In all cases, correction factors were approximately 0.25 lower than the values proposed by O'Connor. Figure 13.17

shows the experimental points obtained (with approximate error estimates). The values obtained from O'Connor's empirical formula are shown by the solid line. The dashed line was obtained by subtracting 0.26 from all points of the O'Connor relation.

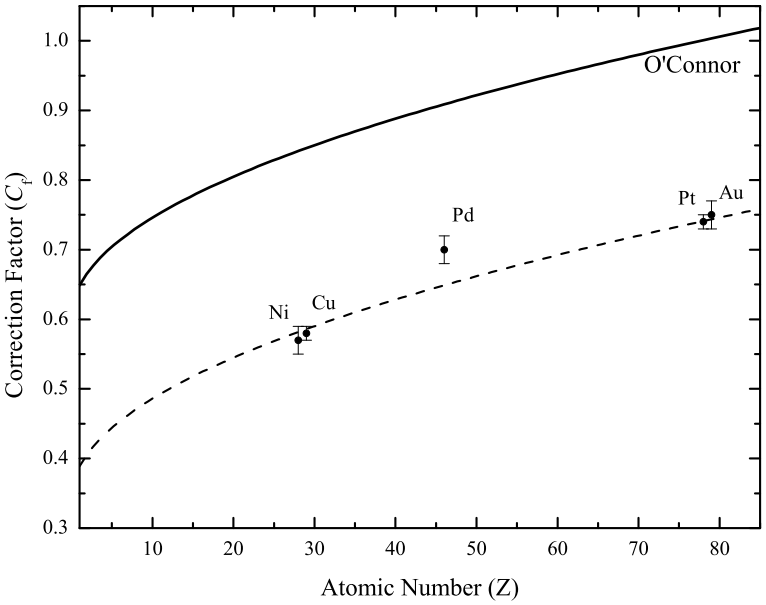

Figure 13.17 Summary plot showing correction factor variation with atomic number for each element. The dashed line shows the O'Connor relation translated by -0.26

The correction factor obtained for Pd is above the new suggested fit line. It is unclear whether this is because the result for Pd is erroneous, or whether the curvature of the fit line needs to be modified. It is also unclear (because of the absence of any very low-Z elements) how the relationship tails off as atomic number is reduced. Both of these issues require further investigation, but finding elements which are suitable and readily available is problematic. Most commonly available crystals have already been tested in this study. Two remaining crystals are Al (difficult to clean), and Si (which although it has a complex reconstruction, has been well-studied). Looking towards the higher end of the periodic table it becomes difficult to pick out any obvious candidates. Some attempts were made during the course of this project to use the MBE facilities at Warwick to grow single crystals on GaAs substrates. Specifically, Sb growth of several hundred microns was attempted. Unfortunately, due to time constraints this work was not completed, but it opened up the possibility of growing bulk-like single crystal of some less abundant elements.

There is currently no solid hypothesis as to why CAICISS experiments in particular seem to show such a large deviation from work using similar techniques. Already mentioned, it has been considered that the low mass of the incident beam could be a factor. The majority of other low-energy ion beam techniques use beams of notably higher mass, Ne or Ar for example. Some studies exist that suggest the discrepancies in correction factor are seen even with these

higher mass ion beams [107, 108]. If this can be verified by further investigation, then it seems likely the deviations are due to an incorrect treatment of the interaction potential in the low-energy scattering regime.

During beam production, a neutral atom is stripped of an electron to create an ion. In the case of He this means removing half of its electrons — a much larger percentage than for heavier elements. Obviously, as the number of electrons increases the removal of a single one becomes less significant. Therefore, it is reasonable to assume that there should be a large difference in the screening length between ion beams of different mass. If the potential used fails to accurately model this change for very low ion beam masses then it could be a contributing factor in accounting for the differences seen. Further testing is needed, utilising ion beams of varying mass, in order to ascertain whether the use of He ion beams is the cause of the different correction factors seen. The Warwick CAICISS system is capable of running a Ne ion beam, but changing between gases requires a down-time, and analysis is considerably more complex because of the presence of multiple isotopes — which leads to multiple TOF peaks from a single target element.

During the course of studying these clean metal surfaces a paper was published by Primetzhofer et al. [97] relating to correction factors in LEIS. The study reported on the result of angular scans performed on a Cu(100) with He^+ ions. It drew into question the validity of simulations from the FAN codes, and suggested that a molecular dynamics package — the KALYPSO codes (Karolewski) [47] — are far more effective. The authors suggested that the low correction factors seen in FAN simulations were a consequence of the code conducting a poor simulation. Examination of their findings reveals that the LEIS system employed by the authors collects ions at 129° scattering angle. The manual for the FAN codes specifically states that the software is designed for near-perfect 180° backscattering simulations due to cross-section dependencies not being included in the design.

Despite the questionable application of the FAN codes by Primetzhofer et al. the direct relevance of their claims to this project necessitated additional study in order to confirm or refute these allegations. A detailed comparison [48, 49] between KALYPSO and FAN[§] concluded that while FAN does not reproduce the relative intensities of peaks as accurately as KALYPSO, the vastly simpler FAN code runs several hundred times faster and thus proves to be much more usable for optimised fitting. Importantly, in the case of 180° backscattering, no difference was seen in correction factors between FAN and KALYPSO. It appears that, for CAICISS studies, the FAN simulation code provides perfectly valid simulations.

[§] The comparison of KALYPSO and FAN simulation codes has been submitted for publication but not included in this thesis because all KALYPSO simulations were conducted by Dr. Marc Walker.

Part IV

CHAPTER 14

Summary and future studies

A combination of modern surface science techniques (CAICISS, MEIS, LEED, AES) has been used to investigate a number of metallic and complex bi-metallic systems. Part I covered some of the essential background theory of ion scattering and supplementary techniques (LEED and AES), and outlined the data analysis processes in place.

In Part II, the Cu(100)/Sn system was investigated. It is a complex bi-metallic system, displaying multiple surface reconstructions at sub-monolayer coverage. Five reconstructions were examined with ion scattering techniques — MEIS and CAICISS. Models for each phase, proposed by previous studies, were tested and the best candidates optimised to produce structural solutions. During the analysis phase of this investigation, the new SOAR codes were developed to aid optimisation of structural fits. Chapter 11 contains a more complete summary of the experimental findings of this investigation.

In Part III, limitations of the Warwick CAICISS system have been identified and addressed as a result of challenges encountered during the study of the Cu(100)/Sn system (Chapter 12). An investigation was carried out to accurately determine CAICISS correction factors for ion-surface interactions (Chapter 13). Five clean metal surfaces were examined with CAICISS at a range of incident ion energies. A correction factor relation similar to that derived by previous authors was found to hold true, but at consistently lower values for all elements investigated. Incident ion kinetic energy dependence seems to have been ruled out, as no change in correction factors was seen in the range 1 keV to 5 keV. During this investigation, further improvements were made to the new SOAR codes to include optimisation of CAICISS correction factors.

14.1 Future studies

Although the results of the CAICISS correction factor investigation are consistent and reproducible, the reasons for the deviation from the accepted correction factors are still unclear. Further research is needed to fully understand the ion-surface interaction, which is fundamental to accurately characterising surfaces. It is possible that the incident ion mass could have an effect on the correction factors; this needs to be tested. As well as the He gas currently used in

CAICISS, Ne is available. But, it brings with it additional complications due to the presence of multiple isotopes in the gas — two sets of ToF peaks will be detected because of the different isotope masses. Ideally, a range of incident ion masses should be tested.

A large amount of time during this project has been spent attempting to improve the Warwick CAICISS system. Many of the limitations identified have been dealt with, but equally many were too expensive or time-consuming to pursue. A redesign of the ion column — especially the beam focusing and steering — is essential to get much more improvement from the apparatus. Much of the beam produced is being wasted at present, but despite that wastage data collection runs have been reduced in duration by more than a factor of 3. With a redesign, it is hoped that the CAICISS system will achieve run times short enough to enable *in situ* observation of MBE growth. The energy range of the source is currently limited to 5 keV; this could be increased by installation of a new isolator in the source control electronics. Many of the feedthroughs on the system are already rated to 15 kV, so the increase should not trigger the need to replace any important components. The increased energy range would allow the dependence of correction factors on incident energy to be tested further. Completion of the sample transfer system will be a good step in the right direction for the main chamber, which up until now has required a full vent to change the target crystal.

Good progress has been made on an automated fitting routine for CAICISS, but more work needs to be done on the simulation codes. The IFFCO codes already have multi-processor versions, but the simulation packages — VEGAS and FAN — are uni-processor codes. VEGAS especially is quite old-fashioned in the way it handles memory usage. It was written when memory was scarce and number of computations was low, so many optimisations put in place to decrease solve time in the past are now bottlenecks which prevent the code from being easily parallelised. The source code for FAN is currently unavailable (despite numerous attempts to acquire it). Given access to the code a number of improvements would be easy to implement, including: periodic boundary conditions, and support for more atoms and atom species. Without the code any additions to the package capabilities requires a costly full rewrite.

The variation of work undertaken in this thesis, I think, demonstrates the versatility of ion scattering techniques. Not only are they able to investigate the fundamental physics of the ion-surface interaction; but also complex systems with many different surface reconstructions. Data analysis is straightforward, and will only get faster and more accurate as the simulation codes are improved.

Bibliography

[1] G. A. Somorjai, The surface science concepts of heterogeneous catalysis. the building of complex catalysts systems on single crystal surfaces, Catalysis Today **12** (1992) 343 – 353.

[2] W. Peng, R. H. Victora, J. H. Judy, K. Gao, J. M. Sivertsen, Perpendicular magnetic recording thin film media using Co/Pd superlattice on ultrathin indium-tin-oxide seed layers, J. Appl. Phys. **87** (2000) 6358.

[3] M. Walker, LEIS studies of metal, metal oxide and alloy surfaces, Ph.D. thesis, University of Warwick (2006).

[4] A. M. Rodríguez, G. Bozzolo, J. Ferrante, Multilayer relaxation and surface energies of fcc and bcc metals using equivalent crystal theory, Surf. Sci. **289** (1993) 100 – 126.

[5] R. M. Tromp, E. J. van Loenen, Structure study of Si(111)-(7 × 7) by channeling and blocking, Phys. Rev. B **30** (1984) 7352.

[6] D. P. Woodruff, T. A. Delchar, Modern Techniques in Surface Science, 2nd Edition, Cambridge University Press, 1986.

[7] E. A. Wood, Vocabulary of surface crystallography, J. Appl. Phys. **35** (1964) 1306.

[8] J. F. Ziegler, J. P. Biersack, U. Littmark, The stopping and range of ions in solids, Pergamon, New York, 1985.

[9] H. Niehus, Ion scattering spectroscopy and scanning tunneling microscopy: A powerful combination for surface structure analysis, Appl. Phys. A **53** (1991) 388.

[10] S. Rubin, Surface analysis by charged particle spectroscopy, Nucl. Instrum. Meth. **5** (1959) 177.

[11] W. K. Chu, J. W. Mayer, M. A. Nicolet, Backscattering Spectroscopy, Wiley-Interscience, New York, 1978.

[12] D. P. Smith, Scattering of low-energy noble gas ions from metal surfaces, J. Appl. Phys. **38** (1967) 340.

[13] D. P. Smith, Analysis of surface composition with low-energy backscattered ions, Surf. Sci. **25** (1971) 171.

[14] N. S. Kaijaks, Ion-scattering spectroscopy of III-V semiconductor surfaces, Ph.D. thesis, University of Warwick (2000).

[15] J. F. van der Veen, Ion beam crystallography of surfaces and interfaces, Surf. Sci. Rep. **5** (1985) 199.

[16] H. Niehus, R. Spitzl, Ion-solid interaction at low energies: Principles and application of quantitative ISS, Surf. Interface Anal. **16** (1991) 287 – 307.

[17] M. Aono, C. Oshima, S. Zaima, S. Otani, Y. Ishizawa, Quantitative surface atomic geometry and two-dimensional surface electron distribution analysis by a new technique in LEIS, Jap. J. Appl. Phys. **20** (1981) L829.

[18] E. Rutherford, The scattering of alpha and beta particles by matter and the structure of the atom, Philosophical Magazine **5** (1911) 669.

[19] R. M. Charatan, R. S. Williams, Scattering of low energy ions from surfaces at 180 degrees, Surf. Sci. **264** (1991) L207.

[20] G. Molière, Therorie der Streuung schneller geladener Teilchen I. Einzelstreuung am abgeschirmten Coulomb-Feld, Z. Naturforsch **2a** (1974) 133.

[21] S. A. Cruz, E. V. Alonso, R. P. Walker, D. J. Martin, D. G. Armour, Interatomic potential considerations in LEIS, Nucl. Instrum. Meth. **194** (1982) 659.

[22] O. B. Firsov, Calculation of atomic interaction potentials, J. Exptl. Theoret. Phys. (U.S.S.R.) **33** (1957) 696.

[23] J. Lindhard, M. Scharff, H. E. Schiott, Range concepts and heavy ion ranges, Mat. Fys. Medd. Dan. Vid. Selsk. **33** (1963) 1 – 42.

[24] D. J. O'Connor, J. P. Biersack, Comparison of theoretical and empirical interatomic potentials, Nucl. Instrum. Meth. B **15** (1986) 14.

[25] O. S. Oen, Universal shadow cone expressions for an atom in an ion beam, Surf. Sci. **131** (1983) L407.

[26] M. Aono, R. Souda, Quantitative surface atomic structure analysis by low-energy ion scattering spectroscopy (ISS), Jap. J. Appl. Phys. **24** (1985) 1249.

[27] T. H. Fauster, Surface geometry determination by large-angle ion scattering, Vacuum **38** (1987) 129 – 142.

[28] O. Mironets, H. L. Meyerheim, C. Tusche, P. Zschack, H. Hong, N. Jeutter, R. Felici, J. Kirschner, Surface vibrations and relaxation effects in Cu(001) studied by x-ray diffraction, Phys. Rev. B **78** (2008) 153401.

[29] P. Bailey, T. C. Q. Noakes, C. J. Baddeley, G. van der Laan, D. Brown, P. D. Quinn, D. P. Woodruff, Aspects of layer-by-layer composition analysis using MEIS, Current Applied Physics **3** (2003) 89 – 92.

[30] G. S. Parkinson, Studies of surface and interface structure using medium energy ion scattering, Ph.D. thesis, University of Warwick (2006).

[31] I. Stensgaard, Surface studies with high-energy ion beams, Rep. Prog. Phys. **55** (1992) 989.

[32] M. Aono, M. Katayama, E. Nomura, T. Chassé, D. Choi, M. Kato, Recent developments in low-energy ion scattering spectroscopy (ISS) for surface structural analysis, Nucl. Instrum. Meth. B **37** (1989) 264.

[33] M. Aono, M. Katayama, E. Nomura, Exploring surface structures by CAICISS, Nucl. Instrum. Meth. B **64** (1992) 29 – 37.

[34] T. C. Q. Noakes, CAICISS of semiconductor and metal surfaces, Ph.D. thesis, University of Warwick (1995).

[35] J. L. Wiza, Microchannel plate detectors, Nucl. Instrum. Meth. **162** (1979) 587.

[36] S. B. Luitjens, A. J. Algra, E. P. T. M. Suurmeijer, A. L. Boers, The measurement of energy spectra of neutral particles in low energy ion scattering, Appl. Phys. A **21** (1980) 205.

[37] M. Katayama, E. Nomura, N. Kanekama, H. Soejima, M. Aono, Coaxial impact-collision ion scattering spectroscopy (CAICISS): A novel method for surface structure analysis, Nucl. Instrum. Meth. B **33** (1988) 857.

[38] P. D. Quinn, C. Bittencourt, D. B. amd D. P. Woodruff, T. C. Q. Noakes, P. Bailey2, TLEED and MEIS determination of the Ni(110)-$c(2 \times 2)$-Sn surface structure, J. Phys. Condens. Matter **14** (2002) 665 – 673.

[39] S. P. Tear, K. Röll, M. Prutton, A comparison of reliability(R) factors in a LEED structural analysis of the Cu(111) surface, J. Phys. Condens. Matter **14** (1981) 3297.

[40] K. Pussi, T. McEvoy, C. J. Barnes, A. A. Cafolla, E. AlShamaileh, M. Lindroos, Determination of the structure of Cu(100)-$c(4 \times 4)$-In by TLEED, Surf. Sci. **526** (2003) 141 – 148.

[41] R. Mayer, C. Zhang, K. G. Lynn, W. E. Freize, F. Jona, P. M. Marcus, Low-energy electron and positron diffraction measurements and analysis on Cu(100), Phys. Rev. B **35** (1987) 3102.

[42] M. A. van Hove, W. H. Weinberg, C. M. Chan, Low energy electron diffraction, Springer-Verlag, 1986.

[43] M. Walker, C. R. Parkinson, M. Draxler, M. G. Brown, C. F. McConville, Initial growth of platinum on oxygen-covered Ni(110) surfaces, Surf. Sci. **600** (2006) 3327 – 3336.

[44] D. Briggs, M. P. Seah, Practical surface analysis: Volume 1: Auger and x-ray photoelectron spectroscopy, Wiley & Sons Ltd., 1983.

[45] L. E. Davis, N. C. MacDonald, P. W. Palmberg, G. E. Riach, R. E. Weber, Handbook of Auger Electron Spectroscopy, 2nd Edition, Physical Electronics Industries, Eden Prairie, USA, 1976.

[46] M. T. Robinson, I. M. Torrens, Computer simulation of atomic-displacement cascades in solids in the binary-collision approximation, Phys. Rev. B **9** (1973) 5008 – 5024.

[47] M. A. Karolewski, Kalypso: A software package for molecular dynamics simulation of atomic collisions at surfaces, Nucl. Instrum. Meth. B **230** (2005) 402–405.

[48] M. G. Brown, M. Walker, L. Fishwick, C. F. McConville, Evaluation of the ion-atom interaction potential for He^+ ions scattered from a clean Pt(111) surface, submitted for Publication (March 2009).

[49] M. Walker, M. G. Brown, L. Fishwick, C. F. McConville, Evaluation of the ion-atom interaction potential for He^+ ions scattered from clean transition metal surfaces, submitted for Publication (March 2009).

[50] R. M. Tromp, J. F. van der Veen, Monte carlo simulations of shadowing/blocking experiments for surface structure analysis, Surf. Sci. **133** (1983) 159.

[51] J. F. Frenken, J. F. van der Veen, R. M. Tromp, Theory and simulation of high energy ion scattering experiments for structure analysis of surfaces and interfaces, Nucl. Instrum. Meth. B **17** (1986) 334.

[52] T. C. Q. Noakes, P. Bailey, D. P. Woodruff, Structure determination of surface adsorption and surface alloy phases using medium energy ion scattering, Nucl. Instrum. Meth. B **136** (1998) 1125.

[53] P. R. Bevington, Data reduction and error analysis for the physical sciences, McGraw-Hill, 1992.

[54] P. Gilmore, C. T. Kelley, An implicit filtering algorithm for optimization of functions with many local minima, SIAM J. Optim **5** (1995) 269–285.

[55] F. Abel, C. Cohen, J. A. Davies, J. Moulin, D. Schmaus, Thin-film growth of Sn on Cu(100), Appl. Surf. Sci. **44** (1990) 17 – 27.

[56] E. AlShamaileh, H. Younis, C. J. Barnes, K. Pussi, M. Lindroos, A tensor LEED determination of the structure and compositional profile of a Cu(100)-$c(2 \times 2)$-Pt surface alloy, Surf. Sci. **515** (2002) 94 – 102.

[57] B. Aufray, H. Giordano, D. N. Seidman, A STM study of surface segregation of Sb at a Cu(111) surface, Surf. Sci. **447** (2000) 180 – 186.

[58] C. J. Barnes, E. AlShamaileh, T. Pitkänen, P. Kaukasoina, M. Lindroos, The kinetics of formation and structure of an underlayer alloy: The Cu(100)-$c(2 \times 2)$-Pd system, Surf. Sci. **492** (2001) 55 – 66.

[59] D. D. Chambliss, S. Chiang, Surface alloy formation studied by STM: Cu(100) + Au-$c(2 \times 2)$, Surf. Sci. **264** (1992) L187 – L192.

[60] G. Gilarowski, H. Niehus, Intermixing and subsurface alloy formation: Ir on Cu(100), Surf. Sci. **436** (1999) 107 – 120.

[61] G. L. Kellogg, R. Plass, The relationship between the growth shape of three-dimensional Pb islands on Cu(100) and the domain orientation of the underlying $c(5\sqrt{2} \times \sqrt{2})r45$ structure, Surf. Sci. **465** (2000) L777 – L782.

[62] H. L. Meyerheim, H. Zajonz, W. Moritz, I. K. Robinson, Surface alloying and dealloying in Bi/Cu(001) at low coverage, Surf. Sci. **381** (1997) L551 – L557.

[63] R. Plass, G. L. Kellogg, Surface morphology changes during Pb deposition on Cu(100): Evidence for surface alloyed Cu(100)-$c(2 \times 2)$ Pb, Surf. Sci. **470** (2000) 106 – 120.

[64] P. T. Sprunger, E. Lægsgaard, F. Besenbacher, Growth of Ag on Cu(100) studied by STM: From surface alloying to Ag superstructures, Phys. Rev. B **54** (1996) 8163 – 8171.

[65] A. Pintar, Catalytic processes for the purification of drinking water and industrial effluents, Catalysis Today **77** (2003) 451 – 465.

[66] W. Gao, N. Guan, J. Chen, X. Guan, R. Jin, H. Zeng, Z. Liu, F. Zhang, Titania supported Pd-Cu bimetallic catalyst for the reduction of nitrate in drinking water, Applied Catalysis B **46** (2003) 341 – 351.

[67] C. Argile, G. E. Rhead, Surface alloy formation in ultrathin layers and bimetallic double monolayers: Tin and lead on Cu(100) and Cu(111), Surf. Sci. **135** (1983) 18 – 34.

[68] T. Aruga, Surface Peierls transition on Cu(001) covered with heavier p-block metals, Surf. Sci. Rep. **61** (2006) 283 – 302.

[69] M. Batzill, D. Beck, B. E. Koel, Metastable surface structures of the bimetallic Sn/Pt(100) system, Surf. Sci. **558** (2004) 35 – 48.

[70] C. T. Campbell, Bi-metallic surface chemistry, Annu. Rev. Phys. Chem. **41** (1990) 775 – 837.

[71] Y. Gauthier, W. Moritz, W. Hoesler, Surface alloy in the $c(4\times4)$ phase of Pb on Cu(100), Surf. Sci. **345** (1996) 53 – 63.

[72] W. Hoesler, W. Moritz, LEED studies of lead on copper (100), Surf. Sci. **117** (1982) 196 – 203.

[73] W. Hoesler, W. Moritz, LEED analysis of a dense lead monolayer on copper (100), Surf. Sci. **175** (1986) 63 – 77.

[74] T. Nakagawa, S. Mitsushima, H. Okuyama, M. Nishijima, T. Aruga, Evolution of geometric and electronic structure in ultrathin In films on Cu(001), Phys. Rev. B **66** (2002) 085402.

[75] G. A. Somorjai, Modern surface science and surface technologies: An introduction, Chem. Rev. **96** (1996) 1223.

[76] J. C. Slater, Atomic radii in crystals, J. Chem. Phys. **41** (1964) 3199.

[77] C. Argile, G. E. Rhead, Growth of metal monolayers and ultrathin films on copper: Simple and bimetallic layers of lead and tin, Thin Solid Films **87** (1982) 265 – 275.

[78] E. McLoughlin, A. A. Cafolla, E. AlShamaileh, C. J. Barnes, A re-interpretation of the Cu(100)/Sn surface phase diagram, Surf. Sci. **482 - 485** (2001) 1431 – 1439.

[79] K. Pussi, E. AlShamaileh, E. McLoughlin, A. A. Cafolla, M. Lindroos, Determination of the structure of Cu(100)-$p(3\sqrt{2} \times \sqrt{2})R45°$-Sn by dynamical LEED, Surf. Sci. **549** (2004) 24 – 30.

[80] J. Martínez-Blanco, V. Joco, P. Segovia, T. Balasubramanian, E. G. Michel, Surface phase diagram and temperature induced phase transitions of Sn/Cu(100), Appl. Surf. Sci. **252** (2006) 5331 – 5334.

[81] J. Lallo, L. V. Goncharova, B. J. Hinch, S. Rangan, R. A. Bartynski, D. R. Strongin, Structural studies of sub monolayer Sn/Cu(001) structures, Surf. Sci. **602** (2008) 2348 – 2357.

[82] Y. Nara, K. Yaji, T. Iimori, K. Nakatsuji, F. Komori, STM observation of surface phases of Sn/Cu(001), Surf. Sci. **601** (2007) 5170 – 5172.

[83] K. Yaji, R. Nakayama, K. Nakatsuki, T. Iimori, F. Komori, Ordered structures of tin-adsorbed Cu(001) surfaces with over $\frac{1}{2}$ monolayer coverage, Surf. Sci. **603** (2009) 341 – 348.

[84] Y. Ku, S. H. Overbury, Surface structure analysis of Sn on Ni(111) by low energy alkali ion scattering, Surf. Sci. **273** (1992) 341 – 352.

[85] R. G. Musket, W. McLean, C. A. Colmenares, D. M. Makowiecki, W. J. Siekhaus, Preparation of atomically clean surfaces of selected elements: A review, Appl. Surf. Sci. **10** (1982) 143 – 207.

[86] F. Bocquet, S. Gauthier, A study of the low-temperature submonolayer deposition of Pb on Cu(100), Surf. Sci. **416** (1998) 1 – 8.

[87] M. Kildemo, T. Ramsvik, S. Raaen, Investigation of the La-Rh(100) surface alloy, Surf. Sci. **490** (2001) 1 – 12.

[88] H. L. Meyerheim, M. D. Santis, W. Moritz, I. K. Robinson, Domain-wall interactions in Bi/Cu(001), Surf. Sci. **418** (1998) 295 – 302.

[89] A. A. Cafolla, E. McLoughlin, E. AlShamaileh, P. Guaino, G. Sheerin, D. Carty, T. McEnvoy, C. J. Barnes, V. Dhanak, A. Santoni, Observation of an anti-phase domain structure in the Cu(100)/Sn surface alloy system, Surf. Sci. **544** (2003) 121 – 133.

[90] M. Draxler, M. Walker, C. F. McConville, Determination of correction factor for the interaction potential of He^+ ions back-scattered from a Cu(100) surface, Nucl. Instrum. Meth. B **249** (2006) 812 – 815.

[91] D. P. Woodruff, J. Robinson, Some structural issues in surface alloys and alloy surfaces: Rumpling, stacking faults and disorder, Appl. Surf. Sci. **219** (2003) 1 – 10.

[92] K. Heinz, L. Hammer, Nanostructure formation on Ir(100), Progress in Surface Science **84** (2009) 2 – 17.

[93] C. J. Baddeley, L. H. Bloxham, S. C. Laroze, R. Raval, T. C. Q. Noakes, P. Bailey, Quantitative analysis of adsorbate induced segregation at bimetallic surfaces: Improving the accuracy of MEIS results, J. Phys. Chem. B **105** (2001) 2766 – 2772.

[94] J. D. Fuhr, J. E. Gayone, J. Martínez-Blanco, E. G. Michel, H. Ascolani, Structural and electronic properties of $(3\sqrt{2} \times \sqrt{2})r45°$–Sn/Cu(100): Density functional theory and scanning tunneling microscopy, PRB **80** (2009) 115410.

[95] R. Kirchner, E. Roeckl, Investigation of gaseous discharge ion sources for isotope separation on-line, Nucl. Instrum. Meth. **133** (1976) 187–204.

[96] H. Winter, A. Schüller, Rainbow scattering under axial surface channeling, Nucl. Instrum. Meth. B **232** (2005) 165 – 172.

[97] D. Primetzhofer, S. N. Markin, M. Draxler, R. Beikler, E. Taglauer, P. Bauer, Strength of the interatomic potential derived from angular scans in LEIS, Surf. Sci. **602** (2008) 2921 – 2926.

[98] H. Dürr, T. Fauster, R. Schneider, Surface structure determination of the (2×1)O—Cu(110) reconstruction by low-energy ion scattering, Surf. Sci. **244** (1991) 237.

[99] R. Spitzl, H. Niehus, G. Cosma, Structure investigation of the nitrogen induced Cu(110)-(2×3) phase with 180° low energy impact collision ion scattering spectroscopy, Surf. Sci. Lett. **250** (1991) L355.

[100] H. L. Davis, J. R. Noonan, L. H. Jenkins, Determination of a Cu(110) surface contraction by LEED I-V, Surf. Sci. **83** (1979) 559.

[101] D. L. Adams, H. B. Nielsen, J. N. Andersen, I. Stensgaard, R. Feidenhans'l, J. E. Sorensen, Oscillatory relaxation of the Cu(110) surface, Phys. Rev. B **49** (1982) 669.

[102] H. L. Davis, J. R. Noonan, Cu(100) multilayer relaxation, J. Vac. Sci. Technol. **20** (1982) 842.

[103] D. L. Adams, H. B. Nielsen, J. N. Andersen, Oscillatory relaxation of the Cu(110) surface, Surf. Sci. **128** (1983) 294.

[104] H. L. Davis, J. R. Noonan, Multilayer relaxation in metallic surfaces as demonstrated by LEED analysis, Surf. Sci. **126** (1983) 245.

[105] S. A. Lindgren, L. Walldén, J. Rundgren, P. Westrin, LEED from Cu(111): Subthreshold effect and energy-dependent inner potential; surface relaxation and metric distances between spectra, Phys. Rev. B **29** (1984) 576.

[106] D. M. Lind, F. B. Dunning, G. K. Walter, H. L. Davis, Surface-structural analysis by use of spin-polarized LEED: An investigation of the Cu(100) surface, Phys. Rev. B **35** (1987) 9037.

[107] L. K. Verheij, J. A. van den Berg, D. G. Armour, Structure analysis of an oxidized nickel (110) surface using low energy ion scattering, Surf. Sci. **84** (1979) 408.

[108] D. S. Karpuzov, I. N. Evdokimov, D. G. Armour, G. Carter, Identification of ion path in crystal surface channels, Phys. Lett. **68A** (1978) 485 – 487.